7-8-2020

The Medium-Term and Event-Scale Tropical Cyclone-Driven Morphodynamics of a Vulnerable Barrier System with Emphasis on the Role of Backbarrier Wetlands

Cody Lee Johnson I
Louisiana State University and Agricultural and Mechanical College

THE MEDIUM-TERM AND EVENT SCALE TROPICAL CYCLONE-DRIVEN MORPHODYNAMICS OF A VULNERABLE BARRIER SYSTEM WITH EMPHASIS ON THE ROLE OF BACKBARRIER WETLANDS

A Dissertation

Submitted to the Graduate Faculty of the
Louisiana State University and
Agricultural and Mechanical College
in partial fulfillment of the
requirements for the degree of
Doctor of Philosophy

in

The Department of Civil and Environmental Engineering

by
Cody Lee Johnson I
BS, Florida State University, 2010
MS, Louisiana State University, 2016
August 2020

For Gretchen Johnson, who had enough faith for us all.

ACKNOWLEDGMENTS

I want to first of all thank my parents, Christopher and Mary Johnson, who never failed to create a positive environment for me. I also need to thank Kristina Sebastian and the rest of my friends and family. Certainly, very little through me would be possible without their support and friendship.

My sincerest gratitude is given to Dr. Qin Chen and Dr. Celalettin Ozdimer for advising my Ph.D. and guiding my education at Louisiana State University. I also want to thank Dr. Kehui Xu and Dr. Scott Hagen for serving on my dissertation committee and Dr. John A. Nyman for acting as the Dean's representative. I am also indebted to the faculty and staff of Louisiana State University and the Department of Civil and Environmental Engineering, especially Dr. Clint Wilson and Dr. Navid Jafari, for their mentorship. I am also grateful for the time I have been able to spend studying and working with my student colleagues at Louisiana State University, in particular Sahar Haddadian and Ling Zhu.

A great degree of gratitude is owed to Louisiana's Coastal Protection and Restoration Authority (CPRA) for their assistance and data resources; specifically, Mark Leadon, formerly of the CPRA, and Jacques Boudreaux. Discussions with Dr. Nathaniel Plant, Dr. Davina Passeri, Alexandra Fredricks, and Kara Doran from the United States Geological Survey, and Dr. Ap van Dongeren, Robert McCall and Kees Nederhoff of Deltares were helpful throughout my dissertation.

The study was, for the most part, supported by a Louisiana Board of Regents' Doctoral Research Fellowship. This project was also funded to a less extent by The Water Institute of the Gulf (TWIG) under project award number 21.015/RCEGR260003-01-00 [project title "Integrating High-Fidelity Models with New Remote Sensing Techniques to Predict Storm Impacts on Louisiana Coastal and Deltaic Systems"]. The statements, findings, conclusions, and recommendations are those of the author and do not necessarily reflect the views of the Department of the Treasury, the Louisiana Coastal Protection and Restoration Authority (CPRA) or TWIG.

TABLE OF CONTENTS

ACKNOWLEDGMENTS iii

LIST OF TABLES vi

LIST OF FIGURES vii

ABSTRACT x

CHAPTER

1 INTRODUCTION 1
- 1.1 Motivation 1
- 1.2 Background 2
- 1.3 Problem Statement 5
- 1.4 Hypotheses and Research Questions 6
- 1.5 Objectives and Outline 7

2 LIDAR TIME-SERIES ANALYSIS OF A RAPIDLY TRANSGRESSING LOW-LYING MAINLAND BARRIER (CAMINADA HEADLANDS, LOUISIANA, USA) 10
- 2.1 Introduction 10
- 2.2 Regional Setting 12
- 2.3 Methods 18
- 2.4 Results 24
- 2.5 Discussion 36
- 2.6 Conclusions 48

3 EVENT-SCALE MORPHOLOGICAL MODELING OF LOW-LYING MAINLAND BARRIER SUBJECT TO HURRICANE FORCING:THE ROLE OF BACKBARRIER WETLANDS 51
- 3.1 Introduction 51
- 3.2 Study Area 53
- 3.3 Materials and Methods 56
- 3.4 Results 62
- 3.5 Discussion 74
- 3.6 Conclusions 81

4 CHARACTERISTICS OF TROPICAL CYCLONE FORCING TO BEACH AND DUNE RESTORATIONS IN CONJUNCTION WITH BACKBARRIER MARSH CREATION SCENARIOS 83
- 4.1 Introduction 83
- 4.2 Materials and Methods 84
- 4.3 Results 89
- 4.4 Discussion 98
- 4.5 Conclusions 102

5 CONCLUSIONS 104

APPENDIX

A SUPPLEMENTAL MATERIAL FOR CHAPTER 2 112
- A.1 Work flow 112

A.2 Lidar data pre-processing . . . 114
A.3 DTM generation . . . 116
A.4 Morphometric analysis . . . 118
A.5 Assessment of lidar accuracy . . . 120
A.6 LWR window-size sensitivity . . . 123

B PERMISSION LETTER FOR CHAPTER 2 . . . 125

REFERENCES . . . 126

VITA . . . 137

LIST OF TABLES

2.1 Details of tropical cyclones making landfall within 100 km of the CH between 1998 and 2013. 18

2.2 Reported lidar survey metadata 19

2.3 Dune overwash statistics. 25

2.4 Dune and shoreline changes due to storm impacts. 33

2.5 Dune and shoreline recovery between TC impacts. 34

3.1 Land cover class definition correspondence with C-CAP classification scheme and their associated Manning's n values for bed roughness. 61

3.2 Statistical performance metrics for the LA domain's flow and wave models. 64

3.3 Statistical assessment of the computed V_{sa} and z_{dc} and their net changes for the entire CH domain. 66

3.4 Statistics of computed bed level changes at subregions BT, BC, and the overall CH grid. 71

A.1 Statistics of lidar survey validation. 117

A.7 Optimized MCC parameter values. 121

A.8 Statistics and cross-validation results for lidar surveys. 121

LIST OF FIGURES

2.1 Map of southeastern coastal Louisiana showing the study area and tropical cyclone tracks. 13

2.2 Wave climate and water level time series for the study period. 17

2.3 Example results of morphological feature extraction. 21

2.4 Net erosion and dune translation rate between September 1998 and March 2013 24

2.5 Shoreline (x_{sl}) and dune crest position (x_{dc}) time series 26

2.6 Time series of z_{dc} and dune volume per zone. 27

2.7 Alongshore-averaged cross-shore profiles for the western section. 28

2.8 Alongshore-averaged cross-shore profiles for the central section. 28

2.9 Alongshore-averaged cross-shore profiles for the eastern section. 29

2.10 Shoreline erosion rate time stack. 30

2.11 Timestack of dune crest elevation and dune volume per unit width. 31

2.12 Spatial relationship between net erosion rate and near-field backbarrier LWRs. 34

2.13 Mean z_{dc} elevation versus LWR calculated using a 25 m window. 35

2.14 Relationship between net erosion rate and mean dune crest elevation versus LWR. 36

2.15 Comparison of LWR contours between the beginning and end of the study period. 37

2.16 Conceptual diagram of a system in metastable equilibrium subject to a significant storm impact. 39

2.17 Stages in the evolution of a low-lying, frequently overwashed barrier. 40

3.1 CH model grid and initial bed level relative to the GoM and LA grids. 55

3.2 Shoreline mapping of LULC classifications. 60

3.3 Observational stations and computed versus measured surface wave and water level comparisons 63

3.4 Boundary conditions and hydrodynamic verification for CH model. 64

3.5 Alongshore distribution of computed and observed post-storm dune volume and respective scatter plots. 65

3.6 Alongshore distribution of computed and observed post-storm dune crest elevation and respecitve scatter plots. 66

3.7 Computed versus observed net Δz for the central portion of the CH. 67

3.8 Bed level dynamics at the BT subregion. 68

3.9 Pre- and post-storm computed bed level profiles in comparison with LIDAR observations (blue circles) for the BT subregion and the BC subregion. 69

3.10 Bed level dynamics at the BC subregion. 70

3.11 Cross-shore bed level evolution at BT3. 72

3.12 Cross-shore bed level evolution at BC3. 72

3.13 Alongshore averaged pre- and post-storm cross-shore profiles. 75

3.14 Correlation between sediment displacement componenets and average backbarrier Manning's n and average elevation 76

3.15 Distributions of post-storm V_{sa} per unit width in the CH's central section. 78

3.16 Pre- and post-storm aerial imagery and cross-shore profiles at SL1 and SL2. 79

4.1 The CH model grid and initial bed level. 85

4.2 Typical design profile for the Caminada Beach and Dune Restoration. 85

4.3 Initial topo-bathymetric inputs for the BD, MC and WD restoration scenarios at sample transects T1, T2, and T3. 86

4.4 Water level and surface wave boundary conditions. 88

4.5 Pre- and post-storm profiles for the HG storm conditions. 90

4.6 Pre- and post-storm profiles for the 100 year storm conditions. 91

4.7 Alongshore averaged transport of dune volume at sample transects T1, T2, and T3. 92

4.8 Distributions of sediment displacement components at sample transects T1, T2, and T3. 92

4.9 Cross-shore bed level evolution at T1 for the BD scenario under 100 year storm conditions. 93

4.10 Cross-shore bed level evolution at T1 for the MC scenario under 100 year storm conditions. 94

4.11 Cross-shore bed level evolution at T1 for the WD scenario under 100 year storm conditions. 94

4.12 Cross-shore bed level evolution at T1 for the BC scenario under HG storm conditions. 96

4.13 Cross-shore bed level evolution at T1 for the MC scenario under HG storm conditions. 96

4.14 Net volumetric change over the 100 year storm event as a function of alongshore distance. 97

4.15 Net dune crest elevation change over the 100 year storm event as a function of alongshore distance. 98

4.16 Pre- and post-storm profiles at the sample transects T1, T2, and T3 for the 100 year storm event. 100

4.17 Alongshore distribution of dune crest lowering due to the 100 year storm event. 100

A.1 Flowchart for pre-processing and analyzing lidar data. 113
A.2 Location of GCPs in relation to Chevron Rd., Port Fourchon, LA. 116

A.3 Comparison of GCP elevations with mean lidar elevations at each GCP along Chevron Rd. 117

A.4 LWRs computed with different sliding window operator sizes. 124

ABSTRACT

Coastal mainland barriers and barrier islands provide the first line of defense against oceanic and meteorological forces. Coastal morphological change, which may degrade these barrier's defensive capabilities, occurs over a range of time scales, from geological epochs (>1000 years) to hours and seconds. Coastal morphological change at a vulnerable, but economically strategic, barrier system—the Caminada-Moreau Headlands, Louisiana—is investigated in terms of tropical cyclone impacts and their effects over a 15 year LIDAR survey time series.

Analysis of the barrier's three-dimensional morphodynamics at medium-term (decadal) time scales reveals that, while subaerial volume was approximately conserved through time, the impact of Hurricane Gustav (2008) may have exceeded a threshold for recovery due to changes in dune morphology and net elevation loss. Additionally, medium-term coastal morphodynamics were correlated with backbarrier wetland health, attesting to the tight coupling that washover processes, which transport sediment from the beach and dunes to the backbarrier, have with these environments in low-lying barriers.

A numerical modeling system is developed to simulate the event scale (days) impact of Hurricane Gustav (2008) to the Caminada Headlands. Washover of beach and dune sediment is enhanced where the backbarrier environment exhibits reduced surface roughness (vegetated land cover) and elevation (increased accommodation space). The correlation between washover sediment transport and backbarrier wetland disintegration, suggests that coastlines which are backed by deteriorated wetlands will export more sediment and, over medium-term time scales, this will appear as enhanced local shoreline erosion. Therefore, the detailed sediment transport modeling results provide a more quantitative picture explaining the relationship identified between decadal scale shoreline morphodynamics and the backbarrier wetlands.

The numerical modeling system is modified to incorporate a recent restoration of the Caminada Headlands to investigate its response to various storm conditions. Three restoration scenario models are forced with Hurricane Gustav's waves and water levels and a synthetic 100 year return period storm. The presence of a restored backbarrier marsh reduced dune lowering and subaerial volume losses compared to the scenario without a marsh creation component or with open water. Therefore, backbarrier marsh creation, which provides vegetated land cover and elevation to help buffer washover transport, may enhance the resiliency of coastal restorations within low-lying barrier systems.

CHAPTER 1
INTRODUCTION

1.1 Motivation

Louisiana's coast (LA) is both important and unique for several reasons. It has great economic importance as a hub for domestic and international energy markets (Energy Information Administration, 2020); supports trade within the United States of America (USA), handling a fifth of all waterborne commerce (U.S. Army Corps of Engineers, 2018); and produces 30% of commercial fishing landings within the continental USA (Restore the Mississippi River Delta, 2020). Among its many unique natural characteristics, arguably the most distinctive are the dynamic deltaic landscape, formed from the geologic history of the Mississippi River (MR) (Roberts, 1997; Penland et al., 1988); the extensive wetland ecosystems, which constitute approximately 40% of that in the USA (Shirley, 2020); and the frequent impacts of tropical cyclones (TC) which have shaped LA's coast morphology (Stone et al., 1997).

The relationship between coastal LA's economic importance and natural environment is fraught with tension. Economic agents, which rely on the natural environment for protection and resources, have historically caused unmitigated environmental disturbances. One of the most conspicuous consequences of this has been the quantity and rate of coastal land loss throughout the 20^{th} and 21^{st} centuries (Shirley, 2020). From 1932 to 2010, LA lost approximately 4870 km^2 of land and an additional 5430 km^2 are at risk to be lost by 2060 (Couvillion et al., 2011, 2017). In addition, portions of vulnerable shorelines, e.g., the Caminada Headlands, have migrated landward over 1.5 km during the past century and a half (Williams et al., 1992).

As a result of the land loss and shoreline migration, important societal investments and valuable infrastructure are at risk of coastal flooding and TC impacts; further, they will probably become more vulnerable in the future due to climate change and global sea-level rise (SLR) (Oppenheimer et al., 2019). Mainland barriers and barrier islands, backed by coastal wetlands, are the chief and most vanguard natural defenses against these ocean-borne hazards (Everard et al., 2010; Otvos, 2011; Hanley et al., 2014). Understanding LA's barrier systems, particularly their response to TCs, i.e., their primary morphodynamic driver over short- and medium-term (years to decades) times scales (Stone et al., 1997), is therefore a worthwhile endeavor for coastal research and the motivation for this dissertation.

1.2 Background

Spatial variability in LA's shoreline erosion rate depends on antecedent geological conditions (Penland and Boyd, 1981) and temporal trends in erosion have been related to TC activity (Stone et al., 1997, 2004; Kindinger et al., 2013; Johnson et al., 2019). One major driver of shoreline erosion and land loss in LA is a landscape scale sediment deficit, which has both natural and anthropogenic causes (Blum and Roberts, 2009; Twilley et al., 2016). The sediment deficit is geologically controlled by the Mississippi River Delta's (MRD) fluvial geomorphic evolution throughout the middle and late Holocene, i.e., the delta cycle process (Penland et al., 1988; Roberts, 1997).

The delta cycle is the landscape-scale process whereby the MR periodically avulses due to changes in hydraulic gradient along its current course. As the MR switches course, sediment delivery to its initial depocenter on the coast progressively wanes. At some juncture in the switching process, the deltaic system transforms from progradational (i.e. land building) to transgressive, where marine processes (i.e., erosion, subsidence, and submergence) begin to dominate (Roberts, 1997). The result of the initial transition, whereby a progradational delta becomes transgressive coastal margin, defines Stage one of the delta cycle, i.e., an erosional headland with flanking barrier islands (Penland et al., 1988). Stages two and three describe subsequent phases in the evolution of an abandoned delta: a detached barrier island arc and subaqueous shoal, respectively (Penland et al., 1988; Roberts, 1997).

During the Mid- to Late-Holocene geological epoch, beginning approximately 7000 years before present (ybp), the MR is thought to have created six major depositional systems (Roberts, 1997). The current position of the MR constitutes the Balize delta complex, which formed approximately 1000 ybp. The LaFourche delta complex began construction prior to the Balize, approximately 2500 ybp, and was cutoff from sediment supply approximately 800 ybp, forming Penland et al. (1988)'s prototype for Stage one of the delta cycle. The Caminada-Moreau Headlands (CH) is the central node of the LaFourche delta complex, i.e., the "headland" in Stage 1, and is flanked on either side by Grand Isle and the Timbalier Islands to the east and west, respectfully, which are associated together as a littoral compartment. The dissertation is inextricably linked with the delta cycle, as it sets the geomorphic context for its study area, i.e. the CH, informing the natural processes and restoration strategies which are studied.

As expected, littoral compartments associated with phase one of the delta cycle exhibit very dynamic coastlines and some of the highest horizontal shoreline erosion rates observed along

LA's coast (Williams et al., 1992). Between 1887 and 2012, the CH's shoreline retreated 1550 m, while downdrift Grand Isle's accreted approximately 500 m. During this time span, the shoreline erosion rate at the CH decreased from -14.8 m yr^{-1} to -6.3 m yr^{-1} for the averaging periods of 1887 to 1930 and 1956 to 1998, respectively (Byrnes et al., 2017). However, between 2004 and 2012, the CH's shoreline erosion rate spiked to -13.6 m yr^{-1} due to a period of intense TC activity, which introduces this dissertation's other major topic: TC impacts.

Up to 90% of shoreline change in LA has been attributed to tropical storms and hurricanes and, at the decadal time-scale, they are considered the primary factor affecting shoreline morphodynamics (Morton et al., 1994; Stone et al., 1997). When a TC makes landfall, the combination of the inverse barometer effect, wind-driven storm surge, and wave-induced setup result in elevated water levels which may exceed critical geomorphic features of the impacted shoreline. Sallenger (2000) differentiates TC impacts as distinct regimes, based on total water level and pre-existing barrier elevations, that are associated with characteristic morphological responses. The most severe TC impact regimes, i.e. the overwash and inundation regimes, are expected to produce the largest morphological responses. In the case of the overwash regime, sand is transported 10s to 100s of meters landward resulting in net shoreline erosion. While, in the inundation regime, massive net onshore transport occurs where sand bodies may migrate landwards up to 1 km, based on limited observations of Hurricane Andrew's (1993) impact to Isle Dernieres, LA (Sallenger, 2000).

When an TC impact generating overwash or inundation regime forcing transpires, the beach and dune sediment which is transported landward by the overwash flux or overland flows during inundation is designated washover, in that it is has "washed over" the barrier (Donnelly, 2007). The occurrence of washover is controlled by alongshore variability in foredune elevation (Sallenger, 2000), as the storm-driven total water level must exceed this elevation to transport sediment, but it is also influenced by barrier width and hydraulic connectivity (Boyd and Penland, 1981). Barrier width primary influences washover dimensions through the introduction of frictional dissipation into overland flows which connect the ocean and backbarrier water body, so that narrow barriers tend to exhibit higher overwash velocities and greater sediment transport (Boyd and Penland, 1981).

In the case of mainland barriers like the CH, i.e., a barrier lacking a characteristic backbarrier lagoon (Otvos, 2020), gradients in friction are introduced by the backbarrier land cover's surface roughness. In the backbarrier environment, this land cover is often dominated by vegetated wetlands; in the case of LA, however, backbarrier wetlands are endemically in a state of disinte-

gration into open water due to coastal land loss. The state of backbarrier wetland fragmentation or land loss, in so far as it modifies gradients in roughness, can be understood as analogous to barrier island width and is quantifiable with various methods, e.g., the areal land-to-water ratio (LWR) (Siverd et al., 2018, 2019, 019b). Vegetated land cover, such as emergent estuarine vegetation, has been observed to influence washover (Morton and Sallenger Jr., 2003; Wang and Horwitz, 2007) and is significant for accurately modeling its dynamics and dimensions (Passeri et al., 2018; van der Lugt et al., 2019). This dissertation closely examines the connection between washover and backbarrier land cover, as the two are tightly coupled in low-lying barriers, such as the CH, which experience frequent overwashing.

As opposed to large- or medium-scale dunes which may extend many meters above mean sea-level (MSL), low-lying barriers typically exhibit maximum elevations less than 2 m above MSL. These barrier are frequently overwashed, even by less energetic meteorological systems, such as cold fronts (Rosati and Stone, 2009). Frequently overwashed, low-lying barriers may follow different trajectories of post-storm recovery than large- or medium-scale barriers (Matias et al., 2009; Houser, 2013; Houser et al., 2015) and not all stages of recovery may transpire before another overwash event occurs. At the CH, the recovery period following a major TC impact has been postulated as 10 years, which includes the continued impacts of relatively minor storm events (Ritchie and Penland, 1988). This, however, assumes that the conditions for metastable equilibrium, i.e., conditions which allow the barrier to rebound to its pre-storm state, are sustained throughout the impact/recovery cycles (Woodroffe, 2007). Metastable equilibrium can be disrupted by changes to conditions in sediment supply, the frequency/severity of storm impacts, and relative sea-level rise (RSLR), i.e., the combined effect of eustatic sea-level rise and vertical land movement, which are all factors in the CH's geomorphological evolution (Woodroffe, 2007).

If these conditions are sufficiently perturbed, then the system will be pushed past a threshold for recovery, whereon it begins to transition into a new metastable equilibrium with different characteristic morphology, e.g., continous foredunes to washover plain (Woodroffe, 2007). For instance, a transition has been forecasted for the Chandeleur Islands, LA, if disintegration continues due to storm impacts and RSLR, causing the barrier island arc to become a subaqueous shoal (Moore et al., 2014). Morphodynamic observations suggest that the central CH was pushed past a threshold for recovery following the repeated TC impacts between Hurricane Isidore (2002) and Gustav (2008) (Johnson et al., 2019). To forestall such a transition at the CH, which would place Port Fourchon, a nationally strategic oil and gas hub, at greater risk, the LA Coastal Protection

and Restoration Authority (CPRA) undertook the largest beach and dune restoration in LA's history (circa 2013). The Caminada Headlands Beach and Dune Restoration Project cost $218 million USD and placed approximately 6.43×10^6 m^3 of offshore-borrowed sandy sediment along 21.3 km of the CH's shoreline.

In addition, LA's barriers would presumably be less vulnerable to storm impacts, if the Mississippi River (MR) were not heavily engineered and channelized, a leading cause of the pervasive coastal land loss (Blum and Roberts, 2009; Twilley et al., 2016). Much of the MR's sediment load, which in natural conditions would eventually be transported to coastal marshes or barrier, is inextricably lost to the deep Gulf of Mexico and sequestered by upriver dams (Blum and Roberts, 2009). It is outside this work's scope to estimate what effect this lost sediment would have if, alternatively, it was distributed in a natural fashion along vulnerable coastal margins; however, it is reasonable to assume increased sediment input would enhance post-storm recovery and mitigate backbarrier marsh land loss. Reasoning along these lines have within the past few decades prompted LA's coastal management to consider the strategy of diverting the MR's sediment load to sediment deprived coastal basis in an effort to build land and "work with Nature" (Xu et al., 2019). If incorporated into a holistic management strategy, in conjunction with ecological objectives and traditional coastal renourishments, sediment diversions could serve to replenish impacted barrier islands and rebuild their deteriorated backbarrier marshes.

In summary, the CH has experienced a large reduction in sediment input, a probable future scenario for deltaic coasts globally (Nienhuis et al., 2020); experiences high rates of RSLR and erosion due to its geological history; is prone to TC impacts; and, yet, is necessarily a high priority for restoration due to its importance as a storm-buffer for valuable infrastructure. By virtual of these aspects, the CH's situation typifies the concept that LA can serve as a "living laboratory" for global coastal research. This dissertation is an effort to work within this "living laboratory" and generate coastal research for communities which, in the global context of sea-level rise and climate change, may soon find themselves in similar circumstances, faced with similar problems and engineering projects.

1.3 Problem Statement

Understanding the TC-driven morphodynamics of coastal barrier is a multi-scale problem. On one hand, TCs drive decadal scale shoreline change within pre-existing geological and geomorphic controls in conjunction with aeolian and marine recovery processes. On the other hand, the actual morphological change occurs at the event time-scale, i.e., over a few days as the TC

makes landfall. These two time-scales are linked by many processes which influence the impacted area's geomorphology. In this dissertation, the link between TC-driven morphological change and backbarrier wetlands is examined at both time-scales. On the way, insights and details are furnished on the physics and phenomena of overwash and washover sediment transport at low-lying barrier systems.

To accomplish this, two distinct, but complementary, disciplines are utilized: remote-sensing and physics-based numerical modeling. LIDAR surveys of the CH are compiled and analyzed for morphodynamic trends during a period of intense TC activity (1998 to 2013). Key patterns in shoreline morphodynamics, dune morphology change, and post-storm recovery rates are presented and related to a conceptual model for frequently overwashed barriers. Further, medium-scale shoreline morphodynamics are correlated with a remotely sensed LWR index, as a proxy for wetland health, in the backbarrier. Consideration of this observation, and the predominate role TC impacts play in shaping shoreline morphology, leads to the use of numerical models to explore this relationship further.

A fully-coupled basin- and regional-scale hydrodynamic-wave model (Delft3D/SWAN) is used to hindcast the impact of Hurricane Gustav (2008) to the CH, the most morphdynamically relevant storm of the LIDAR analysis period. The hydrodynamic-wave model forces a high-resolution local-scale sediment transport-morphodynamic model (XBeach). Both modeling components are verified with multiple datasets (surface waves, water levels, LIDAR-based morphology) and good agreement is found. The sediment transport model allows for insight into the evolution of TC-driven morphological impacts and the physical processes of washover. The model results are tied to the backbarrier wetland in terms of elevation and vegetated land cover.

The insights drawn from this lead to numerical experimentation which investigates restoration scenarios for the CH that allow for enhanced resiliency to TC impacts. Restoration scenarios are prepared which systematically vary the backbarrier wetland to answer questions about its affect on TC impacts to a restored beach and dune. The results hopefully provide guidance on the creation of backbarrier marshes in conjunction with beach and dune restorations.

1.4 Hypotheses and Research Questions

This dissertation endeavors to test the following hypotheses:

1. *In low-lying barriers, where frequent overwashing intimately connects the nearshore and backbarrier environment, fragmentation and marsh surface land loss increase shoreline migration rates.*

2. *Surface roughness and topography, important environmental parameters for inundation regime driven overland flows, are correlated with washover sediment transport.*

3. *Beach and dune restorations are affected by backbarrier marsh creation components when impacted by overwash and inundation regimes; and this is manifested as a reduction in subaerial volumetric loss and dune crest lowering.*

In the course of testing the first hypothesis, the following research questions will be addressed: (1a) How does the three-dimensional morphology of the CH respond to multiple TC impacts at medium-term and event-scale time scales? Can the spatial patterns of TC impacts to the CH, and its recovery, be explained by pre-exiting conditions? (1b) Does TC impact recovery at a vulnerable, low-lying barrier follow a predictable sequence of stages? If so, how, and in what way, is the sequence interrupted by additional TC impacts?

To test the second hypothesis, these research questions related to the numerical modeling of storm impacts are addressed: (2a) How accurately can TC impacts to low-lying barriers be numerically modeled? In this context, is incorporation of limited nearshore sediment availability and variable surface roughness, particular to the CH, necessary? (2b) Can the sediment transport processes that relate backbarrier marshes and shoreline morphodynamics, observed at decadal time scales, be identified in event-scale processes with a physics-based numerical model? (2c) What can the physics-based numerical elucidate, in terms of the evolution of storm impact regimes to low-lying barriers and their morphological responses, which is difficult to observe in the field? Specifically, when does the majority of sediment transport occur, i.e., during the inundation regime or the overwash regime?

Finally, for testing the last hypothesis related to restoration of vulnerable beach and dune systems, these research questions are posed and investigated: (3a) Can numerical model experiments be used to evaluate restoration designs at the CH in terms of their performance under different storms conditions? Specifically, can the CH's recent beach and dune restoration withstand a Hurricane Gustav-like impact or a 100 year storm? Further, can the hypothetical addition of a backbarrier marsh creation increase the resiliency of the CH's beach and dune restoration to future TC impacts?

1.5 Objectives and Outline

To answer the questions stated above, the following objectives are set forth:

1. Compile, perform quality-assurance, and analyze the three-dimensional morphodynamics

of all LIDAR surveys which exist for the CH (1998 - 2013);

2. Correlate the CH's morphodynamics to a remotely-sensed environmental index (LWR) of its backbarrier wetlands and identify trends;

3. Compare and contrast the CH's morphodynamics to a conceptual model for the evolution of frequently overwashed barriers;

4. Couple a large-scale hydrodynamic-wave and local-scale sediment transport-morphodynamic model and verify the modeling system with multiple hydrodynamic and morphological datasets;

5. Apply the modeling system to hindcast the impact of Hurricane Gustav (2008) to the CH and analyze the sediment transport and morphodynamic processes of the impact in relation to the CH's unique characteristics;

6. Incorporate data from the recent restoration of the CH into the modeling system and conduct numerical experiments for varying storm conditions and restoration scenarios;

Chapter 2 contains the presentation and analysis of a 15 year time series of LIDAR surveys of the CH. This work was previously published in the Journal of Geomorphology (Johnson et al., 2019). The LIDAR time series is related to a database of named TC which made landfall with 100 km of the CH. Three-dimension morphodynamic analysis of the LIDAR is accomplished by extracting the shoreline position and the dune position and elevation through time. Temporal and spatial trends in the morphodynamics are presented and related to the CH's backbarrier wetland.

In Chapter 3, a fully-coupled basin- and regional-scale hydrodynamic-wave model is one-way coupled with a local-scale sediment transport-morphodynamic model to hindcast Hurricane Gustav's (2008) impact to the CH. The hindcast is verified with observations of surface wave parameters; coastal and wetland water levels; and LIDAR derived subaerial barrier morphology and morphodynamics. A numerical experiment which limits the nearshore bed sediment supply during the TC impact is used to investigate causes of systematic bias in the local-scale sediment transport-morphodynamic model.

In Chapter 4, the verified local-scale sediment transport-morphodynamic model is employed to forecast TC impacts to the CH after the restoration of its beach and dunes. Hurricane Gustav-like forcing, and synthetic 100 year return period storm conditions, are used to drive the model.

Three restoration scenarios are modeled to investigate the effect of simultaneously incorporating a backbarrier marsh creation component into the CH's beach and dune restoration.

Finally, a summary of the dissertation and its main conclusions are provided in Chapter 5.

CHAPTER 2
LIDAR TIME-SERIES ANALYSIS OF A RAPIDLY TRANSGRESSING LOW-LYING MAINLAND BARRIER (CAMINADA HEADLANDS, LOUISIANA, USA)

2.1 Introduction

Coastal barrier islands and mainland barriers, referred to here as barriers or barrier systems, serve as the first line of defense against oceanic waves and storm surge generated flooding (Everard et al., 2010; Otvos, 2011; Hanley et al., 2014). These systems are composed of different physical and ecological components, e.g. the shoreface, backshore, dunes, tidal inlets, and are often backed by wetlands and estuaries. The subaerial backshore and dunes constitute components of "structural and morphological resistance" that contribute to the resiliency of the barrier island (Woodroffe, 2007). Without an intact backshore and dunes, oceanic forcing would cause significantly more damage to the system itself, its associated backbarrier ecosystems, and any landward infrastructure (Hinkel et al., 2013). There is growing evidence that the physical integrity and functionality of barrier systems may degrade in the future due to increased erosion associated with relative sea-level rise, a changing storm climatology, and increased anthropogenic disturbance (Stive, 2004; Gutierrez et al., 2007; Hanley et al., 2014; IPCC, 2014; Luijendijk et al., 2018).

Recognition of barrier systems' protective function and considerations of their unpredictable future have prompted decision-making authorities to adopt systematic beach and dune restoration programs at a regional scale (Kulp et al., 2005; Lopez, 2009; Hinkel et al., 2013; Toimil et al., 2017; Psuty et al., 2018). Determining the priority of projects is important due to limited project funding and viable sediment resources and decision-making often relies on trends in shoreline erosion. Vulnerability, defined as "the degree to which a coast is likely to be affected by or its incapability to withstand the consequences of impact" (Woodroffe, 2007), is another important criterion. Barrier storm impact response, however, is strongly influenced by the storm's maximum water level relative to the dune crest elevation and the breadth of its backshore and dunes (Leatherman, 1987; Thieler and Young, 1991; Sallenger, 2000; Morton, 2002; Wang and Horwitz, 2007; Houser et al., 2008; Stockdon et al., 2009; Houser and Mathew, 2011). Most shoreline erosion analyses neglect the coastline's vertical dimension and thus do

This chapter was previously published as Cody L.Johnson et al., "Lidar Time-series Analysis of a Rapidly Transgressing Low-lying Mainland Barrier (Caminada Headlands, Louisiana, USA)," *Geomorphology* 352 (2019). Reprinted by permission of Elsevier.

not fully capture its capability to withstand storm impacts. Therefore, more comprehensive three dimensional analyses are required which consider trends in dune morphology and sediment volume (Cooper et al., 2018).

Studies have employed lidar and GIS techniques to analyze storm-driven morphodynamics and volumetric change for several decades (Andrews et al., 2002; Woolard and Colby, 2002; Rader et al., 2018). Lidar is a remote sensing technique that provides extensive and accurate three dimensional geospatial data and has many advantages for the measurement of storm impacts (Krabill et al., 2000; Sallenger et al., 2003). Airborne lidar surveying is capable of rapid and wide ranging data collection, making it well suited to survey large swaths of coastline immediately following a storm. Coastal dune response to hurricane impacts within the Gulf of Mexico (GoM) has been successfully assessed with lidar (Houser et al., 2008; Priestas and Fagherazzi, 2010; Houser and Mathew, 2011). Lidar survey time-series have also been assembled to study multi-year or decadal time-scale coastal morphodynamics (Lentz and Hapke, 2011; Hapke et al., 2013; Houser et al., 2015). Lidar data nevertheless must be utilized in some coastal morphodynamic studies with caution. Acquisition noise, systematic biases, unclassified vegetation, and natural randomness can potentially exceed the morphodynamic signals of interest (Mitasova et al., 2009). In these cases, independent ground-truthing is a necessary step for the production of reliable morphometric analysis (see online supplement for further information).

This study assesses changes in the vulnerability of the Caminada-Moreau Headlands (CH), LA by analyzing the morphodynamics of its shoreline, backshore, and dunes through a sequence of hurricane and tropical storm impacts from 1998 to 2013 with the objective of providing a globally-applicable analogy for a rapidly transgressing mainland barrier. A detailed examination of this period reveals the evolution of a low-lying barrier due to frequent storm impacts with insufficient recovery time and constrained by spatially variable geomorphic controls (i.e. coastal infrastructure, backbarrier ecological health, and sediment supply). Nine airborne lidar surveys are utilized for the analysis. The results can inform conceptual models and, in this work, are situated in the framework of Matias et al. (2009)'s model for frequently overwashed barriers. The increased detail and resolution of the lidar-based methods provide a novel contribution to the long-standing history of research into the unique geology and geomorphology of LA's low-elevation dune systems. In the global context, the research provides a valuable insight into mesoscale (10^1 yr and km) barrier responses to climate change-induced increases in storm-impact frequency and exacerbated by accelerated sea-level rise. The three dimensional evolution of the barrier's geomorphology elucidates important vulnerability metrics for management such as:

subaerial sand storage, dune crest elevation, and their temporal trends. The study's impact will directly benefit coastal management in southeast Louisiana as predicting and mitigating morphological impacts and associated hazards is facilitated by the examination of historical barrier system storm response trends (Morton, 2010).

In this section, a brief introduction with relevant literature is presented. The rest of the paper is structured as follows: Section 2.2 provides an overview of the CH where its geomorphic context, hydrodynamic setting and storm climatology, and recent anthropogenic disturbances are given; Section 2.3 describes the methods of digital terrain model (DTM) creation and analysis, and the generation of land-to-water ratio (LWR) maps for the backbarrier wetland surface; in Section 2.4, results from the DTM analysis are presented; Section 2.5 discusses the CH's morphodynamics and vulnerability, and the relationship between backbarrier wetlands and shoreline erosion; Section 2.6 summarizes the key findings.

2.2 Regional Setting

2.2.1 Study Area

The Caminada-Moreau Headlands are located in the north Gulf of Mexico on the southeast coast of Louisiana (USA) approximately 100 km south of New Orleans and 100 km west of the Mississippi River bird's foot delta (see Figure 2.1). They are an attached mainland barrier, or beach ridge plain (Otvos, 2012), approximately 21 kilometers long, flanked by a series of barrier islands to the east and west. The CH are bounded by two navigational inlets: Belle Pass to the west and Caminada Pass to the east. The flanking barrier islands and the CH are often associated together as a littoral compartment called the (Late) Lafourche Delta. The entire barrier chain is situated seaward of two large, shallow coastal bays: Terrebonne and Barataria Bay to the west and east, respectively. Median grain sizes at the CH grade finer from a range of 160 to 249 (mean = 200 $\pm$ 19) μm over the dunes and beach to 74–159 (mean = 100 $\pm$ 23) μm between 5.5 and 8 m depth (Kindinger et al., 2013). The backbarrier marsh has a fragmented surface and is dominated by *Spartina alterniflora*, *Distichlis spicata*, and *Avicennia germinans*.

2.2.2 Geomorphic Context

The CH's recent geological history is characterized by stage one in the evolution of an abandoned delta complex within the Mississippi River's transgressive depositional model (Penland et al., 1988). This model describes coastal geomorphic evolution forced by the periodic migration of the Mississippi River's main channel, which reconfigures landscape-scale sediment distribution

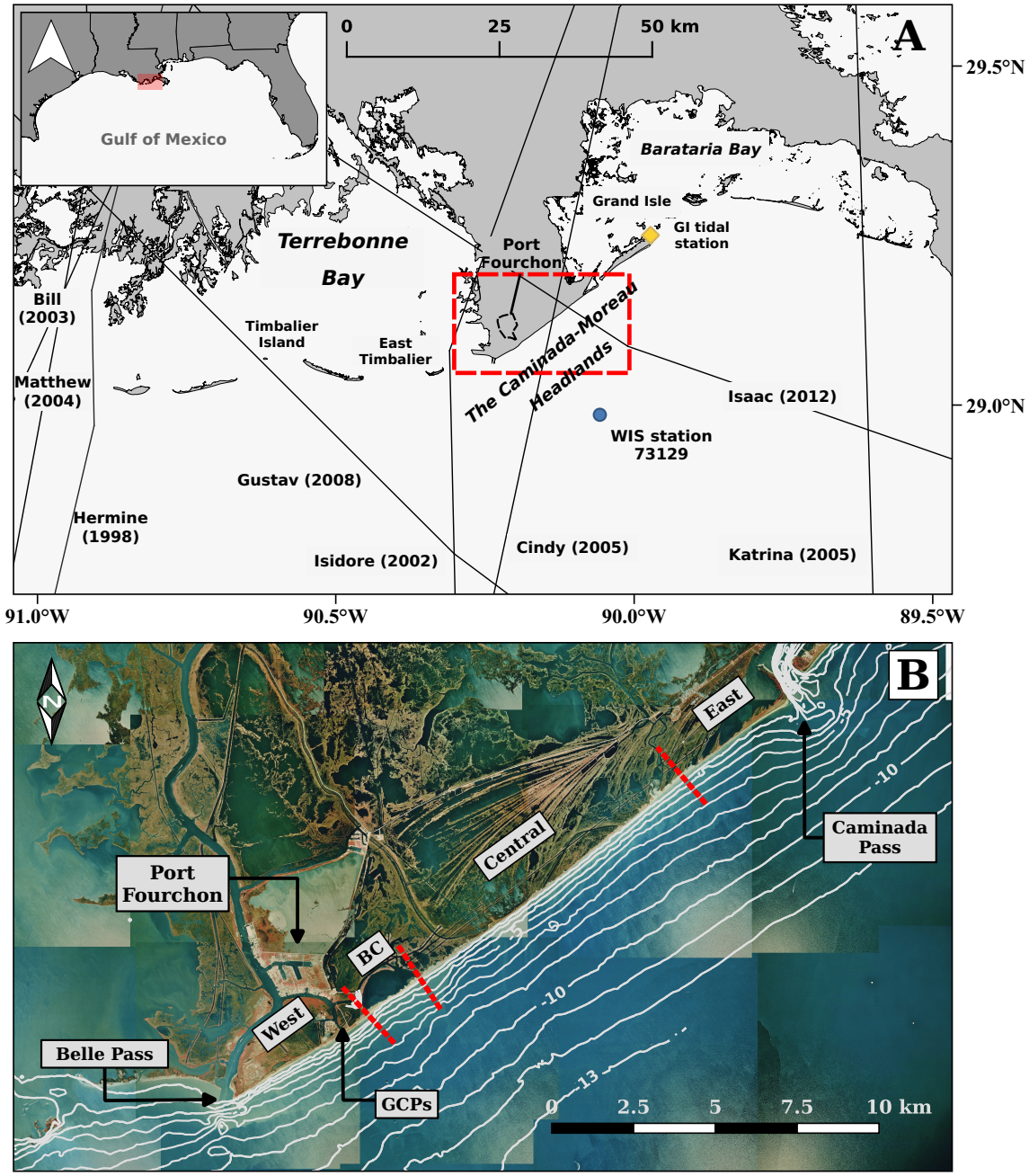

Figure 2.1: (A) Map of southeastern coastal Louisiana showing the study area outlined by a red broken line (B). Tropical cyclones making landfall within 100 km of the CH from 1998 to 2013 are indicated with black tracks. The Grand Isle tidal station and the Wave Information Studies stations are shown with yellow diamond and blue circle, respectively. (B) Natural color aerial orthophoto imagery of the CH acquired on January 24th, 1998. Single-beam bathymetric data from the 2006 Louisiana Barrier Island Comprehensive Monitoring Program (Kindinger et al., 2013) is superimposed on the image as white contours (NAVD88 GEOID12B). Bay Champagne and the west, central, and east zones are separated by broken red cross-shore transects.

and abandons the previously prograding delta complex (Penland et al., 1988; Roberts, 1997). The shift in the river's depocenter and waning sediment delivery results in marine transgression of the abandoned region. The delta complex subsides and is reworked by coastal processes along its seaward margins forming a sandy coastline backed by bays and lagoons (Penland et al., 1988). Stages two and three describe the next phases of the erosional headland: a detached barrier island arc and a submerged inner-shelf shoal, respectively.

The dominance of transgressive marine processes within the study area is highlighted by its long-term coastal morphodynamics. The CH's shoreline retreated on alongshore-average 1,550 m between 1887 and 2012 (Williams et al., 1992; Byrnes et al., 2017). During this time span, the average erosion rate decreased from -14.81 m yr^{-1} to -9.86 m yr^{-1}, for the averaging periods of 1887 to 1930 and 1956 to 1998, respectively (Byrnes et al., 2017). This trend is in accord with that of the Lafourche Delta as a whole, which decreased in erosion rate from -10.42 m yr^{-1} to -6.25 m yr^{-1} from the 1880s to 2012 (Byrnes et al., 2017). Regionally, this partly reflects the advent of coastal projection and an increase in beach renourishments during the 20^{th} century.

At the CH, decelerating erosion is further related to shoreline straightening as the headland evolves toward a detached barrier island (Penland et al., 1988). From 1887 to 1988, sections of the CH directly east of Belle Pass translated landwards nearly 3 km, while shoreline near Caminada Pass accreted 500 m (Williams et al., 1992). Penland and Boyd (1981) find a similar pattern of shoreline accretion near Belle Pass and Caminada Pass, with higher erosion in the central CH, for the period from 1934 to 1974. Cross-shore profile analysis from 1973 to 1975 concluded eastward directed sediment transport due to decreasing erosion toward Caminada Pass, but also found less erosion near Belle Pass compared to the central CH (Harper, 1977). These findings, along with geomorphic evidence in the existence of the flanking barrier islands and progradational spits, suggest that a sediment transport divergence node is located centrally within the CH (Penland and Boyd, 1981; Georgiou et al., 2005; Morang et al., 2013).

Characteristic to the Lafourche Delta, decelerating erosion at the CH deviated during the 2004 to 2012 epoch, a period of intense tropical cyclone (TC) activity, when the average erosion rate spiked to -13.62 m yr^{-1} (Williams et al., 1992). Up to 90% of shoreline change in LA has been attributed to hurricanes and at mesoscale (decades) storms are considered the most significant factor affecting shoreline dynamics (Morton et al., 1994; Stone et al., 1997). Further details on the importance of hurricane driven morphodynamics, particularly washover deposition and breaching as processes in LA's coastal evolution, can be found in Ritchie and Penland (1988); Stone et al. (1997); Stone and Orford (2004); Georgiou et al. (2005); Wang and Horwitz (2007); Fearnley et al.

(2009); Rosati and Stone (2009); Sherwood et al. (2014). The CH's coastal geomorphic context has therefore been summarized as a low-energy environment (see Section 2.2.3) predominately formed by the availability of sediment, which is geologically controlled by the Mississippi River's periodic migration, and punctuated by high-energy TC events (Penland et al., 1989).

The Mississippi River delta, as well as the CH, is a highly engineered system. Upstream damming and channelization of the Mississippi River during the 19th and 20th centuries considerably decreased net sediment delivery to the coast. A presentation of this situation and a continental-scale sediment budget can be found in Blum and Roberts (2009). It is probable that the reduction in sediment availability accelerated the natural, geologically controlled erosion of the Lafourche Delta. Local to the CH, coastal protection efforts began in 1985 with the impact of Hurricane Juan. After Hurricane Andrew (1993), 13 stone-filled barges were sunk in front of Moreau Ridge in 2–3 m of water and a sea-wall was constructed (situated approximately seaward of Port Fourchon in Figure 2.1). In 2013, a 1,675 m long and 2 m in diameter geotube filled with 191,000 m^3 of in-situ sediment was placed landward of the breakwater field. The current dredging schedule for Belle Pass and Bayou Lafourche estimates that approximately 500,000 m^3 of silt and clay sediment will be deposited west of Belle Pass every 1.5–2 years. In 2015 and 2016, construction of the Caminada Headland Beach and Dune Restoration was completed. This restoration project began after the study period and is not captured in the lidar surveys.

2.2.3 Storm Climatology and Hydrodynamics

The CH are classified as a wave-dominated system with low-wave energy and exhibits a micro-tidal regime. The tides are diurnal with a range of 0.318 m and a mean higher-high water elevation of 0.332 m NAVD88 (GEOID12B) for the 2012–2016 epoch. Water level observations referenced herein are taken from the National Oceanic and Atmospheric Administration's (NOAA) long-term tide gauge located at Grand Isle (GI) station (id: 8761724), approximately 12 km east of Caminada Pass. All further reference to the North American Vertical Datum of 1988 (NAVD88) assumes geoid model 12B (GEOID12B). Regional subsidence and eustatic sea-level combine to yield a 9.09 ± 0.43 mm yr^{-1} rate of relative sea-level rise (RSLR). Zero-moment wave height and corresponding peak wave period varies between 0.88 m (5.09 s) and 0.51 m (4.92 s) for the winter and summer months, respectively (see Figure 2.2 for the deepwater wave climate and water level history over the study period). Wave data are hindcasts from 1998 and 2013 derived from the Wave Information Studies (WIS) station 73129 with a nominal depth of 21 m.

The low-energy conditions are regularly interrupted by winter cold fronts (approximately 20–

40 times per year) from September to May and occasionally by tropical storms and hurricanes from June to November (Rosati and Stone, 2009). Summer wind direction and wave propagation is typically out of the south to southeast. During the winter, meteorological forcing is controlled by cold fronts which induce a pattern of wind field rotation. The pre-frontal winds are from the south and the post-frontal winds are directed from the north (Stone et al., 2004). Cold fronts may produce relatively high deep-water significant wave heights of 3 to 4 m (Rosati and Stone, 2009). If sufficient fetch exists, post-frontal wind waves in coastal embayments may erode backbarrier marshes. The CH are mostly sheltered from post-frontal wave attack. However, these winds have a significant overland fetch and are important for aeolian transport and post-storm dune recovery (Ritchie and Penland, 1988; Harter et al., 2015).

Deviations from mean tidal level occur with cold fronts as steady pre-frontal winds may drive wind-induced setups of 0.3 m–0.4 m (Morang et al., 2013). These events are significant for coastal erosion as overtopping and overwash occur when the high-water elevation (R_{high}) exceeds or meets the dune crest elevation (D_{high} in Ritchie and Penland, 1988 and Sallenger, 2000). The top panel of Figure 2.2 shows R_{high} for the study period, where R_{high} is the sum of the observed water level and the 2% exceedence runup height. The 2% exceedence runup height is estimated following Stockdon et al. (2006).

The most significant wave and water level events at the CH are associated with tropical storms and hurricanes. In southeast LA, hurricanes have a 7 to 10 year return period with major (category 3–5) hurricanes recurring every 26 years (Keim et al., 2007). Weaker hurricanes (category 1 and 2) and tropical storms typically elevate water levels by 0.6 to 1.0 m. Major hurricanes (category 3+) generate storm surges between 1 m and 4 m, but may increase water levels up to 8 m as observed during Hurricane Katrina (2005) (Rosati and Stone, 2009).

Tropical cyclone activity was significant throughout the 19^{th} and 20^{th} centuries with 52 named storms making landfall within 100 km of the CH between 1855 and 1997. The study period (1998 to 2013) however exhibited an increase in TC landfall rate and intensity with 8 named storms in the same proximity (Williams et al., 1992; Byrnes et al., 2017). Details of these TCs are listed in Table 2.1. Distance from the CH is defined as positive if landfall is to the west as the TC's counter-clockwise rotation makes impacts in the northeast quadrant more severe (Sallenger et al., 2006). World Meteorological Organization best track data for study period's TCs can be found in Figure 2.1 (Levinson et al., 2010).

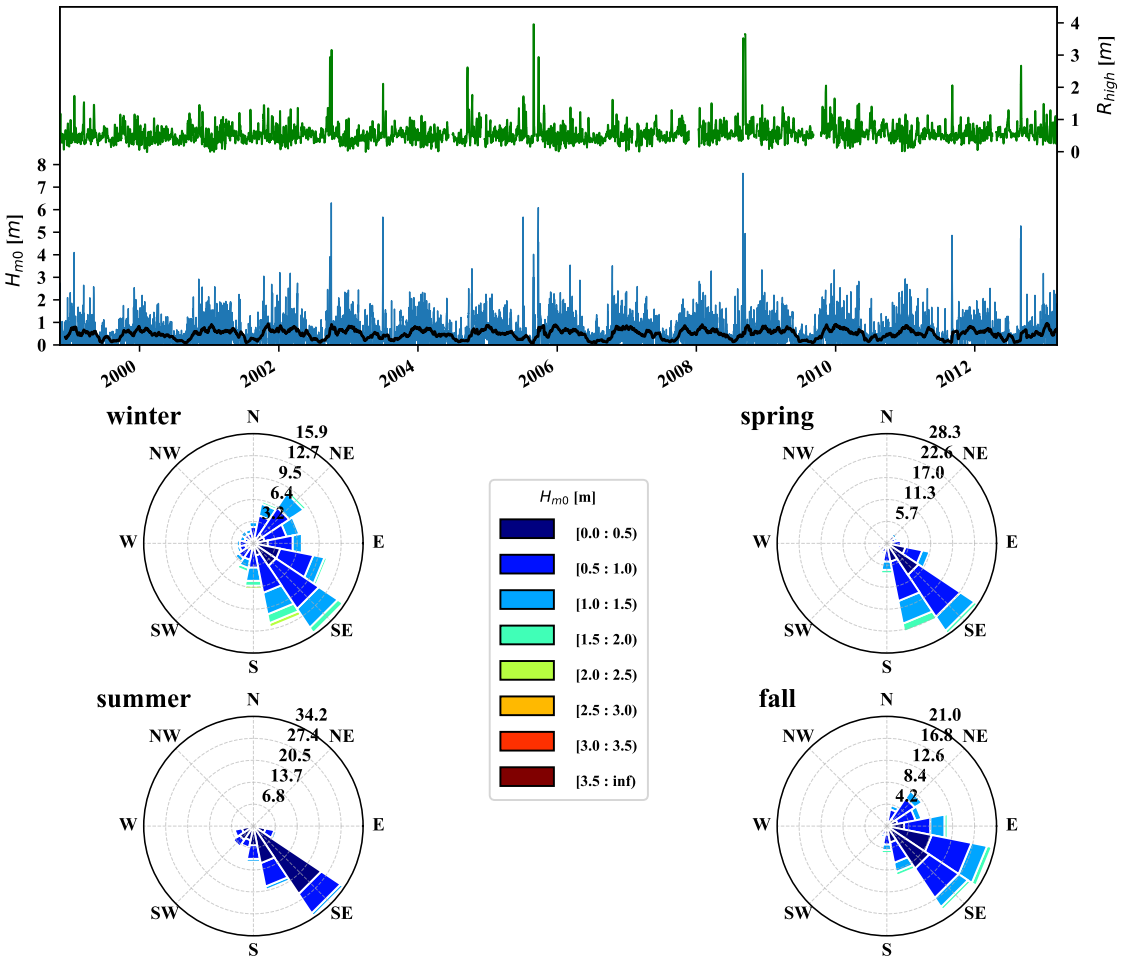

Figure 2.2: Wave climate and water level time series for the study period. (A) Hourly offshore zero-moment wave heights shown in blue with a monthly rolling average shown in black. R_{high} is shown in green. (B) Wave roses averaged by season for the time period between 1998 and 2013 pictured above.

Table 2.1: Details of tropical cyclones making landfall within 100 km of the CH between 1998 and 2013. TS = tropical storm and 1–4 are Saffir-Simpson hurricane wind scales. Water levels are the maximum observations from the Grand Isle NOAA tidal station. The wave height and peak period are maximum hindcast values from WIS station 73129.

name	landfall	category	distance from CH km	water level m, navd88	offshore H_{m0} (T_p) m (s)	wind speed km s^{-1}	central pressure mb
Hermine	1998–9–19	TS	86	0.59	2.81 (7.37)	74	1000
Isidore	2002–9–26	TS	20	1.26	4.84 (12.96)	103	989
Bill	2003–6–30	TS	97	0.83	5.71 (10.07)	93	1002
Matthew	2004–10–10	TS	94	0.97	3.43 (8.21)	74	999
Cindy	2005–7–6	1	0	0.78	5.78 (10.39)	120	992
Katrina	2005–8–29	4	-60	1.64	7.90 (16.77)	232	913
Gustav	2008–9–1	2	52	1.53	7.64 (14.71)	176	955
Isaac	2012–8–29	1	-5	1.64	5.3 (8.46)	130	966

2.3 Methods

2.3.1 Lidar Data

The complete set of existent lidar surveys which cover the CH was compiled (see Table 2.2). The first survey was flown October 9^{th}, 1998 and the final on March 8^{th}, 2013. Three surveys were collected post-storm: TS Isidore (2002); Hurricane Gustav (2008); and Hurricane Isaac (2012). The lidar are referred to by their acquisition year (2008a and 2008b differentiate between the first and second survey in 2008, respectively). Extensive pre-processing of the raw lidar data and quality-assurance checks (see Figure A.1 in the appendix for a flowchart) were performed to minimize biases in the extracted morphological parameters. An overview of the methodology is provided in this section and the reader is referred to the online supplement for further details.

The lidar data were transformed to a common geodetic system (GRS80), horizontal datum (NAD83), vertical datum (NAVD88), geoid model (GEOID12B) and projected coordinate system (UTM 15N) and imported into GRASS GIS for further processing (GRASS Development Team, 2018). The data were independently ground-truthed and shifted per survey to account for systematic biases (see Figure A.3 for an illustration of the correction's results). Forty-two observations from a 2010 terrestrial survey, which occupied the center line of a paved road

Table 2.2: Reported lidar survey metadata including the acquisition (vintage) date, collection agency, lidar system, nominal point spacing, and reported accuracy.

Date	Agency[1]	lidar equipment[2]	nominal point spacing (NPS) pt m^{-1}	accuracy vertical/horizontal m
1998–11–9	NOAA/NASA/USGS	ATM II	1/3	0.15/0.8
2001–9–10	USGS/NASA	ATM II	1/3	0.15/1.0
2002–10–12	NOAA/NASA/USGS	ATM II	1/3	0.15/0.8
2006–12–6	USGS/JALBTCX	EAARL	1/1	0.15/1.0
2008–3–9	USGS/NASA	EAARL	1/1	0.15/1.0
2008–9–6	USGS/NASA	EAARL	1/1	0.15/1.0
2010–4–26	JALBTCX	Optech ALTM Gemini System	1/1	0.15/0.5
2012–10–1	USGS	Leica ALS70	1/1	0.107/0.18
2013–3–8	USGS	Leica ALS60	1/2	0.122/0.73

(Chevron Rd. Port Fourchon, LA) as denoted by the survey team, were used as ground control points (GCPs). The median difference between a survey's lidar data and the GCPs determined the shift for that lidar survey (median errors ranged between -27.8 cm and +47.0 cm, see Table A.1 in the supplement). The 2006, 2008a, 2010, 2012, and 2013 surveys were available as classified lidar (i.e. identified as ground, water, low vegetation, etc.) following the LAS open data format specification (The American Society for Photogrammetry & Remote Sensing, 2013). Multi-curvature classification, a ground surface identification algorithm implemented in GRASS GIS (Blumentrath, 2015), was used to identify the unclassified lidar ground points (Evans and Hudak, 2007; Tinkham et al., 2011). Only lidar data classified as ground points were used in the analyses.

2.3.2 Digital Terrain Models

The lidar point clouds were gridded to 0.5 × 0.5 m^2 cells using a regularized spline with tension and smoothing (Mitasova et al., 2005). The spline parameters were selected to minimize the root-mean-square-error (RMSE) of a cross-validation sensitivity analysis (Neteler and Mitasova, 2008). Turbid waters in the CH's surfzone and marshes render lidar ground classification in these locations unreliable. DTM cells which were below mean high water (MHW) and those not contiguous with the main barrier landform were masked out to remove spurious data. The supratidal beach, backshore, and foredune were extracted for morphometric analysis.

The DTMs were analyzed for five morphological parameters: shoreline position (x_{sl}), dune crest position and elevation (x_{dc} and z_{dc}, respectively) and dune toe position and elevation (x_{dt} and z_{dt}, respectively). The parameters were extracted from cross-shore transects spaced every 10 m in the alongshore direction. The horizontal parameters were measured relative to a

baseline that was generated by smoothing and simplifying the 1998 MHW contour. The vertical features (z_{dc} and z_{dt}) are referenced to NAVD88. The shoreline position was defined as the MHW elevation for the lidar's date (Hapke et al., 2011). The dune crest was identified as the cross-shore profile's maximum elevation. The dune toe, referred to as *dune low* in storm impact studies (Sallenger, 2000), was defined as the point of maximum slope change seaward of the dune crest. Figure 2.3 illustrates a subsection of the 1998 and 2013 DTMs with example feature extraction results and a cross-shore transect. If a dune was not present, then dune low was not defined. The reader is also referred to Figure 3 in Stockdon et al. (2007) for a diagram portraying the cross-shore profile and extracted features.

Dune volume (V_d) was defined as sediment above a common threshold. The mean dune tow elevation ($\overline{z_{dt}}$) across the entire lidar survey collection was chosen to minimize the effects of seasonality and storm impacts on the individual surveys (see Section A.4 for the procedure of reducing bias introduced by RSLR). Dune volume was calculated by integrating the DTM over cells with an elevation greater than $\overline{z_{dt}}$ with,

$$V_d = \int_A z \, dA \quad \text{where} \;\; z \geq \overline{z_{dt}} \tag{2.1}$$

where V_d is dune volume, z is the DTM elevation, and A is the DTM cell area. Dune volume per unit width was calculated by dividing V_d by the alongshore length.

Change in morphological parameters and dune volume were calculated by taking the difference between lidar surveys, expressed as $\Delta\chi = \chi_{t_2} - \chi_{t_1}$, where χ represents a morphological parameter. Rates of change were computed with two methods: (1) the slope of a least-squares linear regression of the parameter's complete time series; (2) the net change (i.e. t_2 =2013 and t_1 =1998) divided by the total time elapsed.

2.3.3 Errors

Quality assurance of lidar data is critical in the low-elevation dune systems of coastal LA given the magnitude of its vertical features. Based on the independent ground-truthing, the 1998, 2001, 2002, 2010, and 2013 surveys' RMSE is smaller than the reported vertical accuracy (see Tables 2.2 and A.1). The 2006, 2008a, 2008b, and 2012 lidar surveys exhibit RMSEs outside their reported vertical accuracies, but do not have an observable trend suggesting an uncorrected bias due to subsidence. Further, the ground-truthing of these surveys yielded relatively narrow absolute error distributions (see standard deviation in Table A.1). This suggests that the relatively larger RMSE values of the 2006, 2008a, 2008b, and 2012 lidar are due to systematic errors

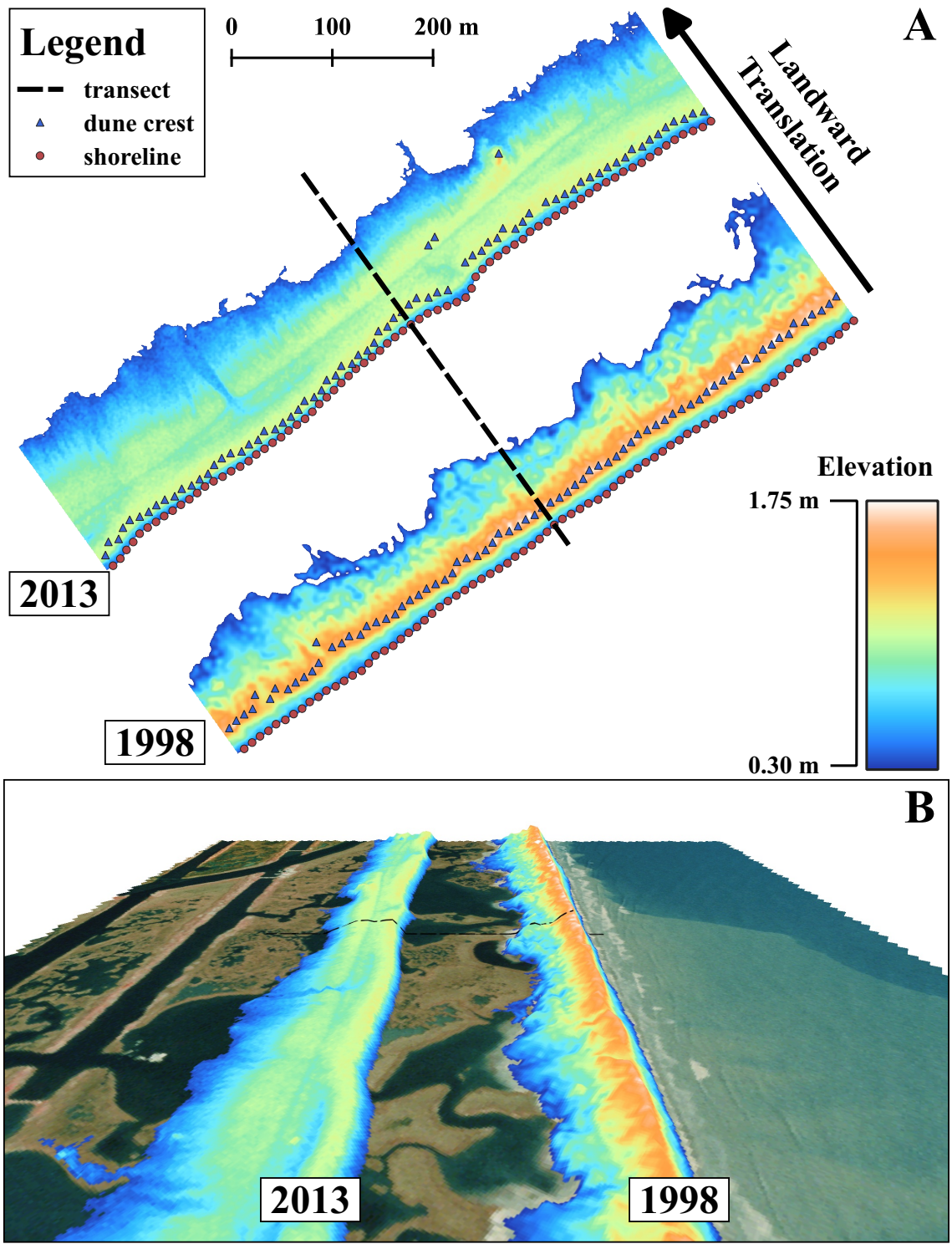

Figure 2.3: (A) The 1998 and 2013 DTMs shown in their actual position. The broken black line is an example transect. The triangles and circles indicate x_{dc} and x_{sl}, respectively. (B) 3D models of the DTMs superimposed on the 1998 aerial photography (25x vertical exaggeration). Viewpoint is looking northeast.

in the initial lidar acquisition. After correcting the lidar data with a uniform shift, the accuracy of the corrected data (computed as 1.96·RMSE) is brought within the reported accuracy for all the surveys except 2008a. The reader is referred to Section A.5 for an quality-assurance assessment of the lidar processing methods.

2.3.4 Land-to-Water Ratio Calculation

Color infrared (CIR) aerial imagery was used to supplement the morphological analyses. The CIR imagery was classified to determine the ground state as either dry land or open water. Computing the land-to-water ratio (LWR), calculated with a sliding window operating on the classified CIR imagery, generated a georeferenced raster for further analysis. LWRs provide a quantitative method to assess the backbarrier wetlands' state of deterioration, i.e. conversion into open water. An early example of this methodology can be found in Gagliano et al. (1970) where the 50% LWR contour is tracked through time to analyze spatial patterns of LA's coastal landloss. The CH's backbarrier wetlands are deteriorated and appear to be transitioning into open water. To investigate the relationship between the coastal morphodynamics and the backbarrier's deteriorated state, LWRs were computed at the beginning of the study period (1998) and the end (2013).

The LWRs were determined following the general method outlined in Twilley et al. (2016) and Siverd et al. (2018). Two sources of one-meter resolution aerial imagery were acquired. The 1998 digital orthophoto quarter quadrangle (DOQQ) CIR imagery for the study area was acquired from The LSU Department of Geography and Anthropology (1999) and the 2013 National Agriculture Imagery Program's (NAIP) DOQQs were downloaded with the USGS's EarthExplorer tool (`https://earthexplorer.usgs.gov/`). The green and near-infrared bands from both image sources were used in the LWR computations. The 1998 imagery was initially captured with photographic film and the 2013 imagery was acquired with digital charge-coupled devices. Thus there are significant differences between the spectral signatures, i.e. reflectance in each spectral band, produced by each image source and computations between them are not quantitatively equivalent. However, they acquisition methods produce qualitatively comparable CIR images that can be used to track the CH's evolution over the study period.

The normalized difference water index ($NDWI$) was computed per tile based on the formulation in McFeeters (1996) given as:

$$NDWI = \frac{\rho_g - \rho_{NIR}}{\rho_g + \rho_{NIR}}, \tag{2.2}$$

where ρ_g is surface reflectance in the green spectral band and ρ_{NIR} is reflectance in the near-infrared (NIR) band. Per-tile $NDWI$ distributions were visually inspected to determine the threshold for differentiating between land and water pixels within the tile (typically, this value was approximately 0.3). This threshold was used to separate the rasters into binary images containing pixels classified as either land or water (i.e. land = 1 and water = 0). In other words, pixels which contained $NDWI$ values less than the threshold (i.e. exhibited a greater reflectance in the NIR band which is mostly absorbed by water but is reflected by healthy plant cell structure) are expected to represent land and vice versa. The binary images were merged and clipped to extract the backbarrier within the bounds of Highway 1, Port Fourchon, and the CH's shoreline.

Land-to-water ratios were calculated within a neighborhood window and assigned to the window's center pixel. The neighborhood-averaging moving window operator applied to the merged binary images can be expressed as:

$$LWR_{ij} = \frac{1}{N^2} \sum_{m=i-\frac{N-1}{2}}^{i+\frac{N-1}{2}} \sum_{n=j-\frac{N-1}{2}}^{j+\frac{N-1}{2}} \psi_{mn} \tag{2.3}$$

where LWR_{ij} is the land-to-water ratio in the i^{th} and j^{th} pixel of the image, N is the side-length of the window in pixels, and ψ_{mn} represents the land (1) or water (0) classification of the m^{th} and n^{th} pixel. The result is one-meter resolution geographic gridded data of a continous variable representing the marsh surface's state of conversion into open water. N determines the length scale of the LWR as larger N values will smooth out smaller scale variations in the LWR (see Section A.6 in the online supplement for further details). LWR values are on the interval $[0, 1]$ where the limits represents open water and solid land, respectively. Areas of high LWR represent a more solid marsh surface whereas lower LWR areas indicate relatively more fragmentation and deterioration of the marsh surface into open water. The CH's backbarrier LWRs were visualized with contours (see Figures 2.12 and 2.15). The contours are level curves (e.g. $LWR = 0.3$, 0.4, 0.5, etc.) of the LWR fields and were computed within GRASS GIS. To relate the near-field LWR (i.e. the environment immediately proximal to the coastline) to the morphological parameters (see Section 2.3.2), the LWR rasters were sampled and averaged along the morphometric analysis transects.

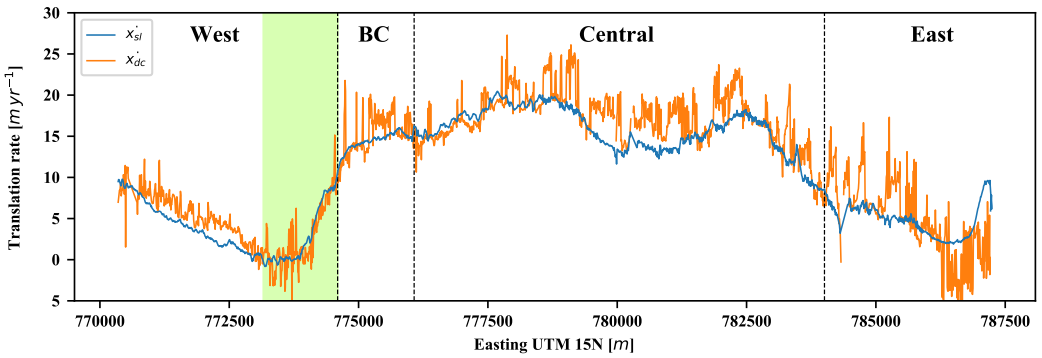

Figure 2.4: Net erosion (blue line) and dune translation (orange line) rate between September 1998 and March 2013. Dashed lines indicate boundaries between morphodynamic zones. The green shaded area shows the breakwater field's location.

2.4 Results

In this section, the CH's overall morphodynamics, storm impact driven change, and relationship to the backbarrier environment will be presented in detail. Before going further, it is worth defining commonly used terms: "net" refers to a change in time between the final and initial lidar survey (e.g. x_{sl} displacement between 1998 and 2013); "mean" refers to the mean of a morphological parameter through time at a fixed alongshore position (e.g. z_{dc} at a single transect or set of adjacent transects); and "alongshore-average" or "average" of a parameter indicates a mean taken over a set of adjacent transects (e.g. average erosion rate for a vulnerable stretch of shoreline).

2.4.1 Definition of Alongshore Zones

Over the study period, the CH's coastal morphodynamics exhibited three distinct zones characterized by shoreline translation and dominant coastal processes. Figure 2.4 shows the boundaries of the western, central, and eastern zones in relation to the net x_{sl} and x_{dc} translation rates. The boundary between the western zone and the central zone/Bay Champagne (BC) can be seen as an abrupt transition in shoreline morphodynamics. The central zone transitions gradually into the eastern zone, but is still discernible in the net translation rates.

Average overwash frequency for each zone is presented in Table 2.3. A cross-shore profile was considered overwashed when R_{high} exceeded z_{dc} for two or more consecutive hourly observations. High-water elevation (see Figure 2.2) between a pair of successive lidar surveys (e.g. 2010 and 2012) was compared to z_{dc} values from the antecedent survey (i.e. the 2010 survey). The number of overwash events is divided by the elapsed time and given as a yearly rate. Also presented in Table 2.3 is the fraction of transects that were overwashed with a higher frequency than the

Table 2.3: Dune overwash statistics. The first, second, and third columns within each zone are the yearly overwash rate, the fraction of transects exceeding the CH's overall overwash frequency, and the fraction without overwash, respectively.

	Zone								
	West			Central			East		
Period	(n yr^{-1})	-	-	(n yr^{-1})	-	-	(n yr^{-1})	-	-
1998–2001	0.26	0.00	0.83	3.16	0.06	0.01	2.92	0.04	0.43
2001–2002	1.97	0.00	0.08	4.78	0.10	0.00	7.84	0.26	0.00
2002–2006	4.98	0.07	0.00	30.34	0.67	0.00	11.78	0.26	0.00
2006–2008a	0.58	0.00	0.93	18.12	0.29	0.12	5.41	0.03	0.47
2008a–2008b	3.18	0.01	0.00	8.55	0.09	0.00	6.79	0.06	0.00
2008b–2010	4.49	0.03	0.00	33.13	0.74	0.00	38.42	0.52	0.00
2010–2012	1.73	0.01	0.18	18.57	0.52	0.00	7.49	0.18	0.00
2012–2013	1.04	0.02	0.92	24.90	0.61	0.02	19.92	0.24	0.41

CH's overall rate and the fraction that was not overwashed.

Table 2.3 provides preliminary insight into each zones' processes as well as trends in the relationship between dune morphology and storm climate. For example, overwash frequency exceeding the overall rate increased in the central zone after the 2008b survey. This increase shows that Hurricane Gustav's impact lowered z_{dc} sufficiently to influence subsequent overwash events and, plausibly, the central zone's capacity to recover. Also, the western zone's relatively low overwash rate contrasts the dominant processes here with the other zones which are overwashed more frequently.

2.4.2 Overall Morphodynamics

Net x_{sl} and x_{dc} displacements and their translation rates are provided in Figure 2.5. The central zone's shoreline translated approximately -225.2 m while the west and east shorelines eroded -51.4 m and -65.9 m, respectively. A similar pattern is evident in foredune translation with x_{dc} migrating landward -247.1 m in the central zone and -61.6 m and -72.8 m in the west and east, respectively.

Translation rates were determined by linearly regressing alongshore-averaged x_{sl} and x_{dc} in time. The erosion rate regressions' coefficient of determinations (r^2) were 0.77, 0.95, 0.95, and 0.77 for the west, BC, central, and eastern zones, respectfully; while dune migration r^2 values were 0.88, 0.95, 0.94, and 0.81 for the same zones. The relatively high r^2 values indicate that at the decadal time-scale steady marine transgression occurred with distinct zonation. The western zone, which is influenced by coastal hardening, showed an erosion rate of -4.4 m yr^{-1} with a lower and upper bound of -11.0 m yr^{-1} and +0.84 m yr^{-1}, respectively. Erosion decreased towards the east and the shoreline becomes stable near the breakwater field (see Figure 2.4).

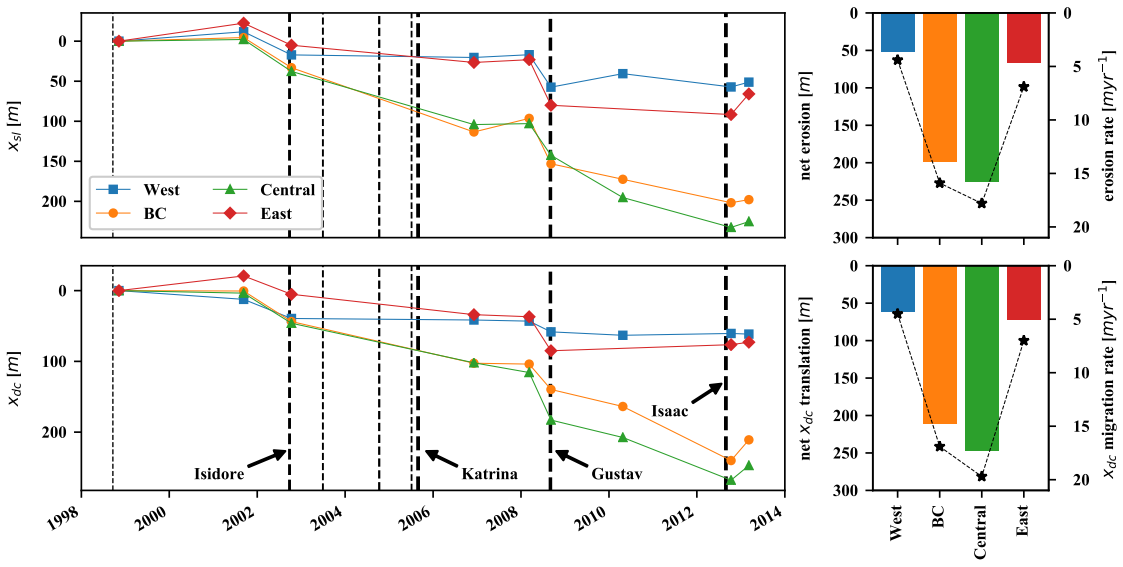

Figure 2.5: Shoreline (x_{sl}) and dune crest position (x_{dc}) time series. The blue (west), orange (BC), green (central) and red (east) differentiate the morphological zones. Vertical dashes represent TC landfalls where the thickness is scaled by the maximum observed water level at GI. The side panels show the net erosion and dune translations (displayed as bars) along with their respective change rates over the study period (broken black line).

The central zone historically exhibited relatively high erosion, overwash, and breaching. Two erosional "hotspots", seen in Figure 2.4 at approximately 777,500 m and 782,500 m easting, are the sites of repeated storm-induced breaching. The erosion rates here range between -8.5 m yr^{-1} and -22.5 m yr^{-1} with an average of -17.8 m yr^{-1}. The eastern zone is an aggradational spit that alternates between accretion, breaching and erosion, and shoreline annealing. Erosion here is comparatively moderate with an average of -6.9 m yr^{-1} and a range of -1.9 m yr^{-1} to -9.6 m yr^{-1}.

Time series of alongshore-averaged x_{sl} and x_{dc} are shown in Figure 2.5. The lidar survey dates are indicated with markers. The 2010 lidar survey for the eastern zone exhibited clearly unrealistic data and was removed from the analysis. Dune crest translation followed the same trends and zonation, but slightly outpaced shoreline retreat. The comparable shoreline and dune translation rates suggest conservation of sediment volume in accordance with the "rollover" model of barrier island transgression. "Rollover" describes landward barrier island movement within a sediment limited setting through overwash processes (Woodroffe, 2002) that is by analogy applied to the CH.

Figure 2.6 shows a time series of z_{dc} and dune volume per zone. Contrary to the coastline's steady landward translation, average z_{dc} oscillates with storm impacts and has a gradual net rate of change. Dune volume displays a similar pattern to z_{dc}. The western zone exhibited a

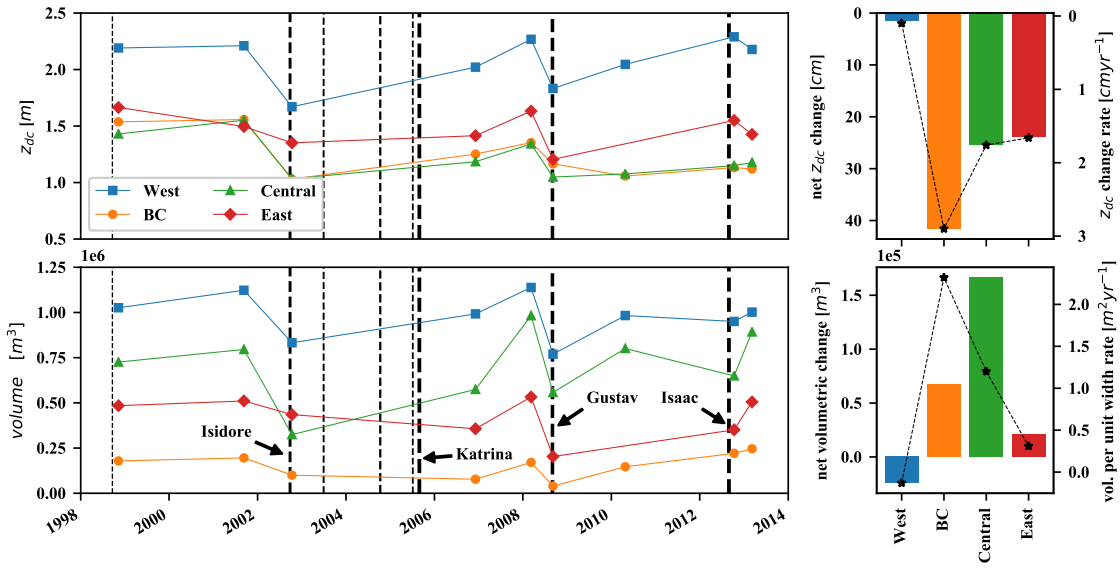

Figure 2.6: Time series of z_{dc} referenced to NAVD88 and dune volume per zone. The blue (west), orange (BC), green (central) and red (east) differentiate the morphological zones. Vertical dashes represent TC landfalls where the thickness is scaled by the maximum observed water level at GI. The side panels show the net dune crest elevation and dune volume change (displayed as bars) along with their respective change rates over the study period (broken black line)

relatively small net volume loss, while an increase occurs in the other zones. Only the central zone's dune volume per unit width showed a correlation with time yielding a volumetric flux of 0.987 m^3 m^{-1} yr^{-1} ($r^2 = 0.158$). Net dune volume change, the rate of change in volume per unit width, and net z_{dc} displacement and change rate can be found in Figure 2.6.

Figures 2.7, 2.8, and 2.9 contain sequential alongshore-averaged dune profiles for the western, central, and eastern zones, respectively. The western zone's morphological change is moderate compared to the others. Initial and final profiles of the western zone, shown in Figure 2.7i, are similar in morphology with some dune crest lowering and translation. The central zone's morphology changed appreciably, resulting in qualitatively different initial and final profiles (see Figure 2.8i). Overall, the central zone exhibits significant morphological change in response to storms impacts. The cross-shore profile is quite diminished in elevation and reduced in coastal-barrier function by 2013 with an average z_{dc} less than 65 cm above MHW. Plausibly the central zone would be frequently overwashed given R_{high}'s historically regular exceedence of this elevation (see Figure 2.2A). The eastern zone changes noticeably between surveys. Its initial and final profiles, however, are similar in morphology, but translated landward and reduced in elevation.

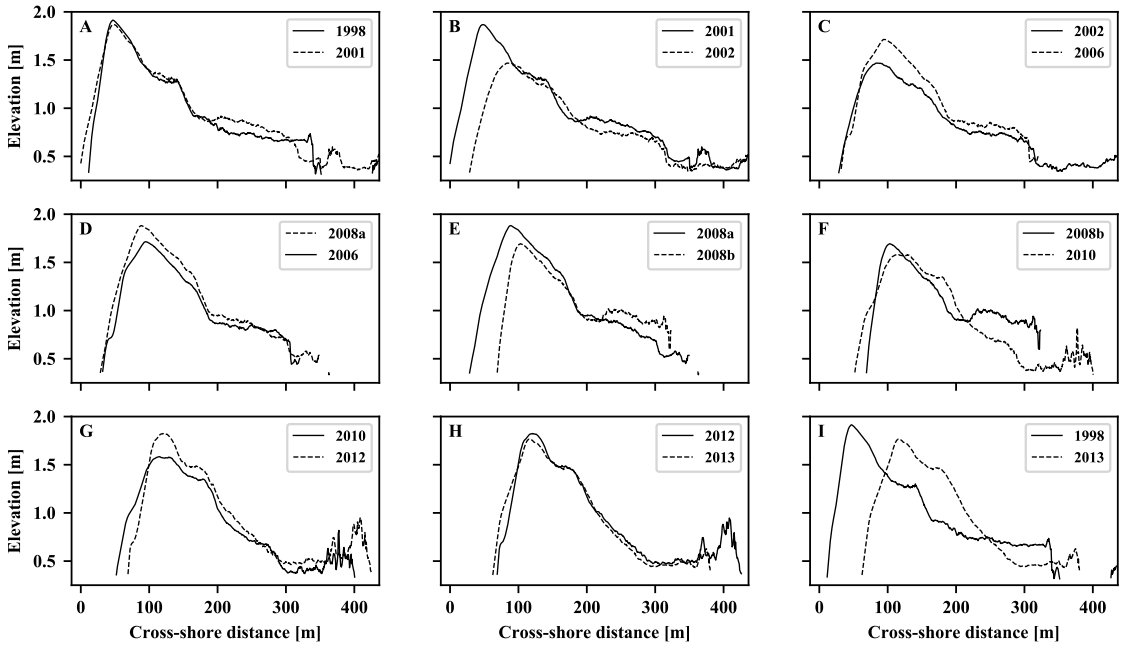

Figure 2.7: Alongshore-averaged cross-shore profiles for the western section. Panels A through H show data from two sequential lidar surveys. The solid and dashed lines are the antecedent and subsequent profiles, respectively. Panel I contains the initial and final survey in the time series.

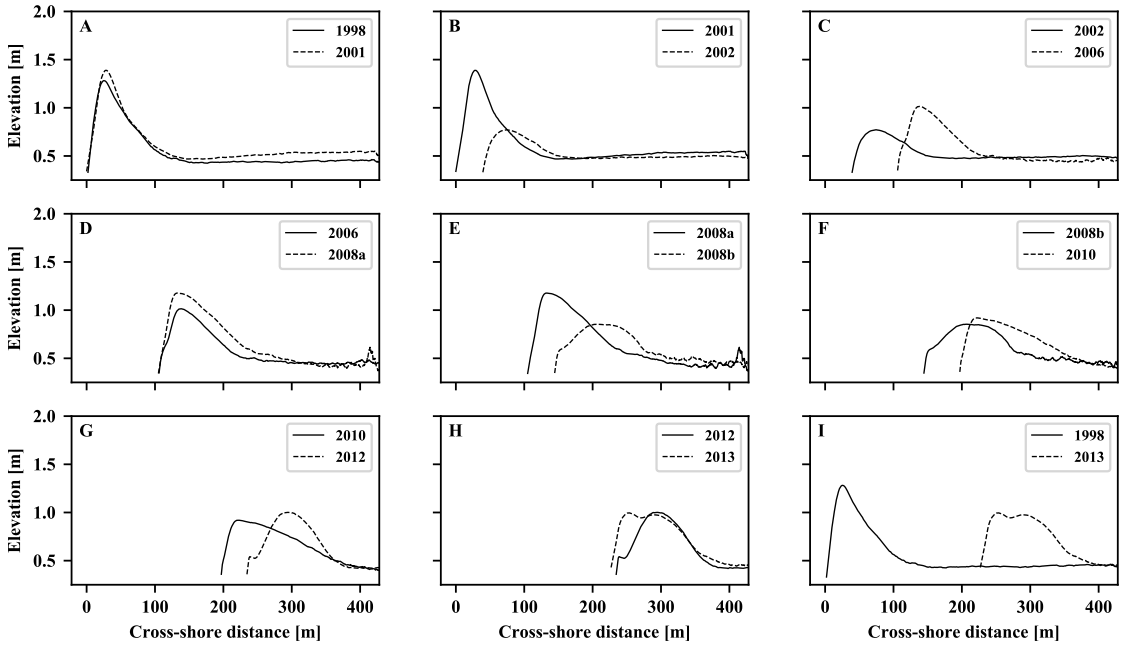

Figure 2.8: Alongshore-averaged cross-shore profiles for the central section. Panels A through H show data from two sequential lidar surveys. The solid and dashed lines are the antecedent and subsequent profiles, respectively. Panel I contains the initial and final survey in the time series

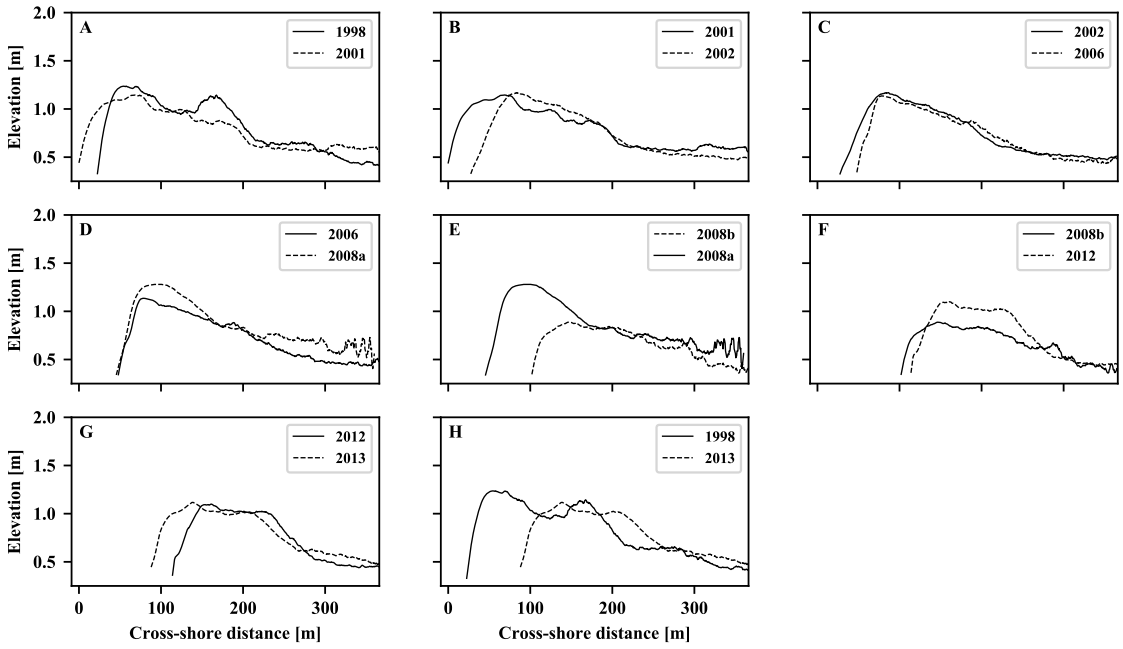

Figure 2.9: Alongshore-averaged cross-shore profiles for the eastern section. Panels *A* through *G* show data from two sequential lidar surveys. The solid and dashed lines are the antecedent and subsequent profiles, respectively. Panel *H* contains the initial and final survey in the time series. The 2010 survey has been removed due to spurious lidar data.

2.4.3 Storm Impacts

The CH's storm driven coastal morphodynamics are visualized with a set of time stacks. The time stacks were created by gridding the morphological parameters based on alongshore location, represented by the easting coordinate, and the lidar surveys' date using a 2D cubic spline. Named TCs from Table 2.1 are indicated to illustrate impacts and cumulative effects on the coastal morphology.

Erosion rate is presented in Figure 2.10. The sequence of storms between TS Isidore and Hurricane Katrina produced the longest period of erosive conditions. The CH's shoreline is mostly erosional over this period, except for the breakwater protected area (773,500 to 774,500 easting). Several breaches (areas of erosion in excess of -120 m yr^{-1}) formed in the central zone with a relatively large breach opening in the bay mouth bar enclosing BC (775,000 easting). A recovery period follows this storm sequence with shoreline accretion in the west, east, and most of the central zone.

Hurricane Gustav generated the largest impact with many areas undergoing erosion rates greater than -100 m yr^{-1}. The breaches at BC and in the central zone were re-opened and enlarged. Erosion of the central zone continues after Hurricane Gustav, but is lessened, and

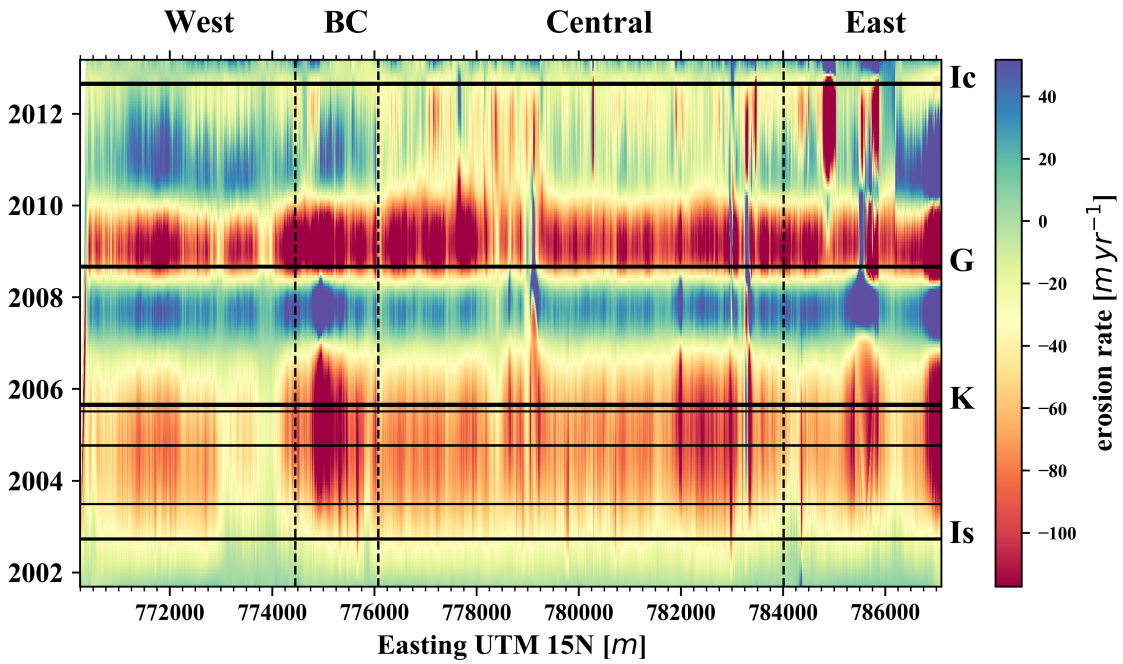

Figure 2.10: Erosion rate time stack. The x-axis is the shoreline's easting coordinate while the y-axis represents time. TC impacts are represented as horizontal lines where Is, K, G, and Ic denote Hurricanes Isidore, Katrina, Gustav, and Isaac, respectively.

shows some recovery following Hurricane Isaac. Relatively high erosion and rapid accretion associated with natural shoreline annealing following TC impacts occurs in the eastern zone.

The top panel of Figure 2.11 shows z_{dc} over the study period. The spatial patterns here largely recapitulate those of Figures 2.10. The most apparent trend in z_{dc} is the central zone's long-term elevation loss initiated by TS Isidore. The western and eastern zones show fragmented recovery towards pre-TS Isidore dune crest elevations. BC and the central zone, however, appear to have uniformly lost elevation between 1998 and 2013. Another notable pattern is the apparent alongshore re-distribution of dune volume seen in the bottom panel of Figure 2.11. Distinct accumulations of volume can be seen in 1998. However, by 2013, much of the accumulated sediment has been transported laterally, resulting in a more alongshore-uniform distribution. This is most evident in the westward dunes of the western zone.

Alongshore-averaged changes to x_{sl}, x_{dc}, z_{dc}, and dune volume captured by post-storm lidar surveys are provided in Table 2.4. Hurricane Gustav and TS Isidore produced relatively large x_{sl} and x_{dc} translations with approximately commensurate decreases in z_{dc} and dune volume. Hurricane Katrina and the other 2005 TCs affected the western and eastern zones less than the central, with x_{sl} displacements of -3.3 m, -21.5 m, and -66.4 m, respectively. Hurricane Rita (2005) made landfall 24 days after Hurricane Katrina, approximately 325 km to the west

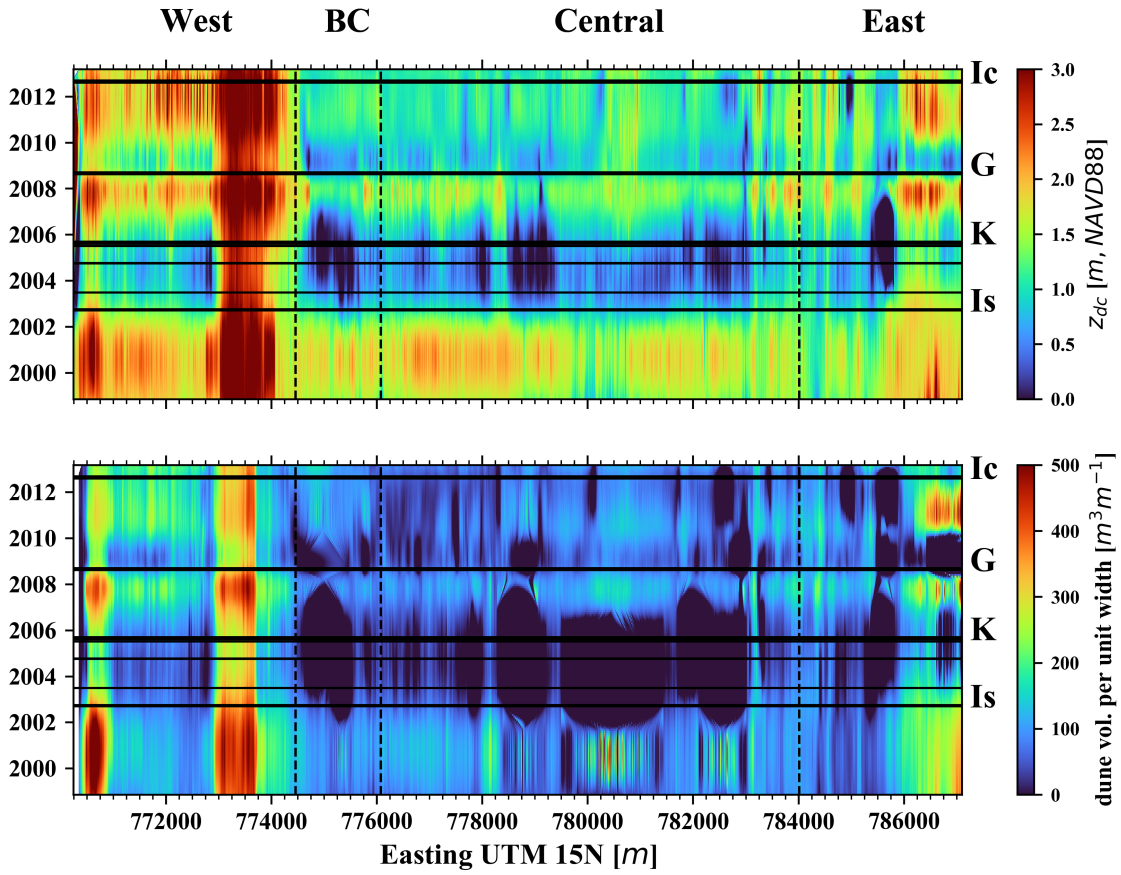

Figure 2.11: (top) Dune crest elevation. (bottom) Dune volume per unit width. TC impacts are indicated with horizontal lines where Is, K, G, and Ic denote Hurricanes Isidore, Katrina, Gustav, and Isaac, respectively.

as a powerful category 3. Hurricane Rita's maximum observed water level at the GI station was 1.089 m MSL. This storm plausibly impacted the CH within the collision and overwash regimes and partially forced the morphodynamic response observed in the 2006 lidar. Counter to one's expectation, given Hurricane Katrina's wide-spread impact, dune crest elevation and dune volume in the 2006 lidar exhibited some increases. One possibility is that the CH's antecedent condition (see in particular the central zone in Figure 2.8C) lessened the overall severity of the impact as the dunes were already morphologically adjusted to inundation regime forcing. However, it is difficult to assess Hurricane Katrina's impact using this lidar. The time elapsed between Hurricane Katrina and survey was 464 days, during which time the coastline may have recovered substantially.

Hurricane Isaac was a major storm surge producing hurricane (see Figure 2.2) whose peak water levels coincided with high tide at the CH. Considering storm waves and water levels, Hurricane Isaac forced an impact within the overwash and inundation regimes with a maximum water level (1.51 m NADVD88) observed at the GI station exceeding z_{dc} at 62% of the pre-storm transects. This is corroborated by hindcast simulations which produce a maximum water level of approximately 1.5 m NAVD88 and a significant wave height reaching 4 m (water levels and waves provided by the Coastal Emergency Risk Assessment `https://cera.coastalrisk.live/`). As such, this event was expected to generate greater morphological change than that observed in the 2012 post-storm lidar. Storm surge relative to dune crest elevation is the predominant control on morphological change, but no single parameter can entirely explain storm impact response (Masselink and Van Heteren, 2014). Hurricane Isaac made landfall approximately in the CH's center (see Figure 2.1) and the relationship between its shoreline orientation (SW to NE) and Isaac's NW track is an important factor. Morton and Sallenger Jr. (2003) also observed that maximum washover penetration (and hydrodynamic forcing) occurs approximately 20–50 km east of the TC's eye which places the CH outside this window for Isaac's landfall. Ultimately, it is the synchronization and combination of variables, including locally weak hydrodynamic forcing, the previous state of the dunes, and the interaction between the shoreline orientation and the landfalling storms' wave fields, that produced the CH's relatively minimal morphodynamic response to Hurricane Isaac (Guisado-Pintado and Jackson, 2018).

Morphodynamics observed during recovery periods (i.e. consecutive surveys without a TC impact) are presented in Table 2.5. The surveys lack the temporal resolution required to accurately determine recovery rates. However, it is adequate to demonstrate broad patterns and trends. The CH's shoreline is generally accretionary outside TC impacts, except within the cen-

Table 2.4: Dune and shoreline changes due to storm impacts.

TC name	Zone	x_{sl} displacement (m)	x_{dc} displacement (m)	z_{dc} change (cm)	dune volume change (m^3)
Isidore	West	-28.9	-27.0	-54.0	-290296.7
	BC	-37.7	-43.3	-52.8	-95631.8
	Central	-39.8	-42.5	-51.6	-471045.9
	East	-27.6	-25.9	-14.4	-75434.8
Katrina	West	-3.3	-2.2	35.1	159803.9
	BC	-80.3	-59.2	22.0	-22285.9
	Central	-66.4	-56.0	15.0	249996.5
	East	-21.5	-28.7	6.3	-78491.2
Gustav	West	-40.6	-15.2	-43.5	-369045.4
	BC	-56.5	-36.3	-19.2	-130960.4
	Central	-39.6	-67.1	-29.3	-424823.4
	East	-57.3	-48.3	-42.9	-329451.1
Isaac	West	-16.6	2.5	24.3	-32856.2
	BC	-29.4	-76.6	7.6	74377.8
	Central	-37.3	-60.3	7.3	-151495.7
	East	n/a	n/a	n/a	n/a

tral zone for the 2008b to 2010 interval. Despite the seaward movement of x_{sl} during recovery periods, x_{dc} typically translated landward. The dunes invariably increase in volume between impacts, but not always through an increase in z_{dc}. In general, however, z_{dc} recovers a fraction of its pre-storm elevation between impacts.

2.4.4 Coastal Morphodynamics in Relation to the Backbarrier Environment

A correlation between net erosion rate and the backbarrier environment can be observed in Figure 2.12. The LWR contours indicate, in a relative sense, spatial variation in the backbarrier wetland's conversion into open water. Three areas of relatively low LWR can be discerned: one associated with BC to the west; a central area which extends to Highway-1; and an eastern area that is constrained by chénier ridges. Directly seaward of these areas, localized "hotspots" of erosion can be observed. These "hotspots" are commonly breached during TC impacts.

In Figure 2.12B, mean LWR along a transect is plotted along with the net erosion rate observed at that transect. Mean LWR represents the backbarrier's near-field condition as the transects were less than 450 m in length. This length was chosen to quantify the LWR between the shoreline and natural landward ridges. A west-to-east trend of decreasing erosion rate, plausibly due to the direction of alongshore sediment transport (Harper, 1977; Georgiou et al., 2005), has been removed in order to highlight the LWR relationship. A coherence between LWR and net erosion within the central zone is present with the signals in approximate antiphase.

Table 2.5: Dune and shoreline recovery between TC impacts.

Recovery period	Zone	x_{sl} displacement (m)	x_{dc} displacement (m)	z_{dc} change (cm)	dune volume change (m^3)
1998–2001	West	11.7	-12.3	1.9	96678.1
	BC	4.4	-0.6	2.4	16737.6
	Central	2.1	-3.6	12.1	69715.8
	East	22.4	20.7	-16.9	26246.9
2006–2008a	West	3.4	-1.6	24.7	146038.0
	BC	16.9	-1.0	10.0	93042.0
	Central	1.2	-13.7	15.7	407998.1
	East	3.6	-2.9	21.7	176040.2
2008b–2010	West	16.8	-4.9	21.2	213853.2
	BC	-19.5	-23.7	-10.2	106766.7
	Central	-52.7	-24.6	2.8	243071.0
	East	n/a	n/a	n/a	n/a
2012–2013	West	6.0	-0.9	-11.2	51651.9
	BC	3.8	29.4	-1.4	25397.5
	Central	7.2	20.7	2.8	243002.4
	East	25.7	3.3	-12.4	154236.7

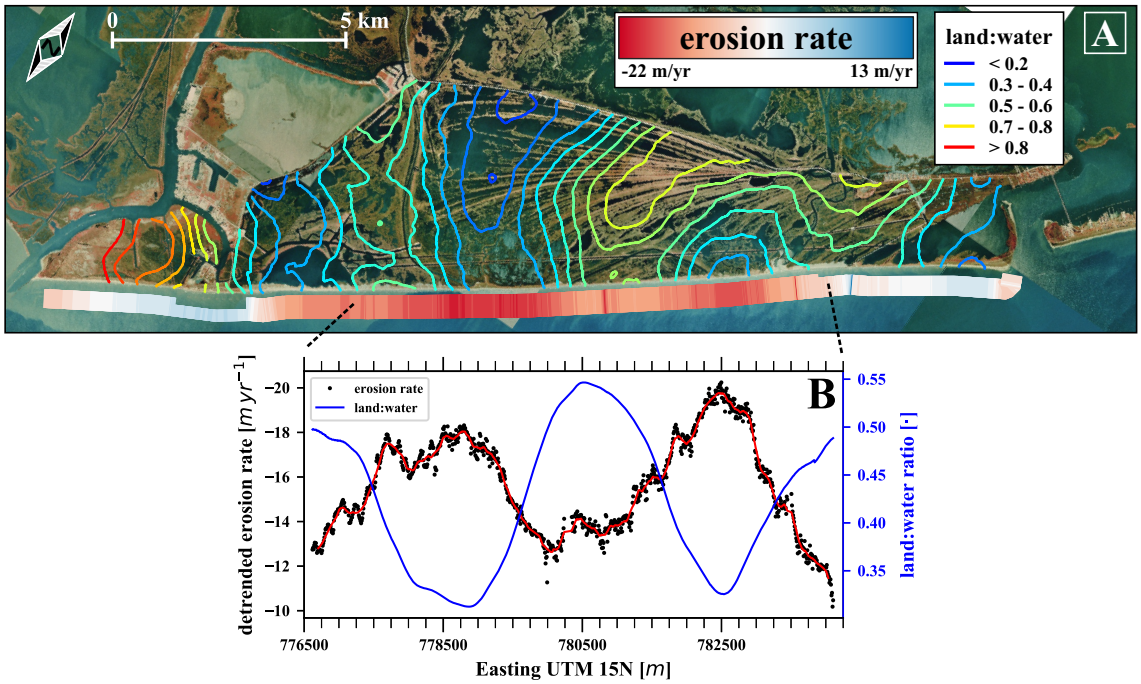

Figure 2.12: Spatial relationship between net erosion rate and near-field backbarrier LWRs. (A) 1998 CIR aerial photography with LWR contours superimposed on the backbarrier environment. Net erosion rate shown where the cross-shore transects have been shifted offshore for the visualization. (B) Net erosion rate and mean LWR plotted as a function of alongshore position. Black markers indicate net erosion rate data points with an alongshore running average shown as the red line. Solid blue line is the LWR.

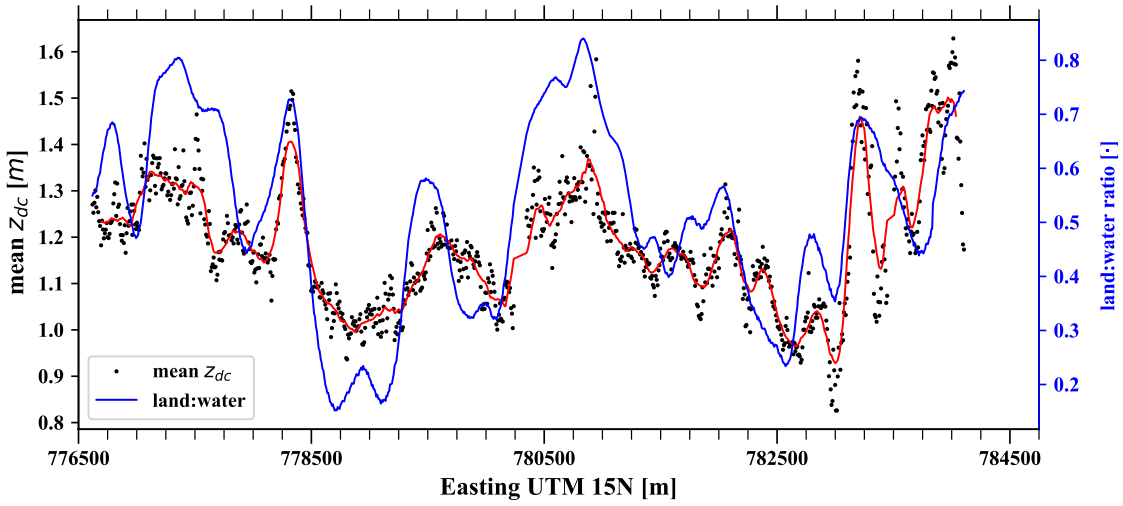

Figure 2.13: Mean z_{dc} elevation in NAVD88 versus LWR calculated using a 25 m window. A running average of z_{dc} is shown as a blue-green line.

Mean z_{dc} exhibits an approximate in phase coherence with the LWR and evidently contains significant shorter wavelength components. This can be seen in Figure 2.13 which shows mean z_{dc} per transect in relation to mean LWR (computed using 25 m window to capture the shorter length scale variations in z_{dc}). The spatial extent of Figures 2.12B and 2.13 are aligned and displayed as scatter plots in Figure 2.14. Lines of best fit, computed with least-squares regression, have been added to indicate the dependency of the morphological parameters on LWR. A negative correlation between LWR and detrended net erosion rate ($r^2 = 0.67$) is clear, while a positive correlation between LWR and mean z_{dc} ($r^2 = 0.48$) is present but less determined. This indicates that coastline exhibiting relatively higher mean z_{dc} coincide with stretches where net erosion rate is relatively less; and that both of these parameters are related to the near-field LWR.

Complexity in the processes involved (e.g. wave-current-vegetation interaction, overwash and aeolian sediment transport) presumably reduce the efficacy of determining these correlations. Unrepresented changes to the backbarrier wetlands occurring after the initial aerial photography may also contribute to indeterminacy in the explanation of the net shoreline erosion rate's variance by the CH's initial LWR. In Figure 2.15, it can be seen that the CH's backbarrier wetland evolved over the duration of the study period (15 years). As expected, the general trend is the conversion of land into water and is most evident in the central zone. However, the overall spatial pattern of the LWR contours is largely consistent between 1998 and 2013. For the purposes of the current research, the net shoreline erosion and mean dune height over the study period, where fluctuations due to storm impact/response cycles are reduced, is related

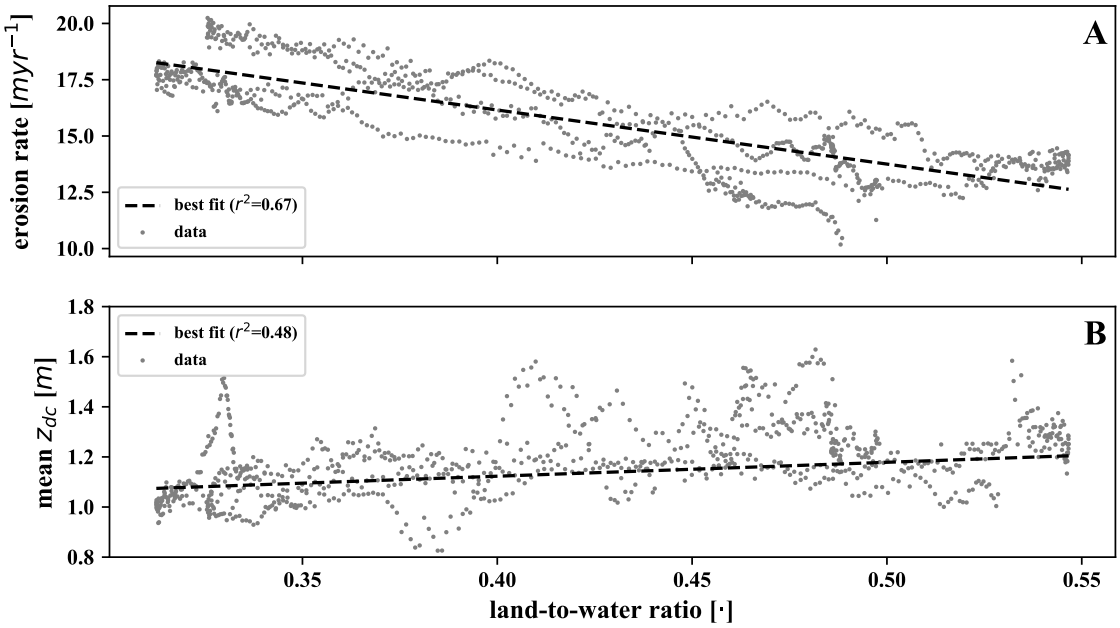

Figure 2.14: (A) Relationship between net erosion rate and LWR. (B) Mean dune crest elevation over the study period versus LWR.

to the backbarrier wetland's initial condition to demonstrate their connection for low-elevation, wetland-backed mainland barriers. Presumably, the backbarrier wetlands' evolution, driven in part by TC impacts, influences the shoreline and dune morphodynamics over the study period and should be considered. Additional research that incorporates aerial imagery at a higher temporal resolution is required to robustly analyze the wetlands' evolution and relate this to the coastal morphodynamics, but is out of the current research's scope.

2.5 Discussion

2.5.1 Morphodynamic Trends

Due to differing dominant coastal processes, each zone's morphodynamics should be discussed separately to better facilitate interpretation of their interrelation. The western zone shows a spatial distribution of erosion rates consistent with an alongshore sediment transport gradient introduced, in this case, by a breakwater field. An increase in erosion westward from the breakwaters can be seen in Figure 2.4. This is counterintuitive given that the western zone abuts a 600 m jetty that is expected to sequester sediment on its updrift side, i.e. to east of Belle Pass. Eroded sediment might bypass Belle Pass though an offshore pathway. This sediment would be transported to West Belle Pass and the Timbalier Islands. However, this quantity is likely small given the high rates of shoreline erosion and land loss in these areas. Offshore or overwash

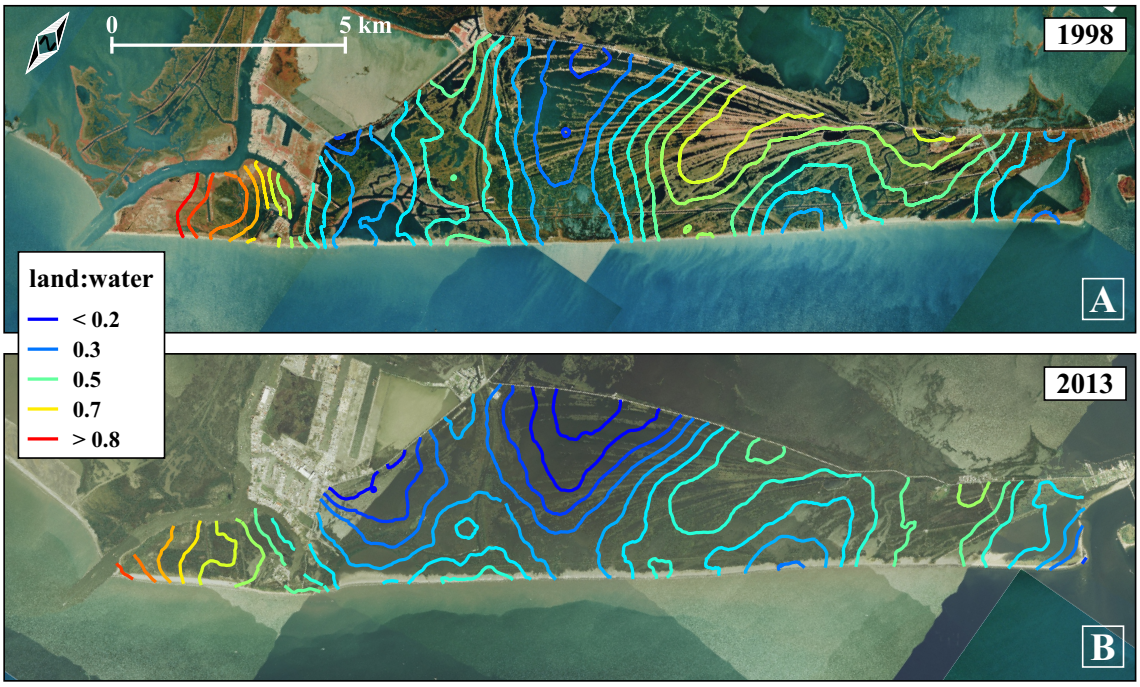

Figure 2.15: Comparison of LWR contours between the beginning (A) and end of the study period (B). Notice that more land has been converted into water over the study period, but the general spatial pattern is consistent.

transport is therefore a more likely pathway for the eroded sediment. Sufficient washover must occur to maintain a constant dune volume, as it is nearly conserved over the study period while x_{dc} and x_{sl} translated landwards approximately 60 m (see Figures 2.5 and 2.6). The fact that x_{dc} and x_{sl} are relatively stable between TC impacts suggests that the majority of the eroded sediment is transported offshore during major storms. An alternative explanation is that eroded sediment does bypass Belle Pass and is deposited in a flood-tidal shoal within Timbalier Bay (Kulp et al., 2002).

The eastern zone displayed the highest variability with respect to storm-impact response. Storm impacts nearly removed its entire dune volume, as seen with TS Isidore and Hurricanes Katrina and Gustav in the upper panel of Figure 2.11. However, between two successive storms, dune volume typically recovered a greater amount relative to its post-storm state than observed in the other zones. This is especially the case near Caminada Pass. The spit quickly built elevation (see the bottom panel of Figure 2.11), but was easily disintegrated. From the observations, one can assume that TC impacts eroded sediment from the central zone which was subsequently transported eastward to rebuild the eastern zone during recovery, supporting the hypothesis of Harper (1977).

The central zone exhibits landward shoreline and foredune translation under normal condi-

tions as well as post-storm impact. Minimal shoreline recovery between the impacts does occur as the shoreline accreted 2.1 m, 1.2 m, and 7.2 m between the survey pairs 1998–2001, 2006–2008a, and 2012–2013, respectively (see Table 2.5). Compared to the net landward translation of the central zone's shoreline (222.5 m) this process plays a minor role. The spatial pattern in net erosion rate, which decreases towards the east and west (see Figure 2.4), suggests a sediment transport divergence node exists in the central CH, as previous research has concluded (Harper, 1977; Georgiou et al., 2005). However, in light of the storm impact response/recovery dynamics, it appears less effective as a background process and controls shoreline morphodynamics in conjunction with major TC events. Overall, dunes within the central zone gained volume while losing elevation. This can be seen in the temporal change in dune volume and z_{dc} in the lower and upper panels of Figure 2.11, respectively. At the same time, landward migration of x_{dc} outpaced x_{sl} resulting in dune flattening. Figure 2.8 portrays the transition in morphology well, where the initial relatively high foredune is successively lowered and widened.

Alongshore-averaged dune profile change within the central zone appears different than those of the west and east, found in Figure 2.8I and in Figures 2.7I and 2.9H, respectively. The initial and final profiles of the central zone are qualitatively different, whereas those of the western and eastern zones have been lowered and translated but appear morphologically similar. This indicates that a state change occurred or was occurring in the central zone over the study period, plausibly as the result of significant perturbations forced by TC impacts. Coastal equilibrium states are identified through conspicuous morphology and are said to transition when a threshold is crossed in response to external boundary conditions or systemic perturbations (Woodroffe, 2007). In particular, metastable equilibrium is defined by punctuated, rapid change followed by a more gradual return to the previous conditions and, as such, is a useful conceptual model for storm impact response and recovery (Woodroffe, 2007). See Figure 2.16 for a conceptual diagram illustrating how a system in metastable equilibrium responds to storm-impact forcing with respect to morphological state (e.g. dune volume or z_{dc}). Equilibrium states themselves are supported by negative feedbacks which work to stabilize morphology, e.g. storm bar welding and increased backbarrier sediment volume through washover deposition and aeolian transport.

The CH's barrier morphology clearly exhibits metastable equilibrium characteristics over the study period (see the impact/recovery cycles in Figure 2.5). As such, the CH's evolution partially supports the model of frequently overwashed barriers (FOB) proposed by Matias et al. (2009) based on the Ria Formosa barrier islands, Portugal. The FOB model describes the cyclic evolution of sediment transport and morphodynamics in low-lying barriers that, as a consequence

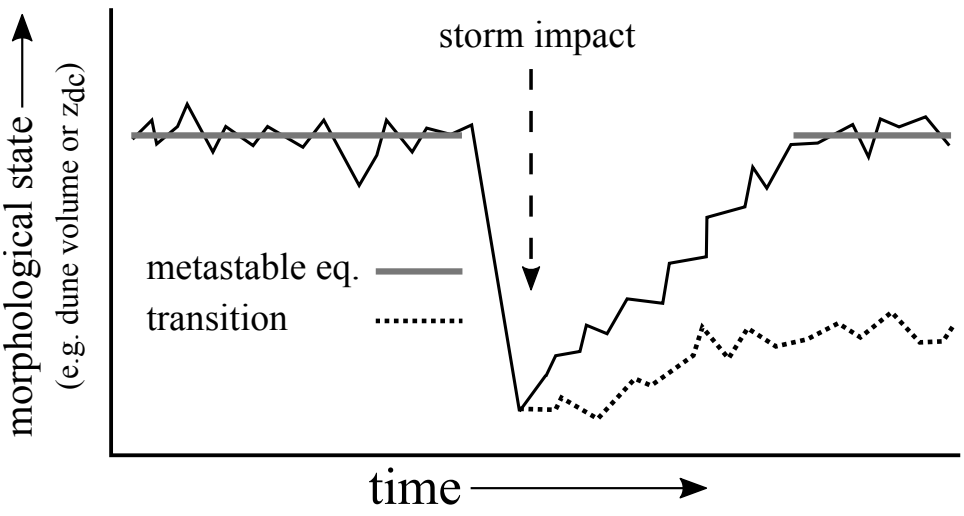

Figure 2.16: Conceptual diagram of a system in metastable equilibrium subject to a significant storm impact.

of limited sediment supply and stunted dune growth, are subject to frequent overwash. The FOB model consists of four stages: (1) a quiescent or recovery period, which depends on a non-negative sediment budget, where overwash is uncommon and aeolian processes lead to dune growth; (2) swash zone and dune erosion due to storm impacts or a re-configuration of sediment transport patterns; (3) if erosion continues, the overwash-prone barrier is subject to complete overwash that promotes dune destruction and the development of a wide and low washover plain; (4) frequent overwashing that includes lesser storm conditions. See Figure 2.17 for a conceptual diagram of the CH's evolution over the study period with respect to the FOB model. Note that the initial stage has been changed to highlight storm-impacts and a return to metastatic equilibrium, i.e. stage 1 in Figure 2.17 corresponds to stage 4 in (Matias et al., 2009), but the ordering of the stages is the same.

Applying the FOB model to the current study allows a useful conceptualization: the eastern zone follows the FOB model's sequence of stages; the western zone never initiates stage 3 due to coastal infrastructure; and, in the central zone, stage 1 does not commence following Hurricane Gustav's impact. The initial survey period (1998–2001) captured in panel A of Figures 2.7– 2.9 corresponds to stage 1 as the profiles exhibit morphological stability or minor accretion (nevertheless, the dynamic eastern zone exhibits transfer of dune sediment to the beach). Hurricane Isidore's impact perturbs the system causing massive beach and dune erosion with a system wide dune volume loss of approximately 9.3e5 m^3 (35.6% of the 2001 volume) and shoreline erosion of 27.6 m to 39.8 m (see morphodynamics in panel B of Figures 2.7– 2.9). Stage 3 does not

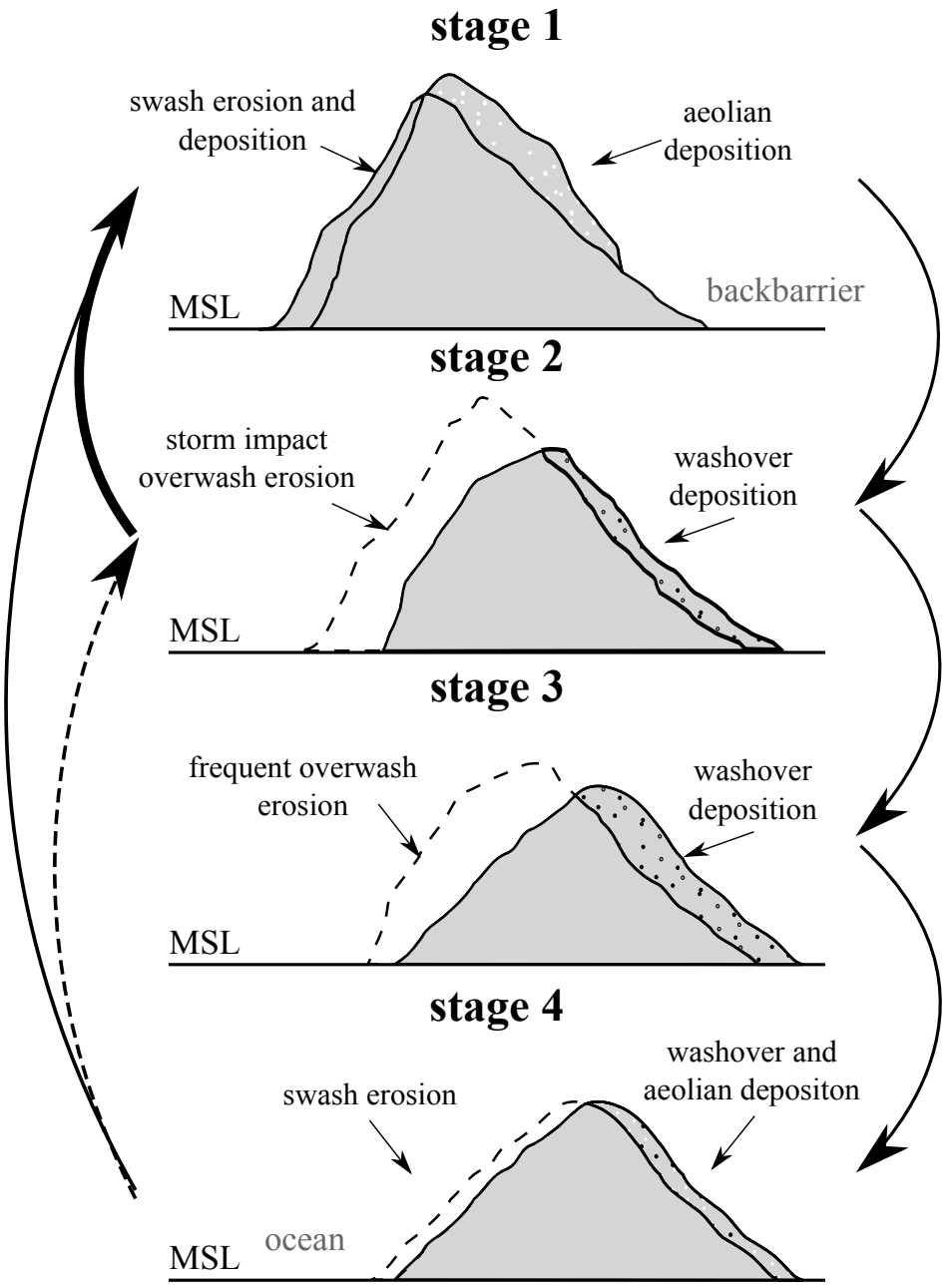

Figure 2.17: Stages in the evolution of a low-lying, frequently overwashed barrier. The right-hand side arrows indicate the sequence of stages following the impact of a significant TC. The left-hand arrows indicate recovery trajectories exhibited by the CH's different alongshore zones. The thicker arrow represents the western zone, the solid line represents the eastern zone, and the broken line indicates the central zone not recovering to stage 1 after Hurricane Gustav's impact. Adapted from Matias et al. (2009).

occur in the western zone as during the 2002–2006 period aeolian processes rebuild the dune and minimal swash zone or shoreline erosion occurred (see Figure 2.7C). In the central zone, stage 3 and 4 clearly occurred following Hurricane Isidore (see continued erosion and landward washover transport in Figure 2.8C and the annual frequency of overwash in Table 2.3). This is plausibly explained by a negative sediment budget (sediment mobilized from the central zone feeds the east and west) and a more overwash-prone post-storm dune morphology (alongshore average $z_{dc} < 1$ m). There is some evidence that the eastern zone underwent stages 3 and 4, as there is net dune volume loss (-18%) and minimal z_{dc} growth (+6.3 cm) between 2001–2006, but recovery is rapid and it does not exhibit prolonged erosion. The period 2006–2008a (see panel D of Figures 2.7– 2.9) indicates that beach erosion and dune retreat have ceased and aeolian processes are promoting dune growth, signaling a return to stage 1 and a completion of the metastable equilibrium cycle. The sequence of stages approximately repeats itself with the impact of Hurricane Gustav (captured in panel E of Figures 2.7– 2.9) in the western and eastern zones. However, the central zone does not clearly exhibit a return to stage 1 characteristics, although there is minimal accretion and dune growth by 2013 (see Figure 2.8H).

The deviation from the FOB model following Hurricane Gustav within the central zone, as opposed to the western and eastern zones which conform relatively better to the FOB model, suggests that the central zone crossed a threshold (or was crossing a threshold) and was no longer in metastatic equilibrium. Lasting morphological changes to low-gradient, low-elevation coastline have been observed and/or inferred elsewhere following storm impacts. Evidence from Santa Rosa, FL, impacted by Hurricane Ivan (2004), suggests that post-storm recovery (stage 1) depends on nearshore sediment availability and, consequently, pre-storm dune heights (Houser et al., 2008, 2015). Pre-storm dune height was observed to control washover sediment volume which, for that site, has limited recovery potential due to weak offshore winds. The system's susceptibility to crossing an irreversible threshold therefore depends on the relatively higher dunes' recovery before the next impact, because the low or discontinuous dunes will continue overwashing and lose unrecoverable sediment to the backbarrier. The relatively higher dunes in the central zone show limited, discontinuous recovery between 2002–2008a and are then approximately flattened and do not recovery following Hurricane Gustav in the period 2008b–2013 (see 777,000 m–779000 m easting and 781000 m–783000 m easting in Figure 2.11). Similar to the morphodynamics observed in the CH's central zone, Houser et al. (2015) suggest that the transition to a lower, flatter barrier profile signals a new equilibrium response. Eisemann et al. (2018) observed unrecovered sediment loss following Hurricane Katrina (2005) at low-lying Ship

Island, MS over an eight year period and attributes this primarily to a systemic sediment deficit. They further observe that sediment transferred to the shoreface during an impact is more likely recovered, while washover sediment transport does not contribute to subaerial recovery as the barrier island lacked a marsh platform for proximal deposition.

Harter et al. (2015) observed five years of lidar data following Hurricane Ike's (2008) impact to Follet's Island, TX ($z_{dc} \leq 3$ m) which exhibited complete recovery of dune volume, elevation, and shoreline position. Their observations largely conform to the FOB model's sequence of states. They attribute dune regrowth to bay to barrier aeolian transport of washover fan sediment. In the central zone, bay to barrier aeolian transport at overwash-prone sections is presumably limited due to relatively lower LWR which appears to influence mean z_{dc} over the study period (see Figure 2.13 and Section 2.5.2). Based on a 4000 year stratigraphic record, Odezulu et al. (2018) argue that this situation at Follet's Island will change in the future (approximately 260 years), as limited sediment supply and frequent overwashing will progressively winnow the subaerial washover deposition and lead to drowning/disintegration of the barrier. The CH and Follet's Island exhibit similar geological and geomorphic characteristics. They are both deltaic barriers with thin (1 m) shoreface sandy sediment overlying clay strata, are low-gradient and low-elevation, and storm-impacted. Follet's Island, however, experiences average erosion rates of approximately 2 m yr^{-1} (Odezulu et al., 2018), while the historical rate at the CH is on the order of 10 m yr^{-1} (Williams et al., 1992). This suggests that the CH's central zone may be considered an accelerated version of Follet's Islands transgressive dynamics and can serve as analogous system for diagnosing deviations from a metastatic equilibrium subject to storm impact perturbations. This comparison illustrates that the transgressive processes and resulting morphodynamics which shaped LA in the 19^{th} and 20^{th} centuries, due to subsidence-driven RSLR, sediment deprivation, and frequent TC impacts, can serve as analogues for the future evolution of other low-gradient coastlines due to projected changes in related forcings, e.g. accelerated sea-level rise, increased storminess, and decreasing sediment supply.

The central and eastern foredunes zones lost elevation at net rates of approximately 2 cm yr^{-1} despite their conservation of dune volume. It is hypothesized in Ritchie and Penland (1988) that dune recovery at the CH follows a 10 year cycle between major storm impacts. The analyses presented here, which encompasses more than 2 major TC impacts, roughly supports this hypothesis but with a recover period for dune volume which is less than 10 years. However, dune crest elevation relative to MSL may follow a different recovery trajectory. MSL rose at a rate of 3.49 mm yr^{-1} (calculated from the GI tidal station as the difference between the observed

rate of RSLR and the vertical land movement rate observed at the co-located National Geodetic Survey's Continous Online Reference Station) and alongshore-averaged z_{dc} decreased over the study period; therefore, the period required to recover dune volume may not be sufficient to sustain a metastable equilibrium in z_{dc}. One can assume that the impact of TS Isidore lowered the CH's central zones' dunes past a threshold for recovery given the frequency of storm impacts that followed (Houser et al., 2015). The western zone appears less vulnerable due to coastal infrastructure. In addition, both the western and eastern zones are plausibly supported by negative feedbacks involving return of eroded sediment from the nearshore/beach related to alongshore fed sediment dispersal from the central zone and the recovery of subaerial washover deposition.

Drawing definitive conclusions about the TC impacts' long-term effect would require a longer lidar time series. However, there is evidence that the CH's general alongshore distribution of dune morphology has persisted through storm impacts in the past, though detailed historical elevation data is missing. The zonation of z_{dc} elevations in 1998 are similar to those in 1977, a period which encompassed the severe impact of Hurricane Andrew (1993): > 2 m in the west, between 1–2 m in the center, and < 1 m near bayou-shoreline intersections, though the 1977 eastern section had slightly more elevated dunes (Ritchie and Penland, 1988). The lidar analysis also suggests that the CH's intrinsic sediment budget did not change significantly over the study period, but that systemic changes to the central zone were due to the sequence of storm impacts. This is based on the approximate conservation of dune volume and that the dune and shoreline translation rates were relatively steady within each zone.

2.5.2 Effects of Backbarrier Wetland Fragmentation on Low-Lying Coastal Morphology

Due to its narrow width and low elevation, the CH's backshore and dunes exhibit a close connection to the backbarrier wetlands (see Figure 2.12). It is reasonable to assume that the marsh platform's relative state of deterioration into open water modifies cross-shore processes such as overwash and aeolian transport. The CH's low-lying topography is frequently overwashed during the study period (see Table 2.3) and, due to alongshore variability in marsh platform deterioration, the overwash fluxes and storm surge-driven flow interact with both subaqueous and subaerial environments. Backbarrier depositional environment (i.e. subaqueous or subaerial) then plays a significant role on subsequent bay to beach aeolian recovery processes (Harter et al., 2015; Houser et al., 2015). Alongshore variation in sediment transport processes, in turn,

influences the CH's morphology and morphodynamics (Cooper et al., 2018). In Figure 2.12, two areas which exhibit erosional "hotspots" (see approximately 778,500 and 782,500 easting) and chronic breaching over the study period are spatially correlated with relatively lower backbarrier LWR. These areas are also associated with relatively low dune elevations (see Figure 2.13). Along stretches of coastline with relatively higher backbarrier LWRs, dunes are more continous and elevated while the erosion rate is lessened (see Figures 2.10 and 2.11 prior to Hurricane Gustav). With respect to the CH, which is backed by fragmented wetlands, low LWR adjacent the backshore seems to be analogous to narrow barrier island width, which has been related to breaching, overwash susceptibility, and washover penetration (Rosati and Stone, 2007; Houser and Hamilton, 2009; Houser, 2013).

During high water events, an increased hydraulic connectivity between backbarrier water bodies and the ocean reduces bottom friction for overland flow (Boyd and Penland, 1981). Overwash and storm surge-driven current velocities are higher in less vegetated and wetter areas due to decreased surface roughness which increases beach erosion, landward sediment transport, and the likelihood of breaching in numerical modeling studies (Kurum et al., 2012; de Vet, 2014; Passeri et al., 2018). LWR is indicative of vegetated land cover abundance (pixels with lower $NDWI$ have higher reflectance in the NIR band) which influences washover deposition thickness and geometry (Wang and Horwitz, 2007; Williams, 2015) and, in areas of low near-field LWR, washover penetrations will in general be greater given the on average lower elevation and vegetation density (Morton, 2002; Morton and Sallenger Jr., 2003). Given an overwash event, it is plausible that more shoreface and beach sediment is transported landward in front of stretches of low LWR and it is transported further inland. While this process occurs at the event scale, at the decadal time-scale, given the frequency of overwash events, the accumulated difference in landward transport would result in increased shoreline erosion rates seen as "hotspots" in Figure 2.12.

The interaction between cross-shore processes and backbarrier environment also affects the dune's vertical morphology as evidenced by the correlation between LWR and mean z_{dc}. The lower elevation dunes located near areas of low LWR would be overwashed more frequently and with greater energy due to preferentially channelized flow through the low topography and reduced bottom friction in the backshore/backbarrier (Morton, 2010; Houser, 2012, 2013). Consequently, these areas would undergo greater bed level change than adjacent higher elevation areas. This constitutes a positive feedback loop between overwash frequency and bed level lowering which could produce the pattern seen in Figure 2.13. A positive feedback between local

minima in z_{dc} and overwash frequency is used to explain the formation of overwash channels and breaches (Priestas and Fagherazzi, 2010; Houser, 2013). It is possible that, in a low-elevation dune system, backbarrier LWR exerts greater control on z_{dc} and, as a result, overwash frequency than vice versa. It is unlikely that deposition from overwash could influence the distribution of land and water observed at the scales seen in Figure 2.12. Rather, a suite of interrelated geological controls, which influenced the backbarrier topography and LWR distribution, determined the alongshore pattern of dune morphology (Cooper et al., 2018). The most important of these is presumably the inherited surficial/near-surface stratigraphy and the topography of the mainland barrier headland. The interior mainland's wetland surface is striated by shore-aligned coarser grained and lithified chénier ridges (see seaward-flaring ridges in Figures 2.1 and 2.12A) which formed within the last 710 to 300 years (Kulp et al., 2002). In addition to the chénier ridges, channel deposits associated with the Lafourche Delta's progradation led to differential shallow subsidence due to spatial variability in substrate compressibility (Byrnes et al., 2015; Jafari et al., 2018), which presumably affected marsh drowning and landloss in the CH's backbarrier. These controlled the "lagoonal" dimensions of the CH's backbarrier, i.e. areas of relatively low LWR where accommodation space is greater (Walters et al., 2014; Brenner et al., 2015; Lorenzo-Trueba and Mariotti, 2017), which influenced the alongshore distributions of chronic storm breaches and overwash-vulnerable dune crests giving rise to the relationship in Figure 2.13.

Once washover is deposited in the backbarrier, the area's LWR influences on average the quantity of sediment which settles out at a sub- or intertidal elevation. An area's LWR is a proxy for its hypsography, as a higher LWR entails a larger proportion of supratidal elevations and vice versa; and, all other factors being held constant, subaqueous deposition of washover sediment would inversely scale with LWR. Mainland barriers commonly increase in subaerial backshore volume during inundation- and overwash-regime storm impacts as sediment is transported from the shoreface landward for subaerial deposition (Durán et al., 2016). On the other hand, overwash of low-lying, sediment deficit barrier islands leads to subaqueous washover deposition and potential sediment loss from the system (Eisemann et al., 2018; Odezulu et al., 2018). This suggests that, for the CH, the increased net erosion rate and decreased mean dune height's relationship with alongshore variations in LWR can partially be explained by increased accommodation space for washover sediment landward of relatively lower LWR sections. Backbarrier accommodation space has been shown to increase the rate of barrier transgression (Walters et al., 2014; Brenner et al., 2015; Lorenzo-Trueba and Mariotti, 2017).

Due to numerous tidal creeks, navigational channels, and impounded water bodies, it is dif-

ficult to estimate tidally driven sediment transport pathways at the CH without a site-specific investigation as adjacent marshes can show significantly different sedimentation rates and tidal amplitudes (Kuhn et al., 1999). Determining whether proximal washover deposition would eventually be tidally flushed is outside the scope of this study. However, transport of washover from the backbarrier through breach channels appears to be an active sediment transport pathway during the channels' intermittent openings (based on post-storm aerial photography). The CH's central zone's backbarrier topography and fragmented wetlands can conceptually be compared to stage one in the runaway barrier transgression model of FitzGerald et al. (2006) (despite the system's microtidal regime). Stage one of their model entails marsh decline which, in turn, enlarges the tidal prism, consequently widening tidal inlets and increasing ebb/flood shoal sediment volume at the expense of the barrier. Storm breaches at the CH serve as temporary tidal inlets. These are historically ephemeral due to low tidal energy and are annealed by alongshore sediment transport. However, while open they apparently facilitate cross-shore sediment fluxes. This suggests barrier sediment export via cross-shore tidal fluxes through storm-induced breach channels may be sensitive to the health of backbarrier wetland ecosystems.

Washover sediment that is subaqueously deposited plausibly has an increased probability of resuspension and being flushed from the system, rather than being reworked by aeolian processes back into the dunes (Rosati and Stone, 2009; Eisemann et al., 2018). Coastline orientation relative to dominant wind direction is significant for determining the degree of aeolian sand transport into the foredune as well as development of the dune system (Miot da Silva and Hesp, 2010). GoM barriers are typically oriented normal to off-normal to northerly cold front winds. As a result, bay or backbarrier to shore aeolian transport of washover deposition is important for the post-storm recovery process of these systems (Harter et al., 2015). For the low-relief CH with an approximately linear coastline, the wind-shoreline angles are approximately alongshore uniform. Overland aeolian fetch for the dominant fall and winter wind direction (north and northwest) is reduced by low LWR as relatively more of the wind flow travels over water (Houser and Mathew, 2011). Variability in aeolian sediment transport potential in the backbarrier is therefore an additional factor explaining alongshore variability in dune height. These factors affect the rates of post-storm dune recovery within proximity to low LWR backbarrier environments through direct export of sediment (breach channels) and rendering it unavailable for aeolian transport. Overwash-susceptibility, aeolian transport potential, and breach-vulnerability plausibly links the interaction of the backbarrier environment with decadal shoreline morphodynamics through an alongshore variation in cross-shore processes.

2.5.3 Implications for Coastal Management

The CH were recently the site of the largest beach and dune restoration project in LA's history (completed in 2016). Historic morphodynamic trends provide knowledge of the CH's natural, pre-restoration behaviour (given its current geomorphic context) and can benchmark its state of vulnerability. Morphodynamic trends warrant consideration from this standpoint and that of the CH's restoration program's long-term resiliency. Identification of the CH's systematic vulnerabilities and insights into their causality will assist monitoring and maintaining the restoration project. Historical patterns in shoreline morphodynamics, long-term trends in subaerial sand storage, and estimated dune crest post-storm recovery rate provide valuable information for decision makers and further studies.

Erosion rates on the order of 20 m yr^{-1}, which occurs frequently in the central zone (see Figures 2.4 and 2.10), indicate a state of relatively high vulnerability. Storm impacts to the CH in this vulnerable state routinely generate erosion rate spike of 40–60 m yr^{-1}. Comparing the post-restoration behavior to this benchmark of vulnerability can provide the context for making sound inferences about the timing and necessity of maintenance renourishments. While the alongshore and cross-shore adjustment of the restoration's emplaced sediment is expected, morphodynamics which approach the pre-restoration behavior may plausibly be considered as an indication of vulnerability (Dean, 2002).

A significant finding related to the erosional "hotspots" is their spatial correlation with backbarrier marsh areas exhibiting a relatively low LWR. The connection between shoreline erosion and marsh deterioration (for which low LWR may be considered a proxy) prompt further consideration of marsh creation projects near the affected areas. A healthier, more solid backbarrier marsh, directly landward of the "hotspots", may enhance the trapping efficiency of washover sediment and server to buffer the restored CH from re-establishing the relatively high erosion rates observed pre-restoration. Coastal engineering design could decide to widen the marsh creation template in these areas. The optimum width could be estimated based on the results of numerical sediment transport modeling studies.

The BC zone's barrier will presumably continue to breach during storm-impacts. The erosion and export of re-nourished sediment associated with the breaching and re-establishment of a tidally connected embayment is presumably an expensive loss of sediment. To increase future restorations' cost-benefit ratio, it may be beneficial to extend the breakwater field an additional 1.5 km eastward. Numerical modeling studies are required to forecast the breakwater extension's

effect on the CH's vulnerable central shoreline and any ecological impacts. It has also been shown that the alongshore spit of the eastern zone is highly dynamic. Attempts to stabilize the shoreline would plausibly be an inefficient expenditure of resources. Further, due to the alongshore sediment transport patterns, this section will presumably continue to recover from future storm impacts at an accelerated rate compared to the central zone.

Information derived from the dune volume calculations can provide coastal management with reference values for use in long-term planning. Identification of the near constant trend in subaerial sand storage, encompassing oscillations generated by storm impact/response cycles, allows for an estimation of the natural, metastable equilibrium dune volume. It is plausible to assume that the post-restored CH's dunes will generally trend towards this volume given the system's geomorphic context. Volumetric calculations using data furnished by routine topographic monitoring of the subaerial sediment placement can be compared to this reference value. Given a project design life-time (i.e. the period of time during which the restoration is supposed to provide services such as limiting wave overtopping, maintain beach width, etc.), the trend in dune volume based on routine topographic monitoring will allow for a simple estimation of the project's performance. Sound inferences about when the project will require maintenance can be based on a estimate of when the post-restoration volumes will reach the pre-restoration state.

The spatial patterns of dune volume change can be used to further refine the restoration's monitoring program. An analysis of post-restoration dune volume trends can be estimated for the entire CH or target specific vulnerable stretches of the coastline. The behavior of select stretches of the CH can be monitored more frequently or with higher resolution. This would allow for a more nuanced decision-making process. For example, if a problem area (e.g. an erosional "hotspot") was losing dune volume at a greater rate than the adjacent areas (e.g. the western zone) and therefore approaching the pre-restoration state faster, coastal management would have a basis to consider a targeted maintenance of the problem area. On the other hand, if the trend in the problem area's dune volume indicates that it will not approach the pre-restoration state within the project's design life-time, then the targeted maintenance may be forestalled and incorporated into a more comprehensive strategy.

2.6 Conclusions

A time series of foredune and shoreline morphology data, derived from nine airborne lidar surveys, was analyzed to investigate storm-impact response/recovery coastal morphodynamics at the Caminada-Moreau Headlands, Louisiana, USA from 1998 to 2013. The main findings can

be summarized as follows:

1. The Caminada-Moreau Headlands' coastline can be divided into three zones characterized by different morphodynamics and dominant coastal processes. The western zone is influenced by coastal infrastructure, exhibits comparatively moderate shoreline erosion, and is relatively resilient to storm-impacts. The central zone is fully exposed to storm-impacts and regular wave action, exhibits characteristics of a sediment transport divergence node, and has the highest erosion rates. The entire central coastline displays overwash driven morphodynamics that are modulated by backbarrier wetland deterioration. Relatively high erosion rates found in the eastern zone alternate with periods of significant shoreline recovery. This zone is morphologically an aggradational spit sustained by eastward sediment transport from the central zone.

2. The study period (1998–2013) was notable for tropical cyclone activity. Shoreline erosion and foredune translation exceeding -20 m yr^{-1} were observed. Erosion generally resulted from episodic shoreline translation driven by tropical cyclone impacts with minor or negligible recovery. The central zone typified this behavior with a net landward shoreline translation of 222.3 m, while the western and eastern zones translated 54.5 m and 73.6 m, respectively. Storm-impacts push the central zone past a metastable equilibrium threshold resulting in negligible recovery following Hurricane Gustav's (2008) impact. The western zones' coastal protection prevents prolonged erosion/frequent overwashing following storm-impacts. The eastern zone conforms relatively well to the frequently overwashed barrier model with approximately complete dune recovery following devastating storm-impacts (Matias et al., 2009).

3. The alongshore spatial pattern of net erosion rates within the central zone was found to be inversely correlated with the land-to-water ratio of the adjacent backbarrier wetland. The mean dune crest elevation positively correlated with the backbarrier's land-to-water ratio. It is hypothesized that the fragmentation/deterioration of the wetlands into open water, represented by a low backbarrier land-to-water ratio, influences washover sediment transport and post-storm recovery. Possible mechanisms for this are reduced bottom friction during overwash events, increased backbarrier accommodation space, and reduced aeolian sediment transport potential during recovery periods.

4. Foredune translation slightly exceeded shoreline erosion while dune volume is approxi-

mately conserved through time. This partially supports the "rollover" model of coastal barrier transgression. However, the central and eastern dunes lost elevation at approximately -2 cm yr^{-1}. The central zone's morphology also appeared to transition from low-elevation foredunes to overwash terraces and sheets. This suggests that the central foredunes were pushed past a threshold for resilience given the area's rate of relative sea-level rise (3.49 mm yr^{-1}). It is conjectured that the central zone lacked the capacity to withstand the tropical cyclone impacts occurring between 1998 and 2013.

CHAPTER 3
EVENT-SCALE MORPHOLOGICAL MODELING OF LOW-LYING MAINLAND BARRIER SUBJECT TO HURRICANE FORCING:THE ROLE OF BACKBARRIER WETLANDS

3.1 Introduction

Sediment transport associated with tropical cyclones (TC) is an important morphodynamic driver for coastlines. For example, TC impacts have been estimated to account for up to 90% of Louisiana's (LA) shoreline change over decadal time scales (Stone et al., 1997). Morphological change resulting from sediment transport directly influences the barrier's resiliency to future storm impacts (Woodroffe, 2007). Additionally, the depositional environment (e.g., backshore, backbarrier lagoon, or offshore) imposes control on the amount of sediments available for recovery processes (Houser et al., 2008). Understanding the drivers and processes responsible for coastal geomorphic change is therefore central to estimating long-term sediment budgets—an important facet of resiliency in the context of sea-level rise and a changing climate (Miselis et al., 2016; Miselis and Lorenzo-Trueba, 2017)—and coastal restoration.

When a TC impacts the coast, the magnitude and direction of net sediment transport results from the combination of storm surge induced pressure gradients and surface wave orbital motion. The storm-driven flow is modulated by the biogeophysical and morphological state of the coastal barrier that further complicates sediment transport patterns. Variability in sediment transport and morphodynamics is therefore difficult to generalize across storm events and coastal settings due to inherent site-specific differences. Because of its distinct topographic and land cover characteristics, the Caminada-Moreau Headlands (CH), a rapidly-eroding deltaic headland of the Mississippi River Delta (MRD) complex (Williams et al., 1992; Kindinger et al., 2013), exhibits contrasting TC impact-driven sediment transport processes from many other coastal barriers. First, its low-lying topography makes the CH more susceptible to overwash and inundation. Second, there exists an extensive, fragmented backbarrier wetland without a characteristic lagoon (receiving basin for washover sediment). Overwash transport and storm surge-driven flow are influenced by this variability in land cover (e.g., wetland creek bottom or emergent estuarine vegetation) at length scales that range from 10^0 m to 10^3 m. In addition, the biophysical properties of vegetation and bed composition have been observed to influence post-storm washover deposition (Morton, 2002; Morton and Sallenger Jr., 2003; Wang and Horwitz, 2007). Third,

the CH is a sand-limited system (Kulk et al., 2005). The barrier morphostratigraphy exhibits a surficial veneer of sand overlying and transgressing the backbarrier marsh and paleo-deltaic sediments (Penland et al., 1988). The thickness of the sand layer becomes significant for sediment transport during TC impacts as erosion may completely remove this layer, exposing marsh outcrops or the mud barrier-core (Ritchie and Penland, 1988; Dingler and Reiss, 1995; Cooper, 2013). The CH was chosen as a study site based on these considerations, in addition to its economic importance as a barrier for Port Fourchon and its recent large-scale beach and dunes restoration.

A significant number of TCs have impacted the CH and influenced its morphology over the past two decades (Johnson et al., 2019). Hurricane Gustav (2008) was particularly chosen for this study as it produced the most severe morphodynamic response, i.e., alongshore-averaged shoreline and dune crest erosion of 48.5 m and 41.7 cm, respectively, and was accompanied by extensive data collection activities (Doran et al., 2009; Kennedy et al., 2010). This study investigates the CH's morphological responses to the evolution of impact regime forcing (Sallenger, 2000) during Hurricane Gustav and analyzes the overwash/inundation processes of a low-lying mainland barrier. In particular, the analyses herein relate the TC-driven sediment transport processes to the CH's site-specific characteristics. XBeach—a state-of-the-art, event-scale sediment transport/morphodynamic model—was chosen to hindcast Hurricane Gustav's impact as it has been extensively used to study TC impacts to barrier islands (Roelvink et al., 2009; McCall et al., 2010; Lindemer et al., 2010; Sherwood et al., 2014; Nederhoff et al., 2015; Smallegan et al., 2016; Harter and Figlus, 2017; Roelvink et al., 2017; Smallegan et al., 2017; Passeri et al., 2018; Schambach et al., 2018; van der Lugt et al., 2019). Utilizing an event-scale morphodynamic model allows for a quantitative inspection of overwash and inundation processes and the influence of topography/land cover on these processes at great detail in conditions where direct observation is often prohibitively difficult, if not impossible. The local-scale morphodynamic model's verification also provides the means to assess the land cover and topo-bathymetric inputs as variables influencing TC-driven sediment transport at the CH. This will allow future research to conduct numerical experiments of TC impacts to assess the feasibility of various barrier restoration design options and thus the CH's future resiliency.

To address the importance of nearshore sediment supply in the barrier "rollover" process and shoreline erosion during a storm event, a non-erodible layer is set up in the model and specified at the surficial sand layer's contact with the underlying barrier-core. This allows for a numerical experiment that specifically assess the significance of nearshore sediment availability

in overwash transport at the event time-scale (Miselis and McNinch, 2006). Analysis of overwash processes in distinct ecomorphological areas of the CH address how variability in morphology and backbarrier environment influence overwash. Specifically, whether a relatively more fragmented wetland surface (i.e., lower bed friction and hypsometry) promotes landward sediment transport during the overwash and inundation regimes compared to a relatively intact wetland surface (i.e., higher bed friction and subaerial land cover) is investigated.

The CH was recently the site of a major restoration effort including a $218 million beach and dune renourishment and a $56 million backbarrier marsh creation component (Louisiana Coastal Protection and Restoration Authority, 2017). Model calibration and validation completed herein lays the foundation for future work that focuses on forecasting future TC-driven geomorphic change to the CH. The future work will address the optimization of barrier system restoration design to retain sediment during storm impacts in relation to long-term coastal sustainability. Beach and dune restoration is critically important for the protection of Gulf of Mexico (GoM) coastlines and many other mid- and low-latitude coastal zones subjected to TC impacts. Future barrier design projects will benefit from an investigation into the role of low-lying topography, land cover, and sediment availability within such impacts.

In this section, a brief introduction with relevant literature is presented. The rest of the paper is structured as follows: Section 3.2 provides an overview of the CH and Section 3.3 describes the model setups, input generation, and post-processing methods; in Section 3.4, the computational results are presented and compared with hydrodynamic and morphodynamic observations associated with Hurricane Gustav; Section 3.5 discusses the sediment supply-limited numerical experiments, sediment transport and morphodynamics under overwash/inundation regimes in the context of low-lying barriers and backbarrier land cover/morphology's effect on deposition patterns; Section 3.6 summarizes the key findings.

3.2 Study Area

The CH is located in southeastern LA, USA, on the GoM's northern coast. It is a mainland barrier that forms a headland at the center of the (Late) LaFourche Delta littoral compartment. Its coastline is approximately 21 km long bounded by two artificially stabilized navigational inlets: Caminada Pass and Belle Pass, to the east and west, respectively (see Figure 3.1a). Alongshore drift-fed barrier islands (i.e., Grand Isle and the Timbalier Islands) flank the central headland and shelter the large, shallow coastal embayments Barataria Bay and Terrebonne Bay. Thirteen rubble mound breakwaters, a seawall, and an earthen dike protect the shoreline

directly seaward of Port Fourchon (Johnson et al., 2019). The CH's natural (pre-restoration circa 2013) coastal morphology consisted of alternating washover sheets and terraces, discontinuous foredunes and intermittently-open breach channels (Harper, 1977; Penland and Boyd, 1981; Ritchie and Penland, 1988). Pre-restoration foredune elevation was typically less than 1.5 m above mean sea-level (MSL). Median sand grain sizes grade finer from a range of 160 to 249 (mean = 200 ± 19) μm over the dunes and beach to 74–159 (mean = 100 ± 23) μm between 5.5 and 8 m water depth. For further details on the CH's long-term evolution, the reader is referred to Williams et al. (1992), Kindinger et al. (2013) and Byrnes et al. (2017).

With regard to the CH's unique geology, an overview of its geological formation is insightful. In LA's coastal geologic literature, the CH is conceptualized as phase one in the MRD complex's *delta cycle* (Penland et al., 1988). Phase one describes the morphostratigraphy of an abandoned delta lobe after marine transgressive processes, i.e., relative sea-level rise (RSLR), alongshore drift, and overwash, have considerably reworked the original depocenter. Complex vertical and lateral stratigraphic sequences arise due to meandering distributary channels and the concurrent alongshore drift-fed accumulation of beach ridges (Kulk et al., 2005). However, a thin wedge or veneer of mobile sand on top of paleo-deltaic strata and a contemporary marsh cap layer is used to conceptualize the upper shoreface and barrier (Harper, 1977; Penland and Boyd, 1981; Dingler and Reiss, 1995). This model describes the contact between the reworked, mobile modern sand and the underlying paleo-deltaic sediment and/or backbarrier marsh platform.

The sand layer's thickness tapers from 3–4 meters near the inlets to very little in the central area where marsh outcrops or the barrier-core may be exposed. Marsh outcrops and the barrier-core denote the appearance of the underlying marsh surface or muddy-clay layers, respectively, among the thin beach or washover sand lithosomes. During storm events, the sand layer's thickness affects local sediment transport as it influences sediment availability and can be entirely eroded, exposing a nearly non-erodible bed composition (e.g., marsh platform soils with root systems or over-consolidated clays) to erosional processes (Rosati and Stone, 2009). The exposure of marsh outcrops in eroding sediment-limited barrier sand bodies has been documented in the literature (e.g., Doughty et al. (2004); Harter et al. (2015); Matias et al. (2009); Cooper (2013); Sherman et al. (2013)). Cooper (2013) observed that the overstepped marsh platform is exposed for a period of time at the shoreline and is eroded at different rates by different processes than the migrating barrier sand body. The exposed barrier-core retreats during ambient conditions and is less affected by storm events as it is probably submerged (Cooper, 2013). Conceivably, an analogous process occurs during TC conditions.

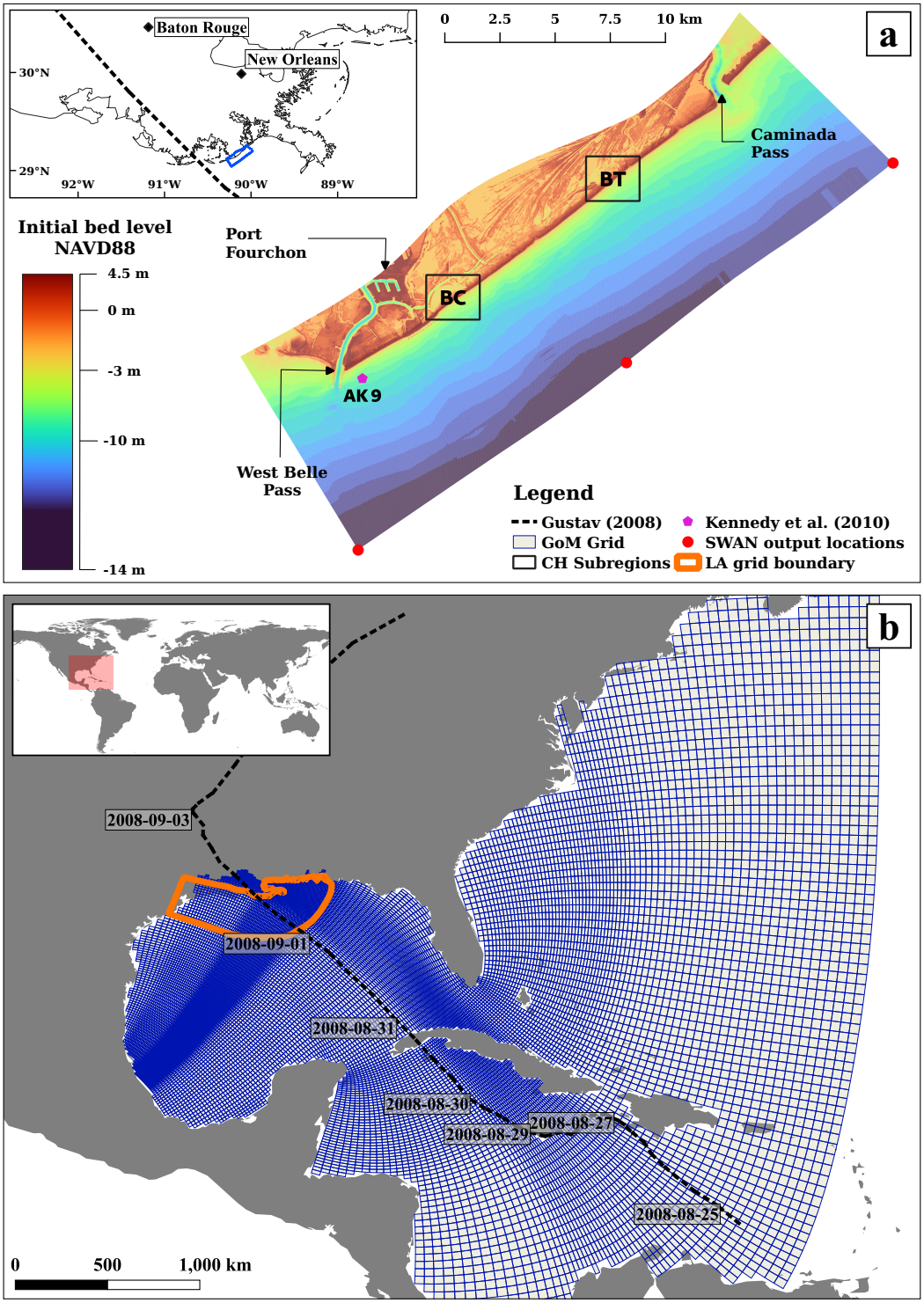

Figure 3.1: (a) CH model grid and initial bed level. The inset shows the CH domain relative to coastal LA and Gustav's track. Kennedy et al. (2010)'s wave gage 9 (AK9) is indicated and SWAN output locations are marked on the model's offshore boundary with red circles. Subregions Bayou Thunder (BT) and Bay Champagne (BC) are marked with black squares. (b) GoM grid (blue) and LA grid (orange polygon). Hurricane Gustav's track is presented with the timestamps and black dashed line.

3.3 Materials and Methods

3.3.1 Large-Scale Hydrodynamic Model

A two-dimensional, depth-averaged (2DH) fully-coupled SWAN/Delft3D-FLOW model (Lesser et al. (2004), SWAN version 4072ABCDE, Delft3D revision 64519) was used to simulate Hurricane Gustav's waves and water levels at the CH. Two nested grids were employed to allow finer grid resolutions near the coast while reducing the overall computation time. The GoM grid covered the western Atlantic basin, the GoM, and the Caribbean Sea (see Figure 3.1b). Water levels were pre-computed on the GoM grid and imposed as water level time-series along the open boundaries of the LA grid. The LA grid's areal coverage contains the northern GoM coast, extending approximately from Houston, Texas to Mobile, Alabama with an offshore boundary that roughly coincided with the continental shelf break (see orange polygon in Figure 3.1b). SWAN computed wave spectra on both grids simultaneously to generate boundary conditions for the nested grid, i.e., the LA grid. In the low-gradient GoM coastal zone, storm surge and surface waves are modulated by vegetation to attenuate storm surge and wave energy (Hu et al., 2015; Liu et al., 2018). Vegetation cover types were incorporated into the LA model based on a 2007 US Geological Survey (USGS) aerial survey (Sasser et al., 2008) and the physical properties of each type were assigned using the USDA herbaceous plant database and other literature. Further details on the large-scale hydrodynamic-wave model's setup and verification of the vegetation inputs can be found in Liu et al. (2018).

Different from Liu et al. (2018)'s model, the LA grid was refined over the CH's foreshore, coastline, and backbarrier wetland. The model's input topo-bathymetry in this location was updated to incorporate the high-quality topo-bathymetric data described in Section 3.3.2. Additionally, the meteorological forcing (i.e., wind velocity and atmospheric pressure) were generated by merging a tropical cyclone model (Holland et al., 2010), based on the National Hurricane Center's best track data for Hurricane Gustav and observed TC geometry to capture the high wind speeds of the storm's eye, with background wind velocities and pressure fields provided by the North American Regional Reanalysis (NARR) program. Finally, in contrast to applying a bulk drag coefficient to compute wind stress for the momentum balance, or one which increases monotonically with wind speed (Charnock, 1955), observational data in Powell et al. (2003) indicate that at high wind speeds the air-sea interface begins to saturate in terms of momentum transfer. Here, we apply the relationship of Vatvani et al. (2012) for the hydrodynamic simulations, where the drag coefficient first increases with wind speed and then decreases after

approximately 30 ms^{-1}.

3.3.2 Local Morphodynamic Model

A local XBeach model (XBeach-X release, revision 5526) of the CH (referred to as the CH model) was nested within the LA grid (see Figure 3.1a). The governing equations of XBeach have been covered extensively in previous studies (Roelvink et al., 2009, 2012, 2017). XBeach was executed in "surf-beat" (SB) mode which solves the non-linear shallow water equations at the wave group time scale (Roelvink et al., 2009). The momentum equation is tightly coupled with a wave action model to force low-frequency infragravity waves. Suspended sediment transport is modeled with a depth-averaged advection-diffusion equation of suspended sediment concentration; and the bed load sediment transport is calculated with the formula proposed in (Van Thiel de Vries, 2009). The resultant morphological changes are computed through the Exner equation and a dune avalanching algorithm. The CH model's computational grid, input data, and non-standard processes are described in the following subsections.

Grid and Initial Topo-Bathymetry

The CH model's computational grid is curvilinear with a refined resolution over the beach, dunes, and tidal inlets. The domain spans approximately 30 km in the alongshore direction and 13 km in the cross-shore for a total area of 390 km^2 (see Figure 3.1a). The landward boundary was fitted to LA Highway 1 and the seaward boundary extends to the limit of the high-quality bathymetric data (approximately -14 m NAVD88). Grid size in the cross-shore decreases smoothly from 40 m offshore to approximately 3 m at the duneline and increases again to 20 m at the landward boundary. Grid spacing in the alongshore dimension transitions smoothly from approximately 10 m over the tidal inlets (Belle Pass and Caminada Pass) to 20 m elsewhere. The given resolution was achieved with a total number of 1,008,750 grid cells.

The subaerial topography, as input, is generated by using a combination of a pre-storm LIDAR survey, terrestrial real-time kinematic global positioning system (RTK-GPS) survey, and the 2014 Coastal National Elevation Database (CoNED) digital terrain model (DTM) (Thatcher et al., 2016). The LIDAR survey was conducted by the USGS' Experimental Advanced Airborne Research LIDAR (EAARL) on March 3rd, 2008 and a nominal vertical/horizontal accuracy of 0.15/1.0 m was reported (Fredericks et al., 2017). The sandy beach, dunes, and backshore were covered by the quality-controlled USGS' LIDAR data (see online Supplement in Johnson et al. 2019) that had been filtered to exclude all points below mean high water (MHW). Over 34,000 RTK-GPS points of wetlands, marsh ponds, tidal creeks, and navigational channels were

incorporated to resolve the CH's backbarrier topography (CPRA, personal communication). The subaqueous domain was entirely covered with the 2006 LA Barrier Island Comprehensive Monitoring (BICM) Project's hydrographic survey (single-beam sonar) that reported a vertical accuracy of 0.18 m (Kindinger et al., 2013). The high-quality data (i.e., the LIDAR, single-beam sonar, and RTK-GPS data) were triangularly interpolated to the computational grid while grid points outside the high-quality data's coverage were sampled directly from the CoNED DTM and smoothly merged with adjacent elevations.

Boundary Conditions

Water levels from the LA grid were output every 30 minutes at the CH domain's corners and linearly interpolated across its boundaries. Two-dimensional wave spectra were extracted from the SWAN outputs at three locations along the CH model's offshore boundary (see Figure 3.1a) and used to generate spatially varying wave energy boundary conditions with a resolution of 30 minutes. Zero gradient flow and wave energy conditions were specified on the lateral boundaries. Absorbing-generating boundary conditions, which allow low-frequency oscillations in the water level to pass out of the domain, were used on the landward and seaward boundaries (van Dongeren and Svendsen, 1997).

Non-Erodible Layer Specification

Hard coastal infrastructure in the CH, i.e., Port Fourchon, the road network, breakwaters, seawall and jetties were treated as non-erodible for all simulations. Preliminary simulation results indicated that unlimited sediment availability in the active layer overestimated post-storm dune volume. In light of this, for a numerical experiment (Section 3.5.2) which examines the influence of sediment availability, a non-erodible layer (specified as the barrier-core) was generated for the CH domain to model limited foreshore sediment supply. The numerical experiment's sediment transport results are contrasted those of the base simulation, which contains an infinitely thick erodible layer outside the coastal infrastructure.

In the limited sediment supply case, sediment volume above MHW was considered as mobile dune/beach sand; whereas sediment below was treated as immobile clay/vegetated marsh surface, i.e., the barrier-core/marsh outcrops. Mean high water served as a proxy for the underlying marsh platform's elevation (Krone, 1985; Morris et al., 2002) and a value of 0.297 m NAVD88 was obtained from the nearby Grand Isle (GI) National Oceanic and Atmospheric Administration (NOAA) tidal station (CO-OPS id: 8761724). The mobile layer's thickness was calculated as $z^{t_0} - MHW$, where z^{t_0} is the initial bed level defined on the CH grid. Thus, the mobile layer's thickness varies spatially with the initial bed level, but the non-erodible layer's elevation

is uniform across the domain. Because the CH's primary sand storage is mostly contained in subaerial washover deposits overlying a transgressed marsh platform, we believe this simplification is reasonable. Perhaps in reality, the underlying layer is not completely immobile; however, due possibly to over-consolidation, inter-particle cohesion, and vegetated root networks, the critical shear stress for erosion is conceivably high. Although unresolved variability in the non-erodible layer, particularly near the berm and shoreline, will likely influence the sediment transport hindcast, a more detailed treatment is outside the scope of this work and is identified as an area for future research.

3.3.3 Land Cover Classification and Bed Friction Parameterization

Land cover, which is parameterized in terms of a calibrated bed roughness, is incorporated into the CH model to realistically simulate erosion/deposition as it influences sediment entrainment and transport. Such calibration, which includes the biophysical properties of vegetation through land cover classifications, has been shown to significantly improve morphodynamic model skill in overwash and inundation regimes (Kurum et al., 2012; de Vet et al., 2015; Nederhoff et al., 2015; Passeri et al., 2018; Schambach et al., 2018; van der Lugt et al., 2019). Land use/land cover (LULC) maps provided by NOAA's Coastal Change Atlas Program (C-CAP) or the National Land Cover Database (NLCD) are routinely utilized to incorporate LULC based surface roughness into hydrodynamic/sediment transport models (Dietrich et al., 2011; Mederios et al., 2012, 2015; Passeri et al., 2018; Schambach et al., 2018). However, C-CAP and NLCD maps were not suitable for hindcasting Gustav due to a two-year offset in their production from the event. A two-year offset in LULC classification is significant for the CH as historically its rate of erosion is 15 m yr^{-1} or greater (Williams et al., 1992; Kindinger et al., 2013). The LULC classifications over the shore and the backshore vegetation were therefore spatially inaccurate and could not properly model the CH's surface roughness distribution (see Figure 3.2).

To calibrate accurate roughness fields for the CH model, remotely-sensed imagery from Landsat 5 (Thematic Mapper) for the date of August 30th, 2008, two days prior to Gustav's landfall, was separately classified (see Figure 3.2). The Semi-Automatic Classification Plugin (SCP) (Congedo, 2016) for the Quantum Geographic Information System (QGIS) (QGIS Development Team, 2018) was used throughout the LULC classification process; both free and open-source software packages. Spectral bands 1, 2, 3, 4, 5, and 7 were used as data in the LULC classification. A principle component analysis was initially performed on the band set and the first three principle components were used to automatically define the training data regions. Training

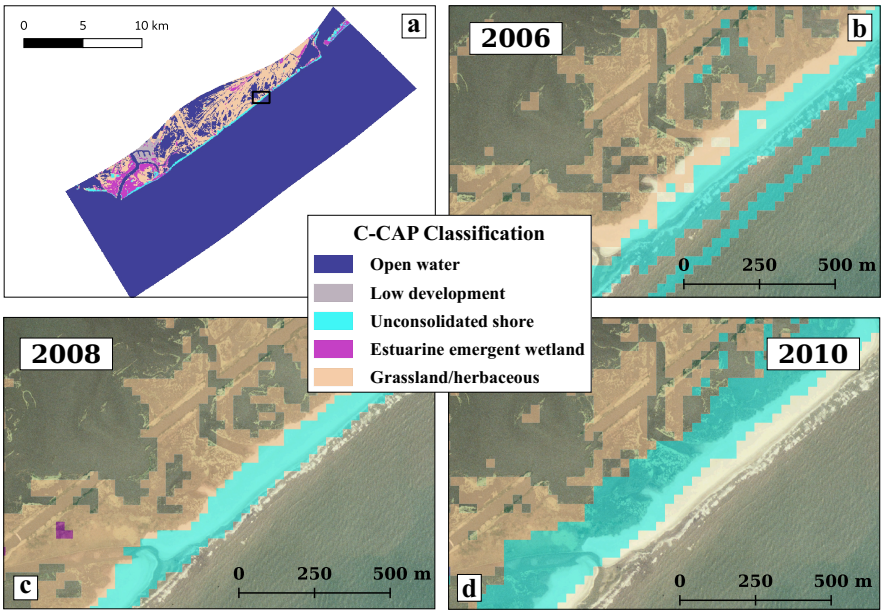

Figure 3.2: Shoreline mapping of LULC classifications. (a) the CH model's LULC classification with the detailed area in (b), (c), and (d) shown with a black polygon. (b) and (d) display the 2006 and 2010 C-CAP classifications, respectively. (c) the 2008 land cover classification performed in this study. Note that the open water LULC class is made transparent to reveal the imagery.

data regions for five LULC classes were assigned following the C-CAP scheme: open water, low development, unconsolidated shore, estuarine emergent wetland, and grassland/herbaceous. The minimum distance method was used for pixel classification.

The LULC classification was incorporated into the CH model through bed friction coefficients that depend on the Manning's n coefficient. Manning's n values were mapped to LULC classes following the Mattocks and Forbes (2008)'s calibration which has been successfully used in XBeach (van der Lugt et al., 2019). The Manning's n field was sampled at the CH model's grid points and smoothed to avoid abrupt transitions in roughness.

Dynamic bed roughness was utilized to incorporate the damping of roughness due to the local vegetation's burial or removal by deposition or erosion, respectively (van der Lugt et al., 2019). The root length was set to 0.3 m (d_{root}) and 0.5 m was used for the stem length (d_{stem}). The variable roughness field realistically captures cross-shore bed friction gradients and reduces unrealistic landward sediment transport rates during the inundation and overwash regimes. In addition, it also reduces bed friction when backbarrier vegetation is buried by washover deposition or removed by erosion.

Table 3.1: Land cover class definition correspondence with C-CAP classification scheme and their associated Manning's n values for bed roughness.

Classification	C-CAP class name	Manning's n
Water	Open Water	0.020
Sand	Unconsolidated Shore	0.020
Backbarrier vegetation	Grassland/Herbaceous	0.034
Wetland vegetation	Estuarine Emergent Wetland	0.045
Anthropogenic	Low Development	0.050

3.3.4 Model Performance Metrics

The computed geomorphic changes were assessed by comparing simulated post-storm bed level elevations to a post-Hurricane Gustav LIDAR survey. The post-storm LIDAR survey was conducted by the USGS' EAARL on September 9$^{\text{th}}$, 2008 (Fredericks et al., 2017). Tight temporal constraint on the input and verification data with regard to the event is important for model verification (Lindemer et al., 2010); in this case, the pre- and post-storm LIDAR were collected 5 months prior to and just 5 days after Hurricane Gustav's impact, respectively. The post-storm LIDAR survey data were averaged within the CH grid cells to yield comparable values. Observations below MHW were removed because turbid coastal water may reflect the LIDAR beam incorrectly measuring bathymetry. The computed morphology was also visually compared to post-storm aerial imagery acquired 4 weeks after Hurricane Gustav (October 1$^{\text{st}}$, 2008) that also contained the impact of Hurricane Ike which made landfall September 13$^{\text{th}}$, 2008 in Galveston, Texas.

Standard statistical quantities were used to assess model accuracy and its predictive capability. The bias or mean error ($\overline{e}$) describes the overall tendency to over-estimate erosion ($\overline{e} < 0$) or accretion ($\overline{e} > 0$) and is calculated as

$$\overline{e} = \frac{1}{N} \sum_{i=1}^{N} \left(z^i_{post,MODEL} - z^i_{post,LIDAR} \right), \tag{3.1}$$

where N is the number of grid cells containing observations, $z^i_{post,MODEL}$ is the i^{th} grid cell's computed post-storm bed level elevation, $z^i_{post,LIDAR}$ is the LIDAR-derived post-storm elevation. The root-mean-square-error (e_{rms}) was computed as

$$e_{rms} = \sqrt{\frac{1}{N} \sum_{i=1}^{N} \left(z^i_{post,MODEL} - z^i_{post,LIDAR} \right)^2}. \tag{3.2}$$

Model skill (s), which serves to benchmark predictive capability, was computed as

$$s = 1 - \frac{\sum_{i=1}^{N} \left(\Delta z^i_{LIDAR} - \Delta z^i_{MODEL}\right)^2}{\sum_{i=1}^{N} \left(\Delta z^i_{LIDAR}\right)^2}, \tag{3.3}$$

where Δz^i_{LIDAR} is the observed bed level change in the i^{th} grid cell and Δz^i_{MODEL} is the modeled change in the same cell (Gallagher et al., 1998). A perfect simulation is indicated by $s = 1$, whereas $s = 0$ indicates that the results are no better than predicting no bed level change. If $s < 0$, then zero bed level change is a better prediction than the model's results.

Finally, the scatter index (SI) is used to provide an overall measure of the difference between the predicted and estimated bed elevation in the domain and is given as

$$SI = \frac{\sqrt{\frac{1}{N}\sum_{i=1}^{N} \left(z^i_{post,LIDAR} - z^i_{post,MODEL}\right)^2}}{\frac{1}{N}\sum_{i=1}^{N} z^i_{post,LIDAR}}. \tag{3.4}$$

3.4 Results

3.4.1 Hydrodynamics

Waves and water levels generated by Hurricane Gustav were verified for the LA domain using observation data collected from the GI NOAA tidal station, LA's Coastwide Reference Monitoring System's (CRMS) water level loggers (CRMS0292 and CRMS1064), and wave gages 8, 9, and 11 from Kennedy et al. (2010). Figure 3.3 compares observed versus computed mean water levels (panels b—g) along with observed versus computed wave parameters (panels h—j) and the biases and root-mean-square errors are tabulated in Table 3.2. The hydrodynamic model reproduces the water level observations with e_{rms} values in the range of [0.16 m, 0.31 m]. The CRMS0292 and CRMS1064 stations (b and c in Figure 3.3, respectively) are located within the intertidal marsh and indicate that overland flow is accurately modeled; however, the model slightly underestimates the storm surge's peak magnitude. The GI station (Figure 3.3d) is sheltered within a harbor which offers an explanation to the phase and magnitude differences. Wave gauges AK8, AK9, and AK11 (e—g in Figure 3.3) slightly overestimate the peak water level with biases of -0.02 m, 0.09 m, and 0.12 m, respectively. The consistent offset in water level prior to the Gustav's impact in AK9 and AK11 is plausibly explained by the settlement of the instrument on LA's muddy sea floor. Significant wave height at AK9 and AK11 (i and j in Figure 3.3) are reproduced with e_{rms} values of 0.34 m and 0.14 m, respectively, with the

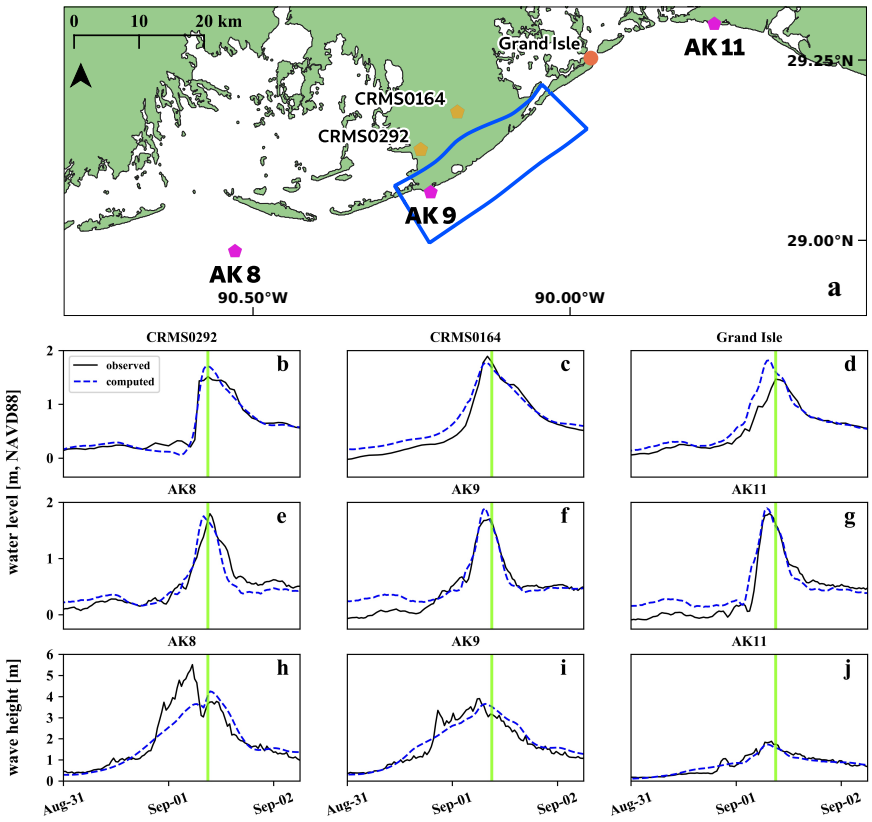

Figure 3.3: (a) Location of observation stations within the LA domain in relation to the local XBeach domain (blue polygon). (b—j) Comparisons between calculated hydrodynamics and observations with observations in black, computed values in dashed blue, and Gustav's approximate landfall time at Cocodrie, LA indicated as a vertical green line. From left to right water level comparisons at CRMS station 0292 (b) and 0164 (c), NOAA's GI tidal station (d), and Kennedy et al. (2010)'s wave gages 8 (e), 9 (f), and 11 (g). Significant wave height comparisons at Kennedy et al. (2010)'s gages 8 (h), 9 (i), and 11 (j).

modeled peak leading the observations by approximately 1 hour at AK9. The difference between the modeled and observed significant wave heights at AK8 (e_{rms} = 0.61 m) is likely due to inaccurately modeled wind fields near Hurricane Gustav's track, which passed approximately over AK8's location.

Figure 3.4 shows the boundary conditions used to force the CH (XBeach) model, as well as, its internal hydrodynamic and wave computations. The water level boundary condition hydrographs (3.4a) indicate a small east-to-west gradient which becomes seaward directed past the storm's peak. The computed water level at AK9 (Figure 3.4) reproduces the measurements with a bias and root-mean-square-error of 0.05 m and 0.22 m, respectively. Figure 3.4c and Figure 3.4e indicate small variability in wave climate along the offshore boundary. A decent match between the computed and observed significant wave heights at AK9 in Figure 3.4 is

Table 3.2: Statistical performance metrics for the LA domain's flow and wave models.

		Water level					Significant wave height		
	CRMS0292	CRMS1064	GI	AK8	AK9	AK11	AK8	AK9	AK11
e [m]	0.16	0.27	0.26	-0.02	0.09	0.12	-0.13	0.07	-0.01
e_{rms} [m]	0.19	0.30	0.31	0.16	0.21	0.25	0.61	0.34	0.14

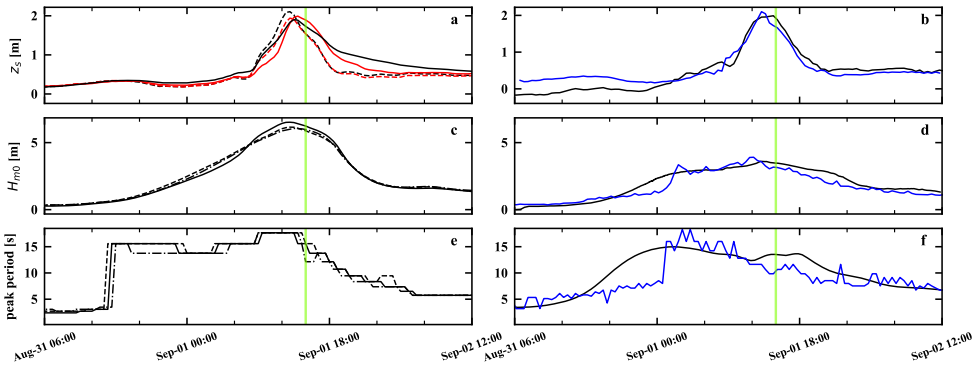

Figure 3.4: (a) Water levels imposed on the CH domain. The dashed lines indicate offshore and the solid show the landward boundaries. The eastern and western locations are shown in black and red, respectively. (b) Water level comparison between the CH model results (black) and observations at AK9. (c) Wave height from the CH model's wave energy boundary conditions; solid is eastern, dashed is central, and dash-dot is the western location, respectively. (d) Wave height comparison between computed results (black) and observations at AK9 (blue). (e) Peak period computed from wave energy boundary conditions with same notation as (c). (f) Comparison between CH model's computed peak period results (black) and observations at AK9 (blue). Hurricane Gustav's landfall is indicated by a green vertical line.

achieved with a bias and root-mean-square-error of 0.17 m and 0.41 m, respectively, with a some overestimation before and after the peak. The comparison of peak periods is satisfactory (e = 0.99 s and e_{rms} = 2.69 s), but the computed wave periods slightly lead the observations in time. For wave calculations, the breaker index, $\gamma = \frac{H_{rms}}{d}$ where H_{rms} is the root-mean-square-error wave height and d is the local depth, in the wave breaking dissipation term was adjusted from its default value of 0.55 to 0.4 which is within a reasonable range (Hoonhout, 2015).

3.4.2 Morphodynamics

Domain-Wide Verification

The computed results for the entire CH domain were compared with the LIDAR observations in terms of post-storm subaerial volume (V_{sa}), dune crest elevation (z_{dc}), and bed level change (Δz). Subaerial volume calculations were limited to grid cells with elevations above MHW which were contiguous with the main barrier sand body. The net change in subaerial volume (ΔV_{sa}) was calculated at cross-shore grid lines between the CH's input and output topography. Figure 3.5a

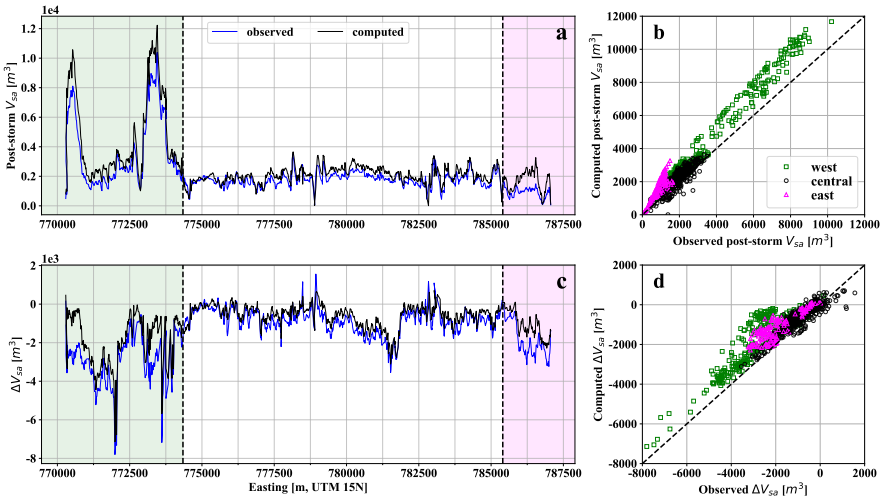

Figure 3.5: (a) Alongshore distribution of computed (black line) and observed (blue line) post-storm dune volume. The green area is influenced by hard structures (seawall, breakwaters, and jetty) and the magenta area is influenced by an alongshore spit and inlet system. (b) Correlation between observed and computed post-storm volume where the western, central, and eastern most regions denoted in (a) are represented with green squares, black circles, and magenta triangles, respectively. (c) Alongshore distribution of computed and observed volumetric change. (d) Correlation between computed and observed volume change.

and c show the alongshore distribution of post-storm V_{sa} and its net change, respectively. The central CH, approximately between 774000 and 785500 easting (referenced to Universal Transverse Mercator Zone 15 North throughout) matches the trend in observed post-storm V_{sa} well but shows a systematic overestimation of net accretion between 779000 and 782500 easting and a variable response elsewhere. The CH's western shoreline (west of 774000 easting and highlighted in green) is protected with rubble mound breakwaters, a seawall, and an earthen dike. The computed results here underestimate erosion which may be due to unresolved interactions between the hydrodynamic-wave model and the structural defenses. The eastern end (shown in magenta and approximately east of 785500 easting) is an attached alongshore spit and tidal inlet system. The computed results here show that erosion is relatively underestimated. Computed versus observed post-storm V_{sa} and the net change in V_{sa} are plotted in Figure 3.5b and c, respectively, and the statistical metrics are provided in Table 3.3.

Post-storm z_{dc}, defined as the maximum post-storm bed level elevation along a grid line, is shown in Figure 3.6a. Post-storm z_{dc} does not exhibit the same trends as V_{sa}. The computed post-storm z_{dc} is not systematically biased in the central CH domain, but begins to show a small discrepancy and a larger positive bias near the structural defenses and inlet system. This is also evident in the computed versus observed post-storm z_{dc} and its net change presented in Figures 3.6b and d, respectively. Overall, the computed morphology in the central section of the

Table 3.3: Statistical assessment of the computed V_{sa} and z_{dc} and their net changes for the entire CH domain. The results are assessed in terms of model bias ($\overline{e}$), root-mean-square-error (e_{rms}), and scatter index (SI) using the LIDAR observations as reference values.

	V_{sa}			ΔV_{sa}	z_{dc}			Δz_{dc}
Section	$\overline{e}$ [m^3] (%)	e_{rms} [m^3]	SI [·]	SI [·]	$\overline{e}$ [m] (%)	e_{rms} [m]	SI [·]	SI [·]
East	767.4 (84.7)	880.8	0.49	0.22	0.53 (67.0)	0.57	0.25	0.28
Central	282.8 (16.8)	387.4	0.15	0.29	0.13 (19.1)	0.40	0.38	0.67
West	978.3 (29.7)	1160.0	0.17	0.22	0.35 (22.3)	0.50	0.20	0.62
Overall	509.4 (27.8)	717.8	0.23	0.33	0.23 (25.5)	0.47	0.33	0.68

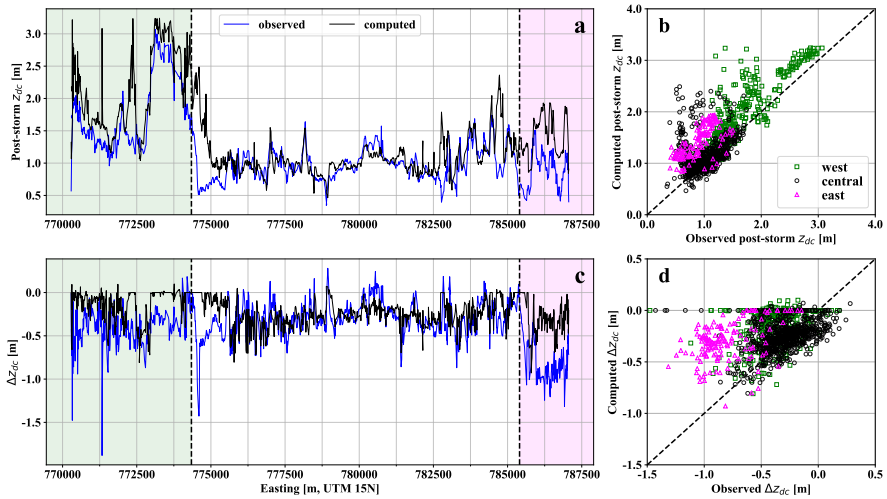

Figure 3.6: (a) Alongshore distribution of computed (black line) and observed (blue line) post-storm dune crest elevation. The green area is influenced by hard structures (seawall, breakwaters, and jetty) and the magenta area is influenced by an alongshore spit and inlet system. (b) Correlation between computed and observed z_{dc} where the western, central, and eastern most regions denoted in (a) are represented with green squares, black circles, and magenta triangles, respectively. (c) Alongshore distribution of computed and observed net z_{dc} change. (d) Correlation between computed and observed net change in z_{dc}.

CH is less biased than those of the other sections and that of the CH domain as a whole (see Table 3.3).

Bed level change at each grid cell containing LIDAR data (number of grid cells = 30,604 covering 3.1 km^2) was calculated for the central CH and is compared to the observations in Figure 3.7. Positive and negative biases are delineated by a one-to-one line. Points falling above the line indicate overestimated accretion and those falling below an overestimation of erosion. The II and IV quadrants in Figure 3.7 indicate qualitative error where the model predicted accretion but erosion was observed and vice versa, respectively. The majority of the computed bed level changes fall near the 1:1 line, but show a bias towards accretion. Relatively more scatter occurs where observed net erosion is high ($\Delta z > 1$m) or close to zero. In summary, the model results show that the morphodynamics associated with Hurricane Gustav's impact

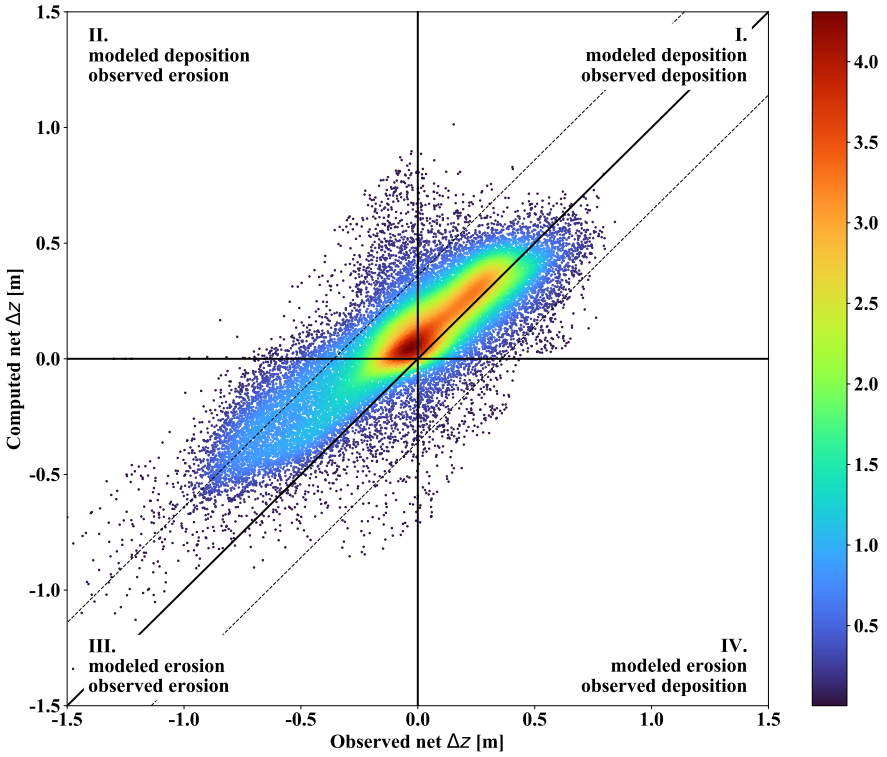

Figure 3.7: Computed versus observed net Δz for the central portion of the CH. The solid line indicates a perfect match between the model results and the observations and the dashed lines are offset by one standard deviation in the observations. The colorbar indicates the density of the plotted data points.

are captured reasonably well ($s = 0.30$), as is the bed level ($e_{rms} = 0.47$ m), but there is an overestimation of post-storm accretion in the subaerial beach and backshore ($\overline{e} = 0.23$ m).

Subregion comparisons

Alongshore variability in pre-storm dune morphology, sediment availability and surface roughness at the CH present different environments for modeling sediment transport and morphodynamics. To identify the significant sediment transport processes and where they are dominant in the CH, two subregions were selected. Our selection is based on the distinct characteristics of the subregions, namely nearshore sediment availability and backbarrier surface roughness/topography. Figure 3.1a shows the subregions in relation to the CH domain: Bayou Thunder (BT) to the east and Bay Champagne (BC) to the west.

Figure 3.8 shows planview comparisons for the BT subregion. The pre- and post-storm imagery (Figures 3.8a and b, respectively) show that depressions between the beach ridge sets, which acutely intersect the shoreline from the north-northeast, serve as sediment transport pathways. Storm-driven landward transport and dune lowering is also observed and reproduced in the computed sediment transport results (see Figure 3.8c and d for the model's initial and final

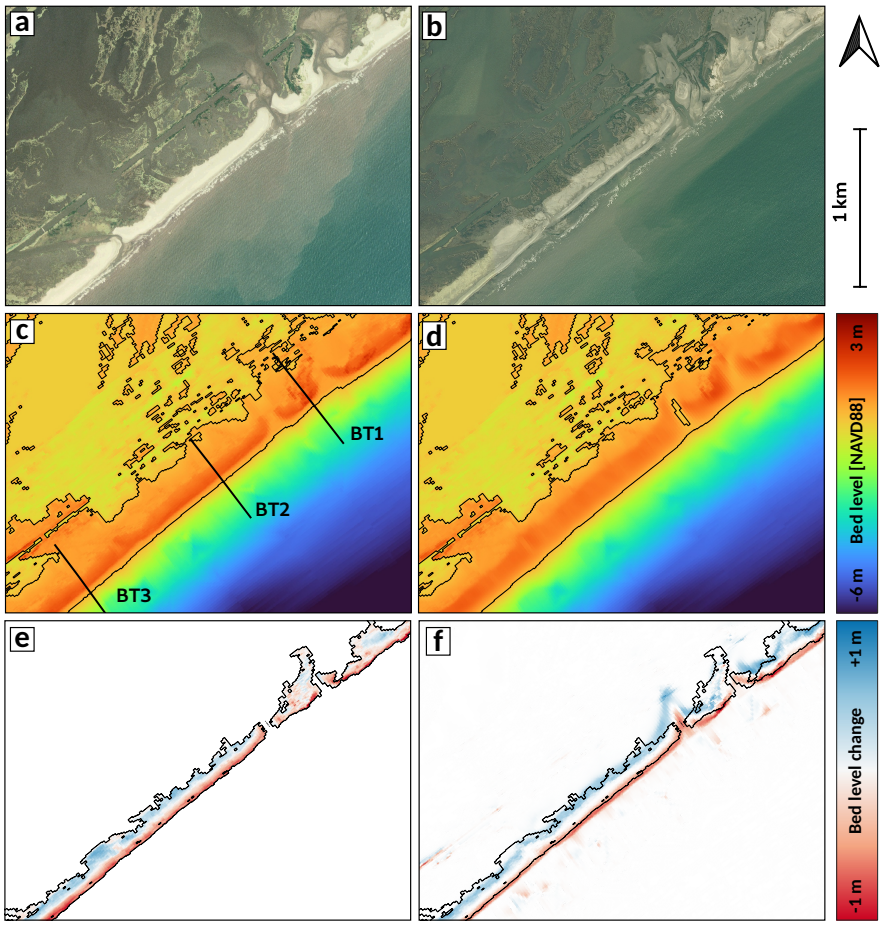

Figure 3.8: Bed level dynamics at the BT subregion. (a) Pre-storm aerial imagery (2007/9/20); (b) Post-storm aerial imagery (2008/10/1); (c) Pre-storm input topo-bathymetry with the zero-level contour shown in black and cross-shore transect locations; (d) Post-storm output bed level with the zero-level contour; (e) Observed bed level change with the observations' extent outlined in black; (f) Computed bed level change also with the observations' extent shown in black.

bed level, respectively). Figure 3.8e only shows the observed bed level change above MHW and thus does not capture the inter- and subtidal washover deposition observed in Figure 3.8b. However, the computed bed level change in Figure 3.8f contains the subaqueous deposition of washover sediment and the initial infilling of a navigational channel (also present in Figure 3.8b). In other words, the computed bed level change generally reproduces the observed barrier rollover pattern of foreshore to backbarrier transport, but slightly overestimates landward transport and post-storm accretion. Computed and observed post-storm bed levels at the transects (BT1, BT2, BT3) in Figure 3.8c are shown in Figure 3.9. The cross-shore morphodynamics are captured well in the computed results, but landward transport and dune crest lowering are slightly overestimated at BT1.

Figure 3.10 shows planview comparison of computed versus observed bed level dynamics

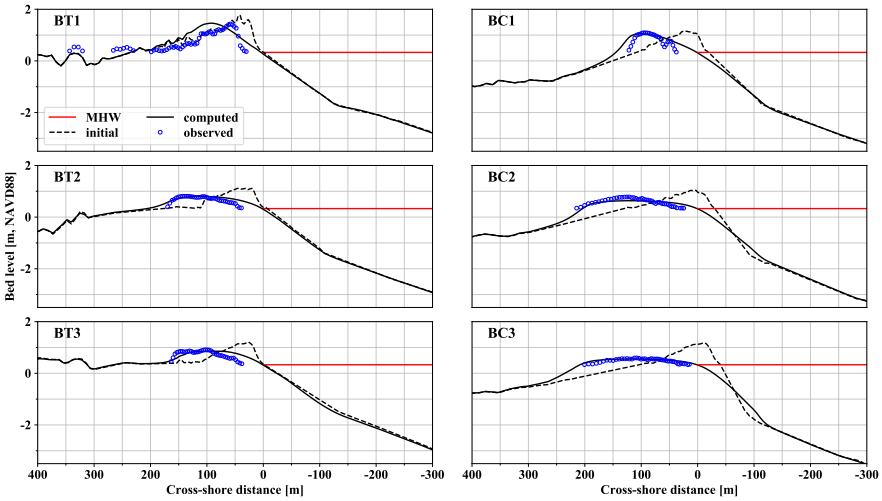

Figure 3.9: Pre- and post-storm computed bed level profiles (dash and solid black lines, respectively) in comparison with LIDAR observations (blue circles) for the BT subregion (panels BT1—BT3) and the BC subregion (panels BC1—BC3).

at the BC subregion which is centered on an attached spit enclosing Bay Champagne, an interior marsh lake which historical erosion exposed to the ocean. Post-storm aerial imagery (Figure 3.10b) exhibits breaches in the attached spit and approximately uniform landward transport and flattening of the barrier's central section. The computed morphological change matches this pattern (see the CH model's input and output bed levels in Figures 3.10c and d, respectively). Figure 3.10e contains the observed bed level change where both pre- and post-Gustav LIDAR data exist. In general, the pattern of foreshore erosion and landward transport into the bay is reproduced in the computations (Figure 3.10f). The aerial imagery in Figure 3.10b also contains Hurricane Ike's impact, which occurred approximately two weeks after Hurricane Gustav, and presumably exhibits additional storm-driven sediment transport. The eastern breach in Figure 3.10b does not appear in the post-storm LIDAR (captured prior to Hurricane Ike's impact), but the western breach is present in both (see Figure 3.10e). The computed bed level change in Figure 3.10f shows the initiation of a scour channel at the observed breach's approximate location, but its formation and scour depth are limited compared with the observations. Comparisons of observed versus computed post-storm bed level along the transects (BC1, BC2, BC3) in Figure 3.10c are shown in Figure 3.9. The computed cross-shore post-storm profiles are similar to the observed post-storm morphology and accurately capture the storm-driven elevation change.

The CH model's performance statistics are presented in Table 3.4. The computed morphodynamics are in general similar or slightly better than recent field-scale XBeach modeling studies

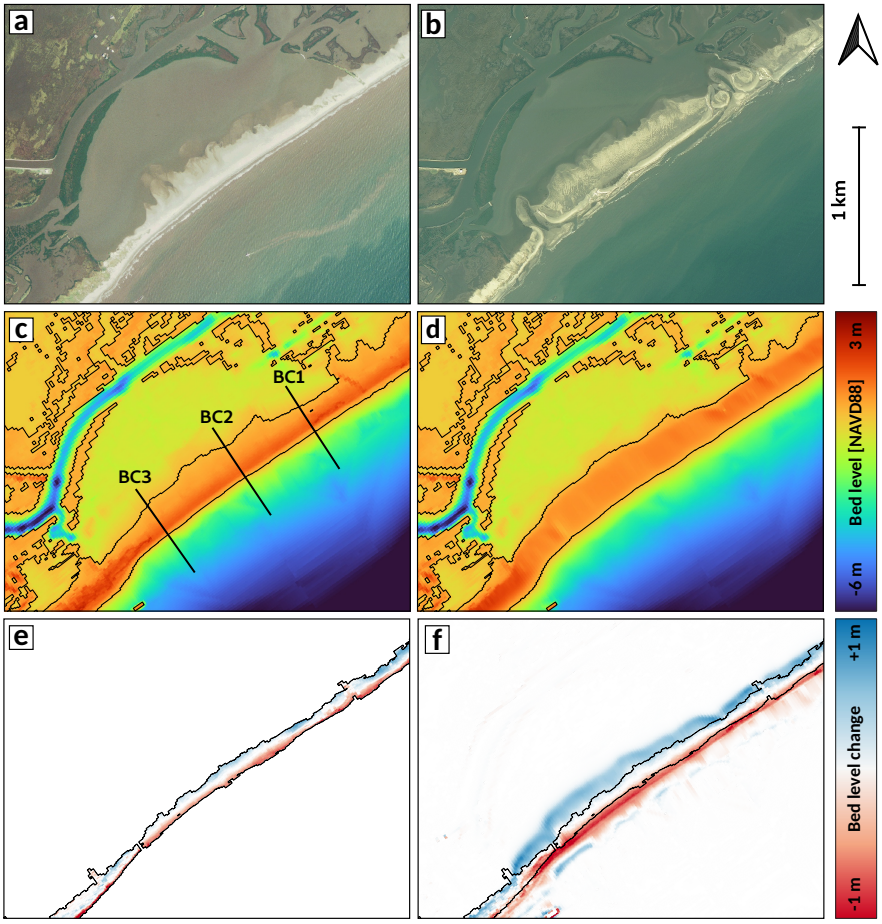

Figure 3.10: Bed level dynamics at the BC subregion. (a) Pre-storm aerial imagery (2008/9/20); (b) post-storm aerial imagery (2008/10/1); (c) pre-storm input topo-bathymetry with the zero-level contour shown in black and the transect samples; (d) post-storm output bed level with the zero-level contour; (e) Observed bed level change with observations' extent outlined in black; (f) Computed bed level change with the observations' extent outline in black.

Table 3.4: Statistics of computed bed level changes at subregions BT, BC, and the overall CH grid. The skill is calculated based on bed level change, while the other metrics are based on computed versus observed post-storm bed level.

Region	Skill [·]	Bias [m]	RMSE [m]	SI [·]
BT	0.53	0.14	0.24	0.24
BC	0.82	0.03	0.15	0.15
All	0.30	0.18	0.32	0.32

reported in the literature (Passeri et al., 2018; Schambach et al., 2018; van der Lugt et al., 2019). Within the BT subregion, the model performs well, but the comparison between the modeled and observed bed level has more scatter with a discernible bias compared to BC. However, it must be noted that BT is located in a part of the CH with greater variability in bed composition and backbarrier surface roughness/topography which offers an explanation for the observed scatter in the model-observation comparison.

3.4.3 Storm-Driven Barrier Evolution

The CH's low-lying topography is more susceptible to overwash and inundation by TC-driven storm surges and waves compared to other barriers with more developed and higher elevation backshore/foredune systems. The barrier sand body is also relatively narrow, thus it is tightly coupled to the backbarrier environment, and fragmented at short length scales. These characteristics are expected to produce impact regime morphological responses that may be typical of low-lying barriers and differ from others. In addition, variation in geomorphology and biophysical properties within the CH's domain (e.g.,, BT and BC areas) can introduce variability into sediment transport processes. Figures 3.11 and 3.12 show the time-stacks of cross-shore profile evolution at BT3 and BC3, respectively, to illustrate these differences.

The profiles display a similar initial sequence and duration of impact regimes (panels b and c in Figures 3.11 and 3.12 at BT3 and BC3, respectively) at the onset of Hurricane Gustav. Following Sallenger (2000), impact regimes are defined as: (i) *swash* that occurs when maximum water level for a given interval (1 hr) does not exceed MHW; (ii) *collision* that occurs when maximum water level exceeds MHW but is less than z_{dc}; (iii) *overwash* that occurs when the maximum water level exceeds z_{dc} but the minimum water level does not; and (iv) *inundation* that takes place when the minimum water level exceeds z_{dc}.

Both profiles experience an initial swash regime which is relatively insignificant. Next, collision regime forcing occurs (lasting approximately 20 hrs), followed by a relatively brief period

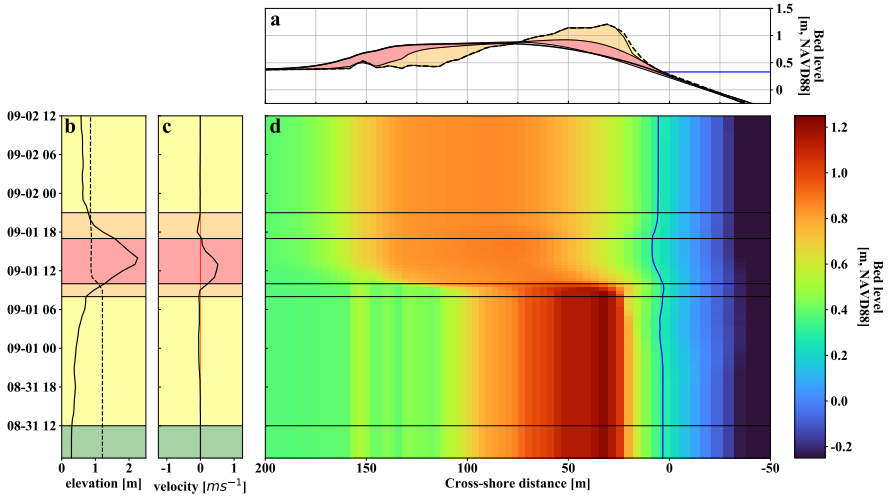

Figure 3.11: Cross-shore bed level evolution at BT3. (a) Cross-shore profiles and MHW (blue line). The dashed and solid black lines are the initial and final bed levels, respectively. The yellow, orange, and red areas indicate profile change over the first collision, overwash, and inundation regimes, respectively. (b) Time-series of water level (solid) and z_{dc} elevations (dashed). (c) Time-series of cross-shore current velocity at the shoreline in (a). The green, yellow, orange, and red shaded areas in (b) and (c) indicate the swash, collision, overwash, and inundation regimes, respectively. (d) Time-stack of bed levels showing the profile's evolution with the MHW contour (blue line) for reference.

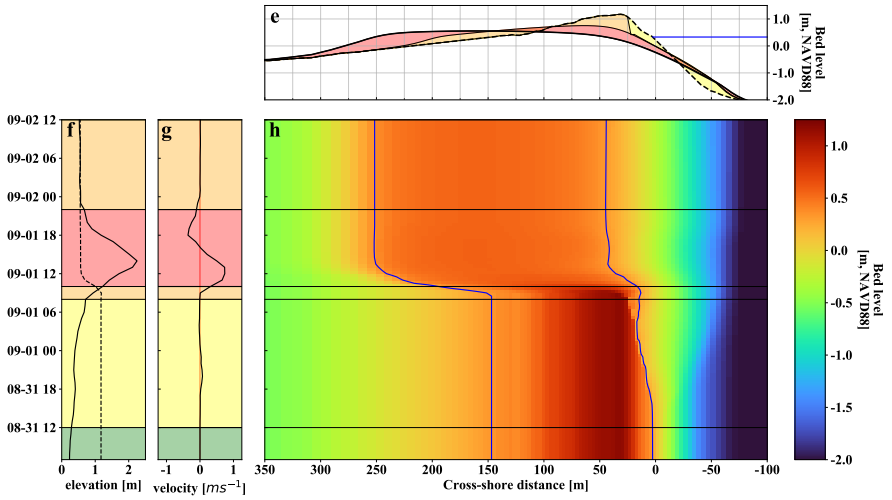

Figure 3.12: Cross-shore bed level evolution at BC3. (a) Cross-shore profiles and MHW (blue line). The dashed and solid black lines are the initial and final bed levels, respectively. The yellow, orange, and red areas indicate profile change over the first collision, overwash, and inundation regimes, respectively. (b) Time-series of water level (solid) and z_{dc} elevations (dashed). (c) Time-series of cross-shore current velocity at the shoreline in (a). The green, yellow, orange, and red shaded areas in (b) and (c) indicate the swash, collision, overwash, and inundation regimes, respectively. (d) Time-stack of bed levels showing the profile's evolution with the MHW contour (blue line) for reference.

of overwash (2 hrs at each profile), which rapidly transitions into a relatively longer period of inundation forcing. The inundation regime lasted approximately 5 more hours at BC3 than that at BT3 (a 71% percent change in duration). After the storm's peak, the sequence approximately repeats itself in the reverse order at BT3, while the BC3 profile does not return to the collision regime but instead persists within the overwash regime as the storm passes.

During the collision regime (yellow areas in panels a, b, and c in Figures 3.11 and 3.12) sediment transport differs markedly between the profiles. There is little change at BT3 and, in contrast, there is substantial foredune scarping and offshore transport at BC3. The most significant elevation change occurs at both profiles over a short duration within the overwash regime (see orange area in Figures 3.11a and 3.12a and bed level change between approximately 9/1 08:00 and 10:00 in panel d). Responses to overwash regime forcing at BT3 and BC3 share the characteristics of relatively large and rapid landward sediment transport. At BT3, however, overwash sediment transport forms a thicker subaerial deposit than that at the BC3 profile, with less landward extent. Overwash sediment transport at BC3 terminates approximately 85 m further landward (into the bay) and is deposited at a lower elevation. At both profiles, depositional patterns during the inundation regime largely conform to that deposited during the initial overwash regime, except that washover length and volume is noticeably larger at BC3 compared to BT3. At BT3, transported sediment is deposited above MHW (i.e., subaerially) and forms a thicker washover fan with less landward excursion.

During the inundation regime (red areas in panels a and b in Figures 3.11 and 3.12), the cross-shore current direction shows a marked reversal at BC3, but is less pronounced at BT3. The inundation regime at BT3 results primarily in further landward transport of the pre-storm dune sediment. This is also the case at BC3 despite the presence of a flow reversal. The second overwash regime interval at BC3 does not appear to influence the profile's bed level which remains approximately stable after the cross-shore velocity peaks. However, at BT3 there is minor seaward transport during this period which corresponds to a small seaward directed flow reversal (see MHW contour in Figure 3.11d). This is followed by stability during the second collision regime.

A significant difference between the two profiles can be identified in their post-storm morphology. The post-storm z_{dc} at BC3 is 0.55 m NAVD88 while at BT3 it is 0.84 m NAVD88. The impact to BC3's foredune forces greater lowering despite its approximate similarity to BT3 in terms of initial z_{dc} elevation. The difference in impact is due to differences in z_{dc} evolution and the resulting profile's evolution following peak morphological change during the inundation

regime (see dashed lines in Figures 3.11b and 3.12b for z_{dc} evolution). The evolution of z_{dc} begins to differ between the two profiles during the inundation regime which appears to be the result of the backbarrier environment's effect on washover deposition transported during the overwash regime, which will be discussed in the next section.

3.5 Discussion

3.5.1 The Influence of Backbarrier Marsh Properties on Cross-Shore Sediment Transport

Alongshore variability in the CH's backbarrier environment modulates shoreline change at medium-term time scales (Johnson et al., 2019). Considering that TC impacts dominate the CH's coastal morphodynamics, this variability will conceivably be evident in overwash and inundation driven sediment transport processes. It is also reasonable to assume that proximal hypsometry (i.e., the relative distribution of subaqueous and subaerial bed elevation) and land cover (e.g., vegetated versus bare earth ground condition) are the leading order backbarrier properties influencing landward sediment transport during the overwash and inundation impact regimes. Three shoreline stretches, approximately 1 km in length, were selected to represent characteristic ranges in these properties and broadly express variability in marsh surface fragmentation and ecological health. A section within the BC area (774700 to 775575 easting) and the BT area (781950 to 782725 easting) were selected to represent a completely drowned backbarrier wetland and an intermediately deteriorated marsh, respectively. A section west of BT (approximately between 780590 to 781430 easting) was included as it contains relatively uniform vegetated land cover and a solid marsh surface (this area is referred to as SM). These sections can therefore be regarded as points on a scale between healthy backbarrier marshes and those which have completely deteriorated into open water. Deterioration into open water is due to land-loss caused by, for instance, subsidence, RSLR and insufficient sediment supply. SM, BT, and BC therefore represent the healthy marsh, the intermediately fragmented stage, and the completely deteriorated backbarrier marsh on this scale, respectively. This scale could also be quantified with environmental metrics. For instance, the backbarrier wetlands' land-to-water ratio (LWR) averaged over the SM, BT, and BC subregions are 0.63, 0.31, 0.12, respectively (Johnson et al., 2019).

Figure 3.13 shows the computed cross-shore profile change and net sediment transport that are alongshore averaged within the three sections, i.e., SM, BT, and BC. The net sediment trans-

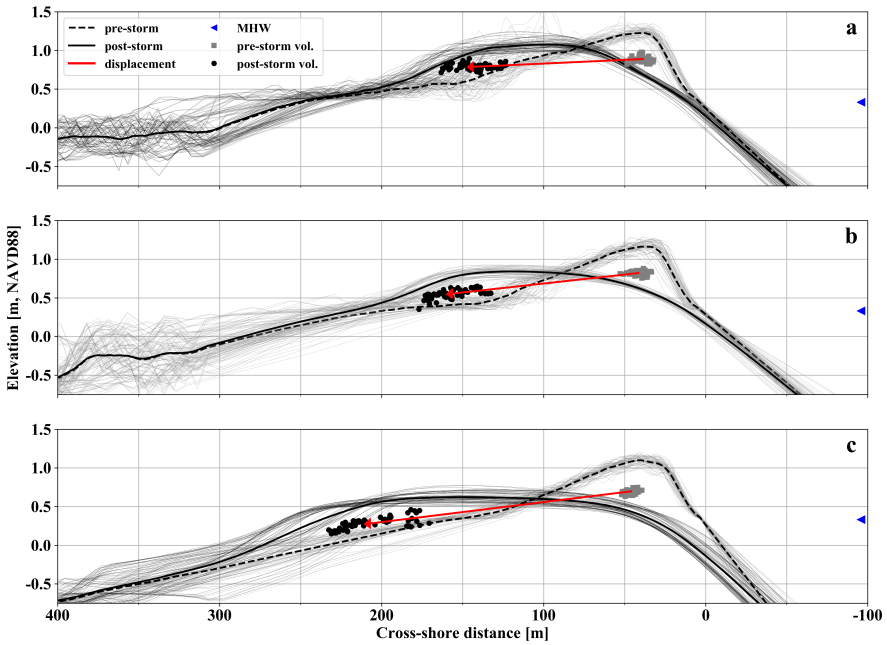

Figure 3.13: Alongshore averaged pre- and post-storm cross-shore profiles shown as dashed and solid lines, respectively. Gray profiles indicate individual transects. Centroids for pre-storm V_{sa} which was transported landward are indicated with gray squares and the centroids of post-storm washover deposition are marked with black circles where the red vector indicates mean displacement.

port was analyzed per profile by finding the centroids of the eroded pre-storm volume and the post-storm deposition and calculating the displacement between them. The cross-shore profiles were interpolated to uniform cross-shore spacing (0.5 m) from the computational (morphological) grid and aligned at the MHW contour. Eroded volume was defined as sediment above MHW, while post-storm deposition extended to the washover deposition's "pinch out", defined where bed level change was less than 1 cm.

Average net sediment transport is shown in Figure 3.13 illustrated by the red vector indicating the mean centroid displacement. Variation in net transport conforms intuitively to the scale of backbarrier wetland health. Landward transport of eroded sediment decreases from the BC section (the most deteriorated) to the SM section (the least deteriorated); while the elevation of the deposition's center of mass increases from BC to SM. Eroded sediment is transported further inland and is deposited at a lower elevation at the BC section than at the BT section and SM exhibits less landward sediment transport than BT with deposition occurring higher relative to MHW. This is presumably due to variability in the backbarrier's initial elevation and land cover as the hydrodynamic forcing, pre-storm z_{dc}, and impact regimes were similar between the sections.

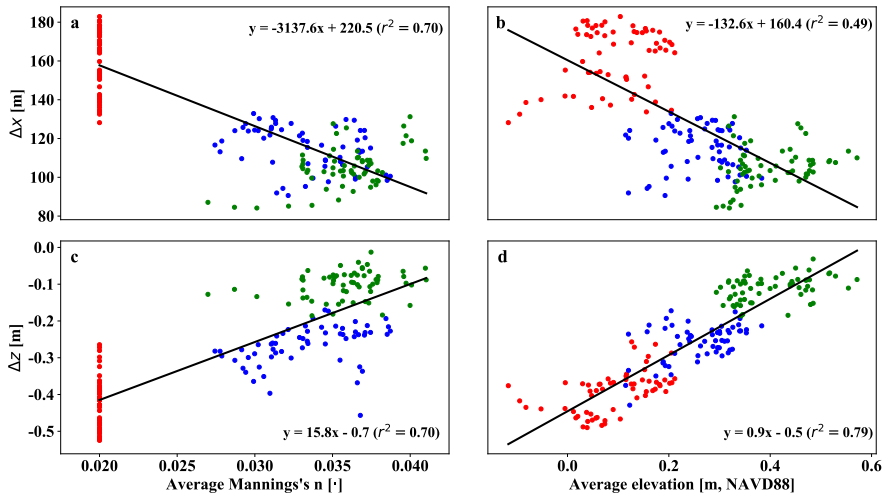

Figure 3.14: (a) and (b) correlation between horizontal displacement and average backbarrier Manning's n and average elevation, respectively. (c) and (d) correlation between vertical displacement and average backbarrier Manning's n and average elevation, respectively. The red, blue, and green indicates samples from the BC, BT, and SM areas, respectively.

Initial bed surface elevation and roughness (i.e., land cover determined Manning's n) were averaged from the pre-storm dune crest up to 400 m inland from the shoreline along grid lines to parameterize hypsometry and land cover, respectively. Vertical (Δz) and horizontal (Δx) centroid displacements at each cross-shore profile were linearly regressed against the same profile's mean elevation and initial Manning's n value. The results in Figure 3.14 indicate that overwash sediment transport is dependent on these parameters. In addition, these parameters appear well suited to express the conceptual scale as mean backbarrier elevation and bed roughness vary continuously between BC and SM (the constant Manning's n in BC is due to its uniform unconsolidated shore land cover). The landward excursion of washover (Δx) decreases linearly with increasing mean backbarrier elevation ($r^2 = 0.49, p < 0.001$) and vegetated land cover-based roughness ($r^2 = 0.70, p < 0.001$) suggesting that a healthier and more vegetated marsh increases sediment retention and promotes proximal deposition (Morton and Sallenger Jr., 2003; Wang and Horwitz, 2007). In addition, the fate of washover sediment within the tidal frame (Δz) is also influenced by elevation ($r^2 = 0.79, p < 0.001$) and land cover ($r^2 = 0.70, p < 0.001$) which is intuitive as accommodation space associated with deeper, more extensive subtidal backbarrier elevations allows for increased subaqueous deposition (Brenner et al., 2015; Lorenzo-Trueba and Mariotti, 2017).

Decreasing the elevation of washover deposition will affect aeolian recovery processes and may threaten the barrier's sustainability in response to RSLR. Following an overwash or inundation regime storm impact, aeolian sand transport from washover fans to foredunes is often

an important recovery process promoting sustainability of the coastal dunes (Miot da Silva and Hesp, 2010; Harter et al., 2015). Aeolian transport potential is dependent on the sediment's moisture content. Sediments that are deposited lower in the tidal frame will have higher moisture content and thus less potential for recovery due to increased flooding duration/frequency (Rosati and Stone, 2009; Houser and Mathew, 2011). If backbarrier marshes deteriorate and fragment, there will be a shift from environments resembling SM to that of BC in terms of hypsometry and land cover. This would lead to a decrease in the elevation of washover deposition (see Δz's trend in Figure 3.14). It is likely that the dune volume recovery rate will likewise decrease due to increased tidal flooding of these sediments. In the long term, this will increase the frequency of overwash, as insufficient recovery leaves barriers vulnerable (Houser et al., 2015), and promote the deposition of barrier sediment lower within the tidal frame as long as subaqueous accommodation space exists. It is also possible that increased overwash frequency and increased subaqueous washover deposition (i.e., reduced post-storm recovery) would reinforce each other in a manner similar to overwash frequency and local alongshore minima in foredune elevation (Houser and Hamilton, 2009). The triggering of this feedback mechanism due to backbarrier marsh drowning or die-off may threaten the ability of TC-impacted barriers to conserve subaerial mass during RSLR.

3.5.2 Influences of Sediment Availability

A numerical experiment was designed in the CH domain to assess the effects of limited foreshore sediment supply during an TC-driven sediment transport event. A non-erodible layer was specified to model the lack of sediment entrainment below the mobile sand layer. The experiment's motivation was based on the computed post-storm V_{sa}'s systematic bias (see Tables 3.3 and 3.4 and Figure 3.5), which, in part, may be explained by the abundance of sandy sediment in the model despite the CH's sand-scarce surficial geology (Harper, 1977; Kulp et al., 2005; Kindinger et al., 2001). The experiment focuses on the CH's central section where there is a relatively greater sediment deficit (Harper, 1977; Penland and Boyd, 1981; Kindinger et al., 2001) while other considerations in the model setup were not changed.

Distributions of post-storm V_{sa} per unit width in the unlimited versus the supply limited simulations are shown in Figure 3.15. Limiting the sediment supply reduced the bias ($\overline{e}$) by 28.3% within the central zone to 11.9 m^3/m from 16.6 m^3/m and reduced $\overline{e}$ by 9.7% over the entire domain. This demonstrates that limited foreshore sand supply affects the cross-shore sediment transport. The extent of this relationship is identified as a future research topic as the

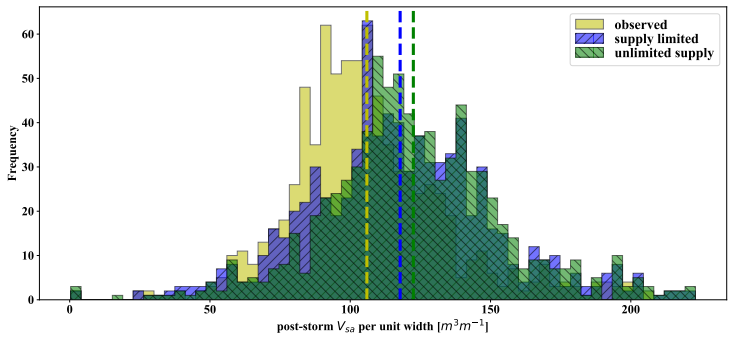

Figure 3.15: Distributions of post-storm V_{sa} per unit width in the CH's central section. Yellow, blue with forward hatches, and green with backward hatches denote the observations, supply limited, and unlimited supply scenarios. The vertical dashed lines indicate the distribution means.

true spatial distribution of the CH's sand layer thickness is unknown.

SL1 and SL2 in Figure 3.16 show cross-shore profiles for the unlimited and limited sediment supply scenarios. The difference in post-storm profile elevation, particularly in the foredune, illustrates that the overestimation of landward transport compared with the observations is decreased when the foreshore sediment supply is limited. However, the computed post-storm deposition still contains excess sediment volume compared to the observations. The observed washover fans sharply tapers (approximately -175 m cross-shore) indicating that the LIDAR surveys captured the majority of the post-storm subaerial deposition.

The observed cross-shore profiles are shown relative to pre- and post-storm aerial imagery in Figure 3.16. In Figure 3.16 the breaker line has shifted offshore despite the appearance of smaller waves. The area in between is interpreted as the exposed barrier-core due to the massive washover sediment transport. The vegetated subaerial barrier-core near the intersection of the navigational channel and the shoreline in Figure 3.16 appears to experience less erosion than that in the adjacent. A similar process has been documented for fetch-limited barrier islands within the Chesapeake Bay, USA (Cooper, 2013) and the Isle Dernieres, LA (Sallenger, 2000).

Another factor contributing to the over-estimation of post-storm V_{sa} is conjectured to be the neglect of fine sediment in the model's bed composition. This location of the CH has been documented to contain little sand in its surficial stratigraphy. Eustis (2010) took a sediment boring in 2010 (see B-9 in Figure 3.16) approximately 100 m from the post-Gustav shoreline at an elevation of 0.8 m NAVD88 and described its sediment texture and soil type. From top to the bottom of the bore sample, the first 60 cm was classified as sand-silt mixture with appreciable fines, the next 122 cm as slightly sandy clay with organics and shell fragments, and the next

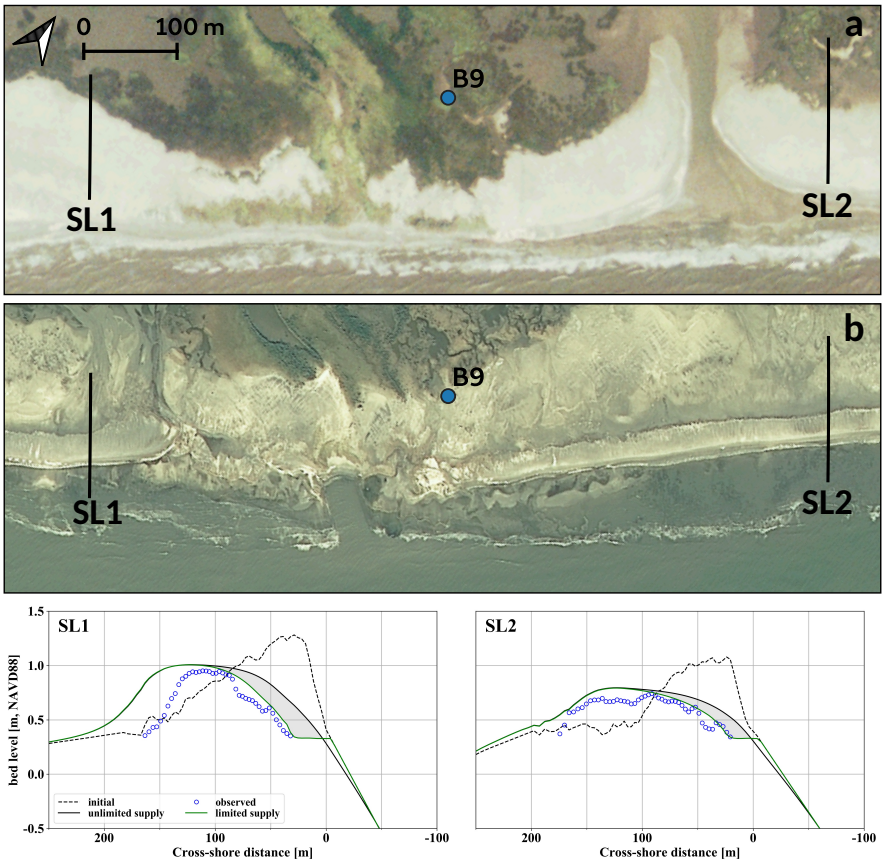

Figure 3.16: (a) Pre- and (b) post-storm aerial imagery with the location of SL1 and SL2 cross-shore transects. B-9 denotes the location of boring B-9 taken in 2010 Eustis (2010). Note the post-storm imagery also contain the effects of Hurricane Ike which is not present in the post-storm LIDAR data. (SL1 and SL2) Post-storm profile comparisons between the unlimited (black) and sediment limited (green) scenarios with LIDAR observations (blue circles) and initial bed level (dashed line). The shaded area indicates the difference in post-storm profiles.

3.35 m as very soft slightly organic clays. Plausibly, a similar stratigraphy and sedimentology comprised the bed composition which was eroded during Hurricane Gustav. Intuitively, the disintegrated fines would be transported further during the storm compared to barrier sand and likely would not be deposited within the post-storm dune. This possibly explains some of the excess computed post-storm deposition compared to the observations as the model's sediment transport formulations and inputs treat the bed composition as pure sand.

Ultimately, an accurate estimation of the CH's surficial morphostratigraphy and erodible layer thickness is essential for understanding sediment supply during TC-driven sediment transport at this site. Even limited core or grab sample collections within a subregion (e.g., BT) would mitigate the difficulty of obtaining subsurface samples; nevertheless, sampling the nearshore, particularly the surfzone, would still prove extremely challenging. However, it may be possible to correlate sediment core observations with high-frequency subbottom seismic profiles to achieve a representative distribution of the mobile sand layer's thickness within the nearshore.

3.5.3 Implications for Barrier Design and Coastal Management

The backbarrier wetlands' role in TC-driven sediment transport has ramifications to coastal management and engineering in relation to RSLR and beach/dune restoration design. It has been recognized that vertical marsh accretion can be outpaced by RSLR leading to marsh drowning and land loss (Orson et al., 1985; FitzGerald et al., 2008; Blum and Roberts, 2009; Weston, 2014). The resulting coastal morphodynamic effects are frequently discussed in terms of an increased tidal prism and the sequestration of additional barrier sediment within subaqueous tidal deltas. The computed sediment transport results indicate, however, that the drowning of marshes may produce additional coastal morphodynamics effects through storm-driven washover sediment transport processes. If marsh drowning occurs within the adjacent backbarrier wetlands, resulting in the conversion of proximal wetland land cover to open water and decreasing the hypsometry, then an increase in landward transport of nearshore sediment may be expected if overwashing or inundation occurs. Without increased sediment input to the active beach profile, the increased sediment export will negatively affect sediment budgets of the barrier sand body and lead to (increased) shoreline erosion and barrier fragmentation (FitzGerald et al., 2008).

Marsh drowning and land-loss is expected to become more widespread throughout the coastal zone (Weston, 2014) as eustatic sea-level rise accelerates (Oppenheimer et al., 2019). Barrier drowning due to RSLR over long-term timescales has received significant attention (FitzGerald et al., 2008; Moore et al., 2010, 2014), but may not be tractable to engineering solutions.

As shown in this study, the backbarrier marsh's role in retaining subaerial sediment during overwash/inundation processes operates at time- and length scales which may be influenced by coastal engineering activities. Restoring relatively small areas of backbarrier marsh, as opposed to offsetting the land-loss which affects coastal bay tidal prisms, may have a large influence on shoreline morphodynamics for TC impacted coastlines.

The simultaneous restoration/creation of backbarrier marshes in conjunction with beach/dune renourishments is an engineering solution found in practice to offset shoreline erosion. This design method is predicated on the practical understanding that, if overwash events are likely, then it is best to elevate foredunes to reduce their occurrence and provide an intact platform for subaerial washover deposition. The results herein support the simultaneous restoration of wetlands and provide a basis for further improvement of existing restoration design solutions. For instance, the computed sediment transport results at BC3 and BT3 suggest that the overwash regime quickly reduces foredune elevation and, within the subsequent inundation regime, landward sediment transport distance is dependent on the backbarrier wetland. Assuming that overwashing will occur in the project's design lifetime, prolonging sediment retention within the backshore/foreshore system through the construction of a broader subaerial beach nourishment along with backbarrier marsh creation may be more advantageous than increasing foredune elevation via dune nourishment. Future work will address this issue through a series of numerical experiments which vary restoration design targets and TC forcing.

3.6 Conclusions

A large-scale hydrodynamic model of the northern Gulf of Mexico was coupled with a local-scale sediment transport/morphological model of the Caminada Headlands, Louisiana to simulate Hurricane Gustav's impact to a low-lying mainland barrier. The computed results exhibited a good agreement in terms of tropical cyclone-driven storm surge and surface waves at a number of coastal and intertidal wetland observation stations. Computed bed level dynamics were compared with pre- and post-storm LIDAR surveys. The results show good skill in modeling overwash processes and post-storm deposition patterns on the backshore in the unprotected, central area and reasonable skill over the entire domain. The sediment transport model was used to investigate the tropical cyclone-driven sediment transport and morphological response processes over the Caminada Headland's low-lying coastal topography and variable backbarrier environments. The unique characteristics of these processes include: (1) the majority of net sediment transport occurs during a short-duration (approximately 2 hours) overwash regime as the low-elevation

coast is rapidly inundated; (2) inland washover sediment transport distance is influenced by the backbarrier topography/surface roughness as increased accommodation space/reduced roughness allows for more landward sediment transport.

The following summarizes the main findings.

1. A large-scale hydrodynamic-wave model was successfully coupled with a local-scale morphodynamic model of a low-lying mainland barrier to simulate Hurricane Gustav's impact to the coastal geomorphology. The model incorporates the most recent and highest quality input data in terms of topo-bathymetry and surface roughness.

2. Washover sediment transport is found to be dependent on backbarrier bed friction and elevation. For similar pre-storm dune elevation and impact regimes, cross-shore profiles with lower backbarrier elevation and less vegetated land cover exhibit increased landward sediment transport. Simultaneous restoration/creation of backbarrier marshes with beach/dune renourishments may serve as a engineering solution to offset increased washover sediment transport at tropical cyclone impacted coastlines.

3. The evolution of a low-lying mainland barrier subject to tropical cyclone generated hydrodynamic forcing shows a response that follows the impact regimes of Sallenger (2000). However, the distinction between the overwash and inundation regime, in terms of morphological response, is not clearly evident. Further, the inundation regime does not appear as effective in generating landward sediment transport as the low-lying topography is significantly reduced during the overwash regime.

4. Biases in computed post-storm dune volume and tropical cyclone-driven landward transport at the Caminada Headlands are partially explained by a nearshore sediment deficit. Other potential explanations are the abundance of fines in the bed composition.

CHAPTER 4

CHARACTERISTICS OF TROPICAL CYCLONE FORCING TO BEACH AND DUNE RESTORATIONS IN CONJUNCTION WITH BACKBARRIER MARSH CREATION SCENARIOS

4.1 Introduction

Vulnerable coastlines are often restored and fortified by renourishing the main barrier sand body to offset natural shoreline erosion and protect against future storm impacts (Dean, 2002). It is therefore imperative to predict the fate of placed sediment, which provides vital information for decision-making and the design practice for restoration. Understanding potential sediment transport pathways, particularly the mode of sediment transport or loss rates, will help provide design constraints to coastal engineers and develop strategies for optimal sand resource management. For many mid- and low-latitude coastlines, the major driver of high sediment transport and loss rates are tropical cyclone (TC) impacts (Morton et al., 1995; Stone et al., 1997; Morton and Sallenger Jr., 2003; Georgiou et al., 2005). In this regard, understanding the sediment transport mechanisms and their interaction with the natural features during a TC event are central to assessing the sustainability of the restoration projects and, possibly, developing strategies to improve the resilience of the barriers.

Sediment transport and morphological change driven by TC impacts is, to the first order, controlled by the event's maximum water level elevation relative to the barrier's dune crest elevation (Sallenger, 2000). Accordingly, restoration design mostly aims at achieving profile elevations higher than the design water levels. However, the backbarrier elevation and its land cover also influence event-scale sediment transport. This is mostly because vegetated land cover and increased elevation promotes deposition and reduces landward sediment transport (Morton and Sallenger Jr., 2003; Wang and Horwitz, 2007; Johnson et al., 2019). Backbarrier marshes are natural features of most barrier systems and are integral to physical/ecological systems. They also supply many benefits such as improving the water quality, providing habitats for species, and attenuating storm surge/waves (Woodroffe, 2007; FitzGerald et al., 2008; French et al., 2016). Therefore, consideration of the backbarrier environment's defensive capabilities during beach and dune restoration design aligns with the principles of working-with-nature and long-term resiliency. However, knowledge of the backbarrier's effects on beach and dune restorations in response to TC impacts is still limited and deserves further study.

The objective of this study is to test the effect of the backbarrier elevation and land cover on the sediment retainment capacity of barrier systems that experience frequent overwash under TC forcing. To address this question, we use a physics-based numerical model to investigate the morphological response of three different restoration strategies under two different TC forcing with different backbarrier elevation and land cover. A previously verified sediment transport-morphodynamic modeling system (XBeach) is set up using accurate input data from a recent large-scale restoration in coastal Louisiana (LA) and hindcast storm conditions from Hurricane Gustav (2008) in the Caminada Headlands (CH). The CH restorations (Byrnes et al., 2015; Coastal Engineering Consultants, 2015; Jafari et al., 2018) serve as the basis for the numerical experiments which vary the physical and ecological configuration of the restoration scenarios.

In this section a brief introduction with relevant literature was provided; in Section 4.2, the numerical model set up and input is described; Section 4.3 presents the sediment transport and morphodynamic modeling results; model sensitivity to vegetation height and the role of marsh creation in barrier restoration is discussed in Section 4.4; finally, a summary of the main findings are reported in Section 4.5.

4.2 Materials and Methods

4.2.1 Restoration Scenarios

The CH Beach and Dune Restoration Project placed approximately 2.38×10^5 m^3 of sand mined offshore from Ship Shoal along 21.3 km of the CH's shoreline (see the green polygon in Figure 4.1). The pre-restoration profile lacks a discernible foredune and the maximum elevation is around 1.5 m by using the North American Vertical Datum of 1988 as reference, i.e., 1.5 m NAVD88. The post-restoration design targets an elevation of 1.37 m NAVD88 beach that is 20 m-wide. Target dune crest elevation is 2.13 m NAVD88 over a width of 88.4 m, see Figure 4.2 for a representative profile (Coastal Engineering Consultants, 2015). The marsh creation project was designed to span from Port Fourchon to Elmer's Isle (see purple polygon in Figure 4.1) and will create approximately 5.6 km^2 of marshland at an elevation of 0.76 m NAVD88 (Ardaman & Associates, 2018). The three post-construction scenarios used in the numerical experiments are directly based on these design specifications (see Section 4.2.2).

The first restoration scenario reflects the actual "as-built" morphology of the CH after the beach and dune restoration was completed (BD scenario). The BD scenario was set up by incorporating the post-construction survey data (see Section 4.2.2). The restoration design template, shown in Figure 4.2, indicates that the subaerial profile's elevation was increased for a

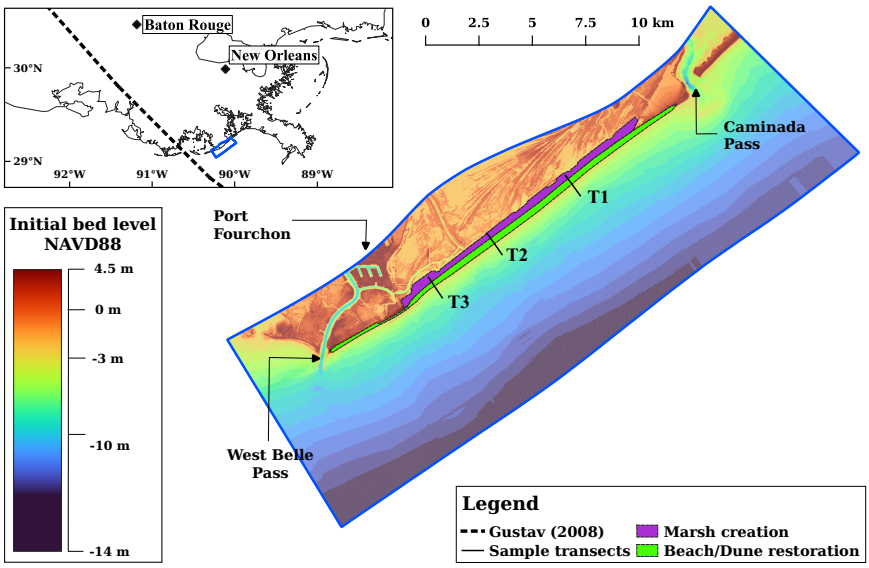

Figure 4.1: The CH model grid and initial bed level. The inset shows the CH domain relative to LA and Hurricane Gustav's (2008) track. The marsh creation and beach/dune restoration footprint geometries are displayed as purple and green polygons, respectively. Sample transects T1, T2, and T3 are shown with black lines.

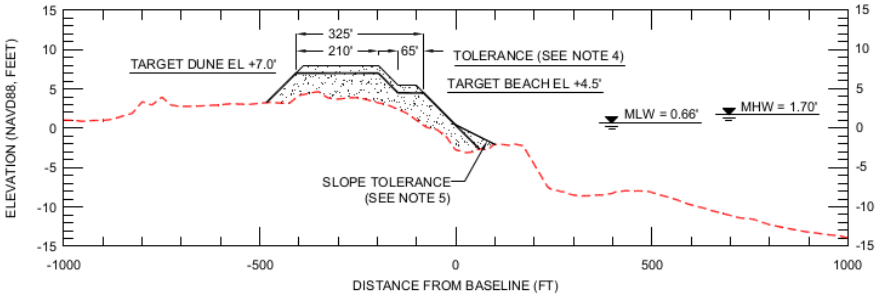

Figure 4.2: Typical design profile for the Caminada Beach and Dune Restoration. The pre-existing grade is shown as a red dashed line and the placement geometry is the dot-filled polygon with the construction tolerance shown as a buffer on the placement geometry. Modified from BA0 (2019).

width of approximately 150 m and the dune crest was raised to an elevation of 2.13 m NAVD88.

The second scenario (MC scenario) includes the beach and dune restoration but further incorporates the backbarrier marsh creation project. The last scenario models the complete deterioration of the backbarrier wetland (WD scenario) into open water and is diametrically opposed to the MC scenario. Figure 4.3 shows the initial topo-bathymetry for the BD, MC, and WD scenarios at sample transects T1, T2, and T3.

4.2.2 Morphodynamic Model

A coupled large-scale hydrodynamic-wave model (Delft3D-Flow version 64519 and SWAN version 4072ABCDE) covering the eastern Atlantic Ocean basin and the Gulf of Mexico, which

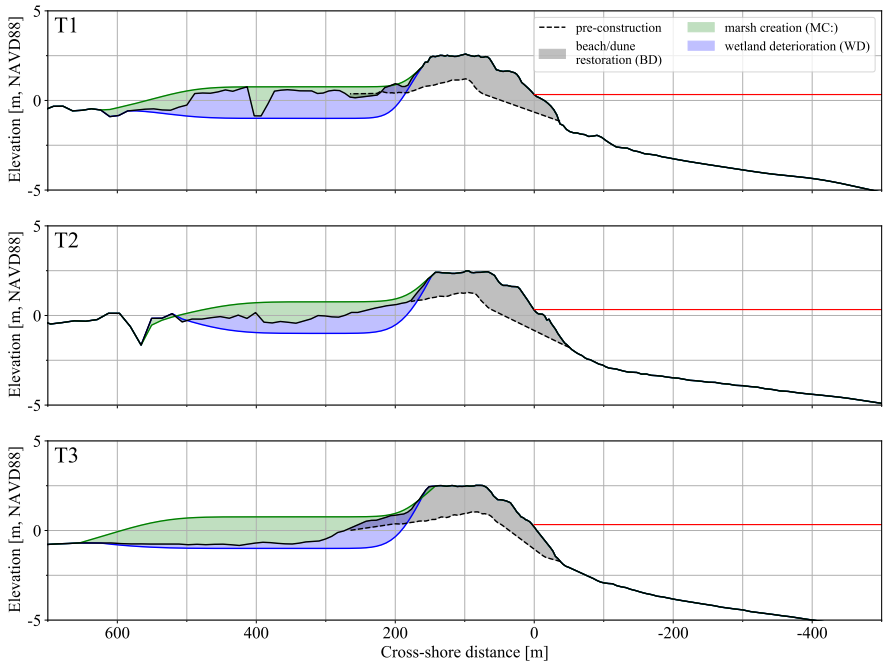

Figure 4.3: Initial topo-bathymetric inputs for the BD (black), MC (green) and WD (blue) restoration scenarios at sample transects T1, T2, and T3. The pre-restoration profile is shown as a dashed line. The gray, green, and blue shaded areas are the difference between the restoration scenario profiles and pre-restoration profile, respectively.

has been verified for Hurricane Gustav (2008) (Liu et al., 2018; Johnson et al., 2020), used to generate water level and surface wave boundary conditions for a local-scale morphodynamic-sediment transport model (XBeach-X release, version 5526). XBeach has been used extensively for modeling TC impacts (Roelvink et al., 2009; McCall et al., 2010; Lindemer et al., 2010; Sherwood et al., 2014; Nederhoff et al., 2015; Smallegan et al., 2016; Harter and Figlus, 2017; Roelvink et al., 2017; Smallegan et al., 2017; Passeri et al., 2018; Schambach et al., 2018; van der Lugt et al., 2019; Johnson et al., 2020). The local-scale model of the Caminada Headlands (CH model) was previously calibrated and verified to hindcast Hurricane Gustav's impact using surface wave, hydrological and morphological observations (Johnson et al., 2020). As part of this process, a remotely-sensed land cover/land use (LULC) classification was produced from Landsat 5 (TM) imagery and calibrated to a Manning's n-based surface roughness. The same CH model (see Figure 4.1) is used here, but its topo-bathymetric and LULC-based surface roughness inputs are modified to reflect the CH's post-construction state in the different restoration scenarios.

The new topo-bathymetric data, incorporated to model the CH's post-restoration state, are comprised of real-time kinematic global positioning system (RTK-GPS) and single-beam sonar hydrographic survey data. RTK-GPS and hydrographic data were collected in December

12^{th}, 2014 and May 25^{th}, 2016 during the post-construction phases of the BA-45 and BA-143 restoration projects, respectively. These surveys total 902723 elevation observations that spans across the CH's entire shoreline, beginning at approximately the -5 m NAVD88 contour and ending approximately 200 m past the post-construction shoreline. These "as-built" elevations captured the post-construction morphology of the CH's beach and dunes. An additional single-beam sonar hydrographic survey was conducted between October 29^{th} and November 10^{th}, 2015 as part of the Louisiana Barrier Island Comprehensive Monitoring (BICM) Project Phase 2 which extended out to approximately -14 m NAVD88 (Byrnes et al., 2015). To set up the post-construction scenarios, these survey data sets were triangularly interpolated to the CH model's grid and the remaining grid points were sampled from the Coastal National Elevation Database (CoNED) digital terrain model (DTM) Thatcher et al. (2016). To update the LULC-based surface roughness distribution to post-construction conditions following the restoration's construction, Landsat 8 (TM) imagery from December 10^{th}, 2016 was acquired. The remotely-sensed data were classified following the methodology in Johnson et al. (2020).

For the restoration scenarios, the input topo-bathymetry and roughness fields were generated based on restoration design documents and post-construction data (Coastal Engineering Consultants, 2015; Ardaman & Associates, 2018). The backbarrier marsh creation was set up in the model by uniformly setting the elevation of the grid points within the marsh creation footprint to the design elevation of 0.76 m NAVD88 (Ardaman & Associates, 2018). The created marshland is assumed to have a uniform LULC and Manning's n value (0.034) corresponding to backbarrier vegetation in (Johnson et al., 2020). The marsh creation was then smoothly merged with the surrounding topo-bathymetry and surface roughness inputs within a 50 m buffer distance. To set up the WD scenario, water bodies in the CH's backbarrier were randomly sampled and averaged to yield an elevation of -0.64 m NAVD88. This elevation was assigned to grid points within the marsh creation footprint and smoothly merged with adjacent elevations within a 50 m buffer. Within the same polygon, the LULC was set to open-water with a Manning's n of 0.020.

4.2.3 Storm Conditions

Two storm conditions were used to force the CH model. Forcing was imposed as water levels on all boundaries and surface wave boundary conditions on the offshore boundary (see Figure 4.1). One set of conditions (see Figure 4.4a, c, and e) were identical to those produced by Hurricane Gustav (2008) (HG conditions) and have previously been verified within the CH model (Johnson et al., 2020). An additional set of conditions (see Figure 4.4b, d, and f) were synthesized

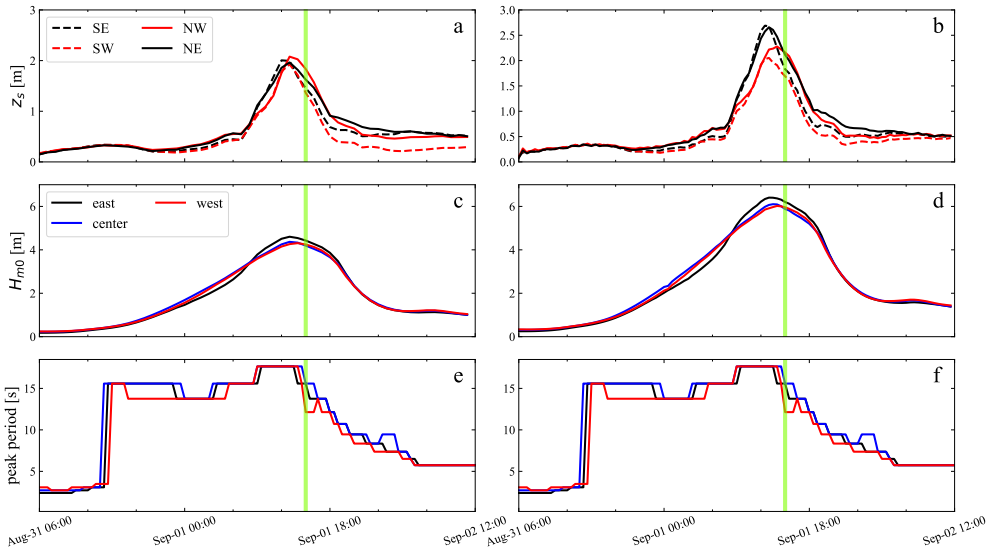

Figure 4.4: Water level and surface wave boundary conditions. (a) Hurricane Gustav water levels at the CH model's boundary where the dashed black and red lines indicate the southeast (SE) and southwest (SW) corners, respectively, and solid black and red lines indicate the northeast (NE) and northwest (NW) corners, respectively. (b) Water levels in 100 year conditions with same line styles as (a). (c) Offshore zero-moment wave height for Hurricane Gustav at three offshore locations: east (black line), central (blue), and west (red). (d) Offshore zero-moment wave height for the 100 year conditions with same line styles as (b). (e) Peak period for Hurricane Gustav conditions with same line styles as (b). (f) Peak period for the 100 year conditions with same line styles as (b). The tropical cyclone's landfall is shown as a vertical green line.

to simulate 100-year return period forcing along a track identical to Hurricane Gustav's (see inset in Figure 4.1). To generate the conditions for 100-year return period, the HG boundary conditions are scaled by ramp functions, where were different for water level and zero-moment wave height (H_{m0}). Maximum value of the ramp functions are equal to the ratio between the 100 year return period conditions and Hurricane Gustav's peak values for both water level and H_{m0}.

Mean sea level (MSL) is estimated as 2.13 m for a 100-year return-period water level and the peak water level of 1.36 m MSL observed during Hurricane Gustav, which were acquired from the National Oceanographic and Atmospheric Administration (NOAA) Grand Isle (GI) tidal station (CO-OPS id: 8761724), approximately 15 km to the northeast of the CH. The scaling factor, denoted as α with superscripts wl and H_{m0} indicating those used for water level and zero-moment wave height, respectively, was therefore calculated as $\alpha_{wl} = 2.13m/1.36m = 1.57$. The value obtained was used to smoothly scale the HG water level at the boundaries to approximate the water levels for a hypothetical storm with a 100-year return period (see Figure 4.4a and b, respectively).

A similar procedure was employed to scale up the surface wave boundary conditions for

100-year return period at the offshore boundary. The relationship for H_{m0} is obtained from the Wave Information Studies (WIS) station 73129, given as $H_{m0}(T_r) = 3.1452 + 1.6284\log(T_r)$ with T_r being the return period in years, and was used to calculate H_{m0} for 100-year return period. The maximum H_{m0} associated with Hurricane Gustav at this WIS station was 7.64 m which yields a scaling factor of $\alpha_{H_{m0}} = 10.6443m/7.6400m = 1.39$. Since the surface wave boundary conditions are imposed as directional wave spectra, the HG energy spectra were scaled with a ramp function which has a peak factor of $\alpha^2_{H_{m0}}$ (see Figure 4.4c and d for the HG and 100 year conditions, respectively). The distribution of energy density in frequency and directional space was kept the same as that is used in HG so that the peak frequency and mean direction in the HG and 100-year conditions are identical.

4.3 Results

4.3.1 Morphodynamics

To contextualize our discussion on hurricane-induced morphodynamic changes, it is worth describing the impact regimes. Following Sallenger (2000), impact regimes are defined as: (i) *swash* that occurs when maximum water level for a given interval (1 hr) does not exceed mean high-water (MHW); (ii) *collision* that occurs when maximum water level exceeds MHW but is less than the dune crest (z_{dc}); (iii) *overwash* that occurs when the maximum water level exceeds z_{dc} but the minimum water level does not; and (iv) *inundation* that takes place when the minimum water level exceeds z_{dc}. Figure 4.5 shows the pre- and post-storm profiles at T1, T2, and T3 for each restoration scenario under the HG storm conditions along with the maximum mean water levels.The backbarrier mean water levels approached the dune crest elevation (approximately 2.35 m NAVD88), but never establish a connection with the ocean. Therefore, the HG storm conditions never initiated the inundation regime due to the CH's restored dune elevation. Although the inundation regime was never reached, duneface sediments were transported to the dune's leeward side and offshore. The seaward sediment transport is almost identical at these transects for all the restoration scenarios, but a slight morphological difference in the small washover deposition is noted.

The 100-year storm conditions produced inundation regime forcing at transects T1, T2, and T3 as indicated by the maximum mean water levels in Figure 4.6. As expected, the result of the inundation regime forcing is landward transport of beach and dune sediment. The profiles' net change indicate that dune lowering between each scenario is morphologically similar, but there are quantitative differences. The presence of a restored backbarrier marsh (scenario MC) decreases

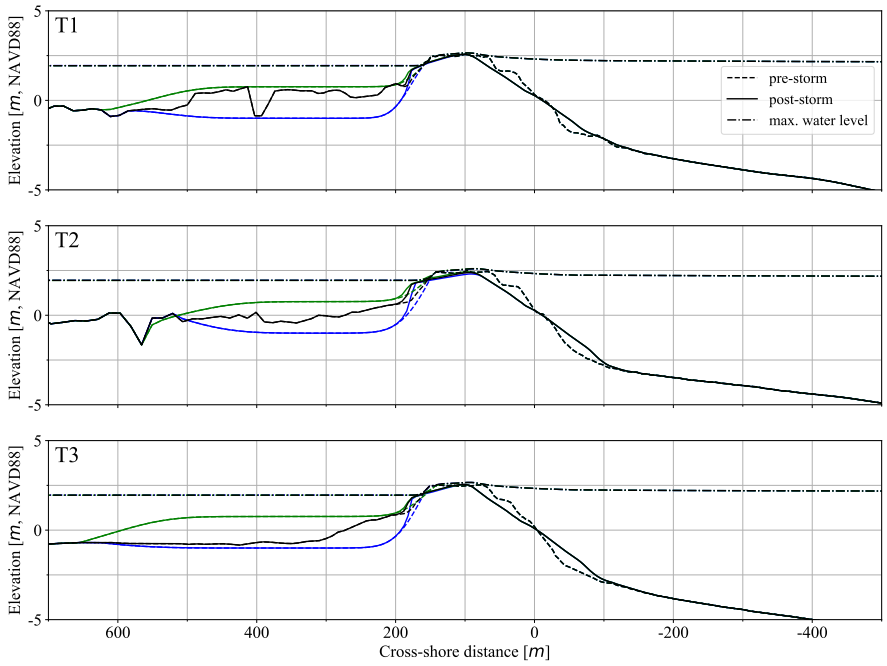

Figure 4.5: Pre- and post-storm profiles for the HG storm conditions shown as dashed and solid lines, respectively. The BD restoration is shown as black, the MC as green, and the WD as blue lines. Maximum water levels over the entire event are shown as dash-dot lines.

the amount of lowering compared to scenarios BD and WD. The post-storm z_{dc} decreases with decreasing backbarrier elevation at every transect, where WD has a lower post-storm dune than BD, which is likewise lower than MC. Comparing the profiles from scenario MC to WD reveals a conspicuous difference in that the horizontal landward excursion of washover increases when the backbarrier marsh is present (MC scenario) compared to the WD scenario with open-water landward of the dune.

Figure 4.7 shows the displacements of eroded beach and dune sediment onto the backbarrier at the sample transects after a hurricane with 100-year return period. The spatial comparison between the centroids of eroded pre-storm sediment volume and the post-storm deposition allows us to analyze the sediment displacement of sediment. The pre- and post-storm profiles were alongshore-averaged over a one-kilometer shoreline stretch centered at T1, T2, and T3. These transects highlight the general deposition patterns along CH. Landward sediment migration in the MC scenario is more emphasized as opposed to those in BD and WD scenarios. However, the opposite is the case of the sediment's vertical displacement (Δz) which is deposited at a higher elevation in the MC scenario than in the BD and WD scenarios. This suggests that the volume of sediment eroded is similar in all the cases, and the landward migration determines the vertical displacement of the dune crest. The results also indicate that approximately half of the

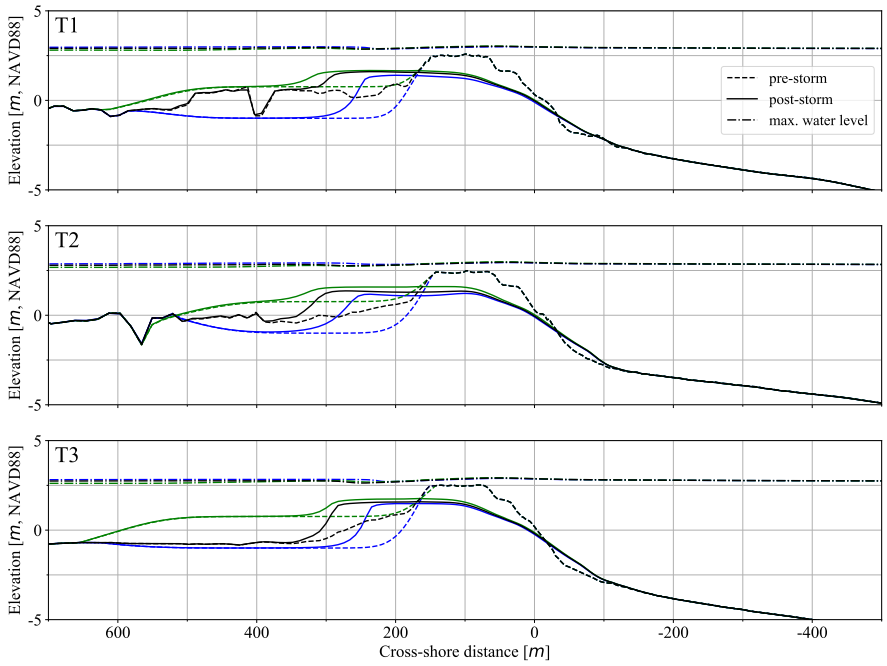

Figure 4.6: Pre- and post-storm profiles for the 100 year storm conditions shown as dashed and solid lines, respectively. The BD restoration is shown as black, the MC as green, and the WD as blue lines. Maximum water levels over the entire event are shown as dash-dot lines.

post-storm sediment transport in the WD scenario is deposited below MHW.

Figure 4.8, which shows the distributions of sediment transport at each profile within the alongshore averaging section, contrasts the horizontal and vertical components of washover sediment transport under the 100-year storm condition. Since the HG forcing did not result in overwash, its deposition patterns are not part of the current analysis. In terms of vertical displacement (Δz), there is a clear order to the scenarios where the mean Δz is -0.47 m, -0.98 m, and -1.4 m for the MC, BD, and WD scenarios, respectively. The MC's narrow Δz distribution relative to the others is likely due to the uniform elevation of the backbarrier marsh platform on which the washover transport was deposited. Identifying the trends in the horizontal displacement is less straightforward. From the distributions of Δx, less landward sediment transport clearly separates WD scenario from BD and MC; however, there is no clear trend to describe the difference in sediment displacement for BD and WD scenarios. In summary, under the 100-year forcing, landward horizontal sediment transport increases with increased backbarrier elevation, while vertical displacement becomes more negative with decreasing backbarrier elevation.

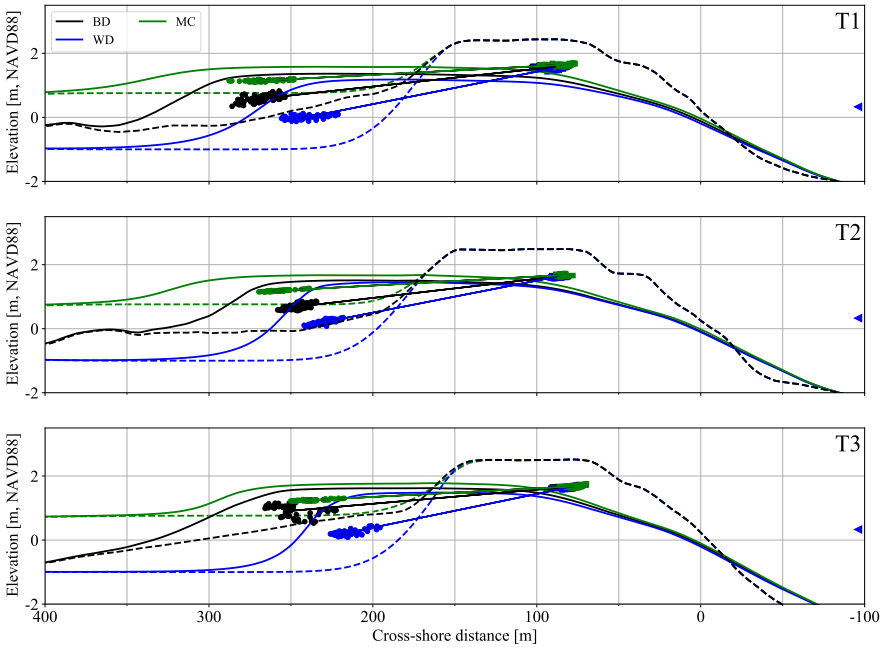

Figure 4.7: Alongshore averaged transport of dune volume at sample transects T1, T2, and T3. The BD, MC, and WD restoration scenarios are represented with black, green, and blue lines. The pre- and post-storm profiles are shown as dashed and solid lines respectively. Centroids of the pre-storm dune volume and post-storm deposition are indicated with squares and circles, respectively. The displacement between the two is indicated with vector.

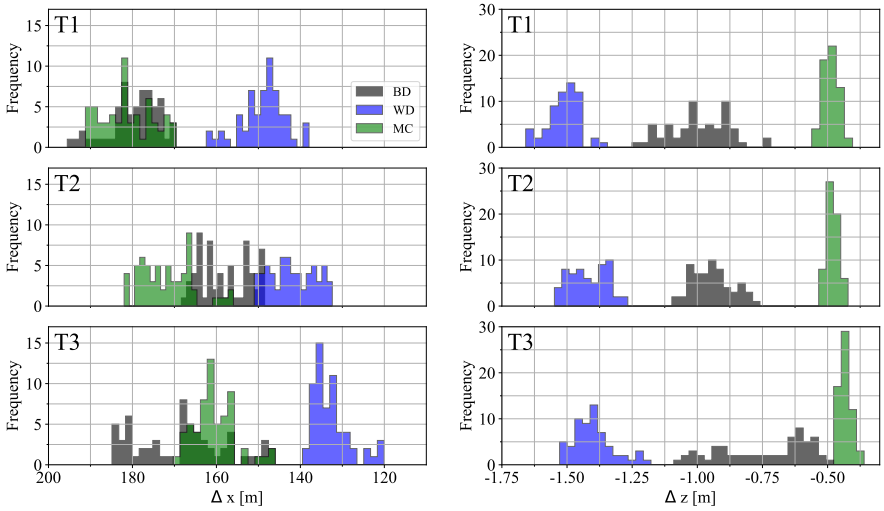

Figure 4.8: Distributions of sediment displacement components, i.e., Δx and Δy at sample transects T1, T2, and T3. The BD, MC, and WD restoration scenarios are represented with black, green, and blue shaded areas.

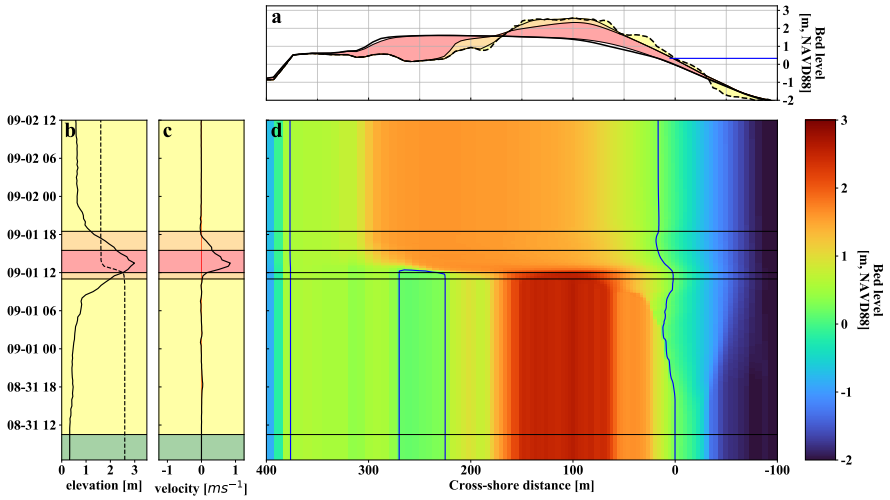

Figure 4.9: Cross-shore bed level evolution at T1 for the BD scenario under 100 year storm conditions. (a) Cross-shore profiles and MHW (blue line). The dashed and solid black lines are the initial and final bed levels, respectively. The yellow, orange, and red areas indicate profile change over the first collision, overwash, and inundation regimes, respectively. (b) Time-series of water level (solid) and z_{dc} elevations (dashed). (c) Time-series of cross-shore current velocity at the shoreline in (a). The green, yellow, orange, and red shaded areas in (b) and (c) indicate the swash, collision, overwash, and inundation regimes, respectively. (d) Time-stack of bed levels showing the profile's evolution with the MHW contour (blue line) for reference.

4.3.2 Impact Regimes

100 Year Storm Forcing

Figures 4.9, 4.11, and 4.10 are time stacks showing the morphological and forcing evolution at profile T1 under the 100 year storm conditions within the BD, WD, and MC scenarios, respectively. Panel a within the Figures 4.9, 4.11, and 4.10 shows the profiles after each impact regime with cross-sectional area changes during different impact regimes, where yellow, orange and red colors indicate the profiles after collision, overwash and inundation regimes, respectively. Panel b shows the mean water level and z_{dc} time series as well as the succession of impact regimes. Panel c in the same figure shows time series of cross-shore velocity at MHW, and panel d presents the time stack of bed level changes.

For the storm with 100-year return period, profile T1 is within the collision regime for approximately 24 hours before a two-hour long overwash regime. During the collision regime, sediment transport patterns are similar for all the scenarios where duneface sediment was transported offshore. During the overwash regime, more landward sediment transport from the dune crest is observed for WD scenario compared to those in the BD and MC scenarios.

Cross-shore velocity at the MHW contour of the initial profile, shown in panel c of Figures 4.9, 4.11, and 4.10, starts increasing during the overwash regime, and accelerates sharply

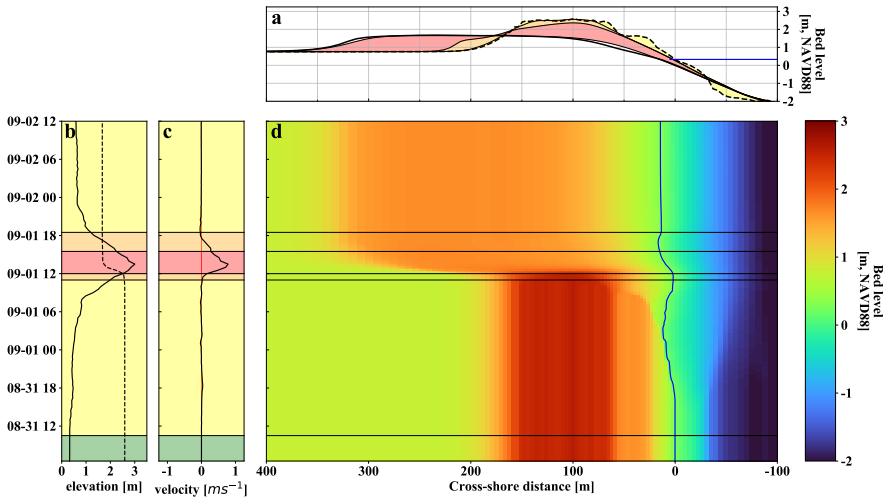

Figure 4.10: Cross-shore bed level evolution at T1 for the MC scenario under 100 year storm conditions. (a) Cross-shore profiles and MHW (blue line). The dashed and solid black lines are the initial and final bed levels, respectively. The yellow, orange, and red areas indicate profile change over the first collision, overwash, and inundation regimes, respectively. (b) Time-series of water level (solid) and z_{dc} elevations (dashed). (c) Time-series of cross-shore current velocity at the shoreline in (a). The green, yellow, orange, and red shaded areas in (b) and (c) indicate the swash, collision, overwash, and inundation regimes, respectively. (d) Time-stack of bed levels showing the profile's evolution with the MHW contour (blue line) for reference.

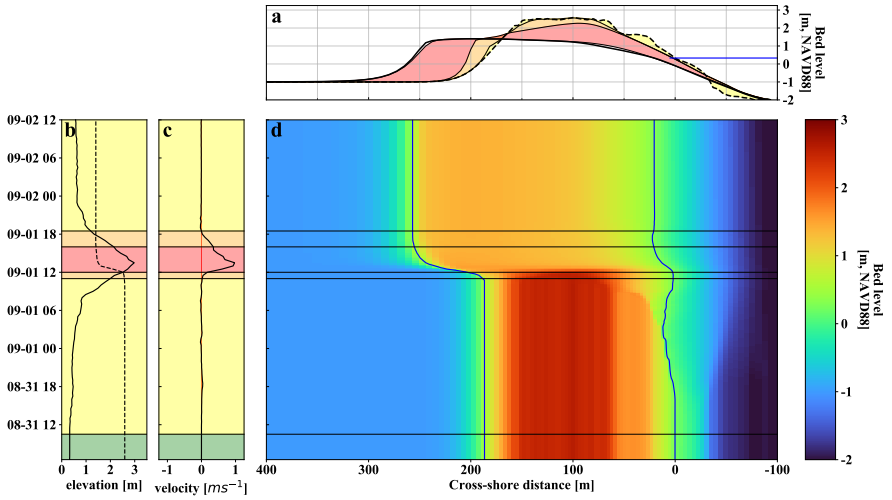

Figure 4.11: Cross-shore bed level evolution at T1 for the WD scenario under 100 year storm conditions. (a) Cross-shore profiles and MHW (blue line). The dashed and solid black lines are the initial and final bed levels, respectively. The yellow, orange, and red areas indicate profile change over the first collision, overwash, and inundation regimes, respectively. (b) Time-series of water level (solid) and z_{dc} elevations (dashed). (c) Time-series of cross-shore current velocity at the shoreline in (a). The green, yellow, orange, and red shaded areas in (b) and (c) indicate the swash, collision, overwash, and inundation regimes, respectively. (d) Time-stack of bed levels showing the profile's evolution with the MHW contour (blue line) for reference.

once the dune is inundated (red shaded area). The majority of the sediment transport occurs during the inundation regime in all the scenarios which lasts approximately 4 hours. From Figures 4.9, 4.11, and 4.10, one can observe that sediments eroded from the dune crest form thick washover deposits landward of the pre-storm dune. The thickness of the deposition during the inundation regime depends on the pre-storm topography. WD exhibits the thickest, but the shortest deposition; whereas MC shows the most elongated but the thinnest deposition. Following the inundation regime, a second overwash regime occurs and produces a relatively small amount of landward transport onto the leeward side of the newly deposited washover sediment. No significant flow reversal occurs in the 100 year storm conditions under any restoration scenario. Overall, the majority of sediment transport occurs during the inundation regime, and the deposition patterns are tightly linked to the accommodation space in the backbarrier, which depends on the backbarrier's pre-storm topography.

Gustav-Like Forcing

Figures 4.12 and 4.13 show the morphological evolution of T1 under Gustav-like conditions for the WD and MC scenarios, respectively. Since the inundation regime did not occur under the HG storm conditions (in panel b of Figures 4.12 and 4.13, the mean water level never exceeds the dune crest elevation), these profiles do not exhibit notable landward transport. In both the WD and MC scenarios, there is erosion at the duneface and offshore transport during the initial collision regime. The following overwash regime, which lasts approximately 1 hour, produces discernible, but small amounts of landward transport. Overall, the restoration scenarios examined here, which vary with respect to the backbarrier accommodation space and surface roughness, do not significantly affect storm impacts unless extended overwash or inundation regimes occur.

4.3.3 Domain-Wide Morphodynamics

To holistically assess the effect of the different restoration scenarios on the CH, change in the pre- and post-storm subaerial sediment volume is plotted along the CH's shoreline in Figure 4.14. Subaerial volume calculations were limited to grid cells with elevations above MHW which were contiguous with the main barrier sand body. The net change in subaerial volume (ΔV_{sa}) was calculated at cross-shore grid lines between the input and output topography.

The green and magenta areas indicate the shoreline sections that are protected by structural defenses (break waters, seawall and geotube, and a jetty) and involved with inlet/spit processes, respectively. These sections historically exhibit different morphodynamic characteristics from

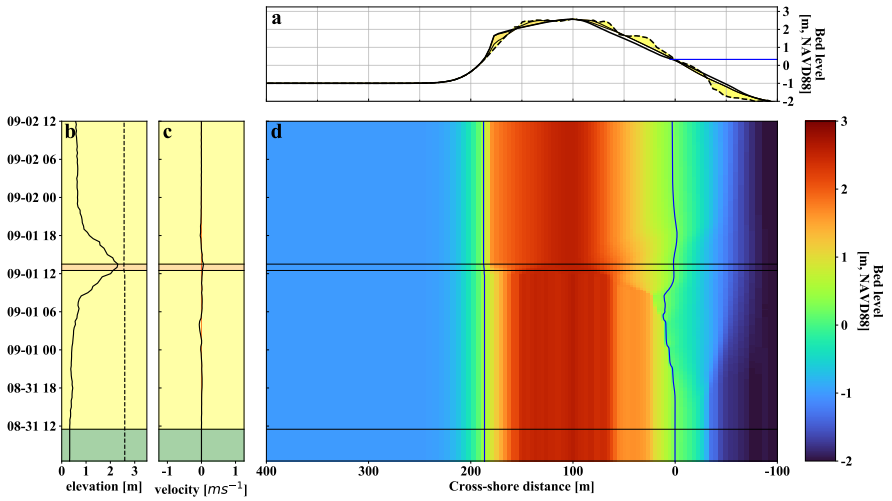

Figure 4.12: Cross-shore bed level evolution at T1 for the BC scenario under HG storm conditions. (a) Cross-shore profiles and MHW (blue line). The dashed and solid black lines are the initial and final bed levels, respectively. The yellow, orange, and red areas indicate profile change over the first collision, overwash, and inundation regimes, respectively. (b) Time-series of water level (solid) and z_{dc} elevations (dashed). (c) Time-series of cross-shore current velocity at the shoreline in (a). The green, yellow, orange, and red shaded areas in (b) and (c) indicate the swash, collision, overwash, and inundation regimes, respectively. (d) Time-stack of bed levels showing the profile's evolution with the MHW contour (blue line) for reference.

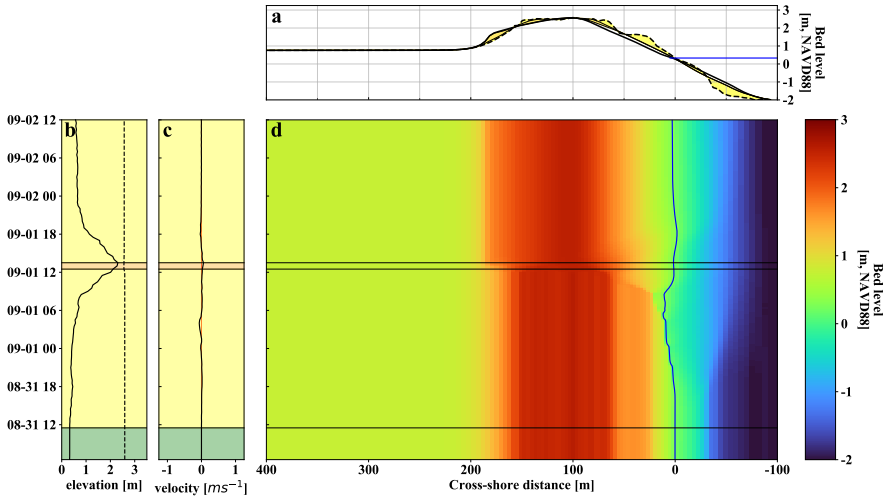

Figure 4.13: Cross-shore bed level evolution at T1 for the MC scenario under HG storm conditions. (a) Cross-shore profiles and MHW (blue line). The dashed and solid black lines are the initial and final bed levels, respectively. The yellow, orange, and red areas indicate profile change over the first collision, overwash, and inundation regimes, respectively. (b) Time-series of water level (solid) and z_{dc} elevations (dashed). (c) Time-series of cross-shore current velocity at the shoreline in (a). The green, yellow, orange, and red shaded areas in (b) and (c) indicate the swash, collision, overwash, and inundation regimes, respectively. (d) Time-stack of bed levels showing the profile's evolution with the MHW contour (blue line) for reference.

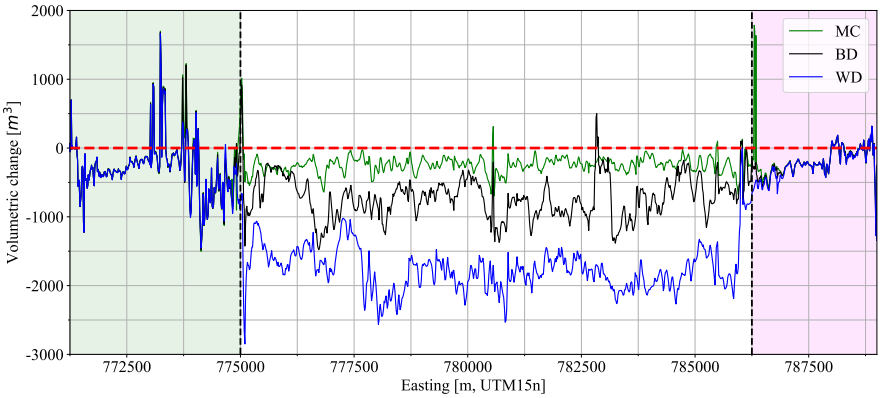

Figure 4.14: Net volumetric change over the 100 year storm event as a function of alongshore distance. The BD, MC, and WD restoration scenarios are shown as black, green, and blue lines, respectively. The green shared area indicates a protected stretch of the CH and the magenta area indicates an area affected by inlet processes.

those within the exposed central CH shoreline (Johnson et al., 2019). In these flanking areas, the storm-driven morphodynamics do not indicate distinct variability between restoration scenarios because there was no marsh creation here.

In contrast to CH's flanks, volumetric change in the central CH exhibited distinct morphological responses to the restoration scenarios. The MC restoration uniformly sustained relatively small ΔV_{sa}; volumetric decreases rarely exceed 500 m^3. On the other hand, volumetric sediment loss from the dunes in WD scenario ranges between 1500 m^3 and 2250 m^3. Volumetric sediment loss in BD falls between those of the MC and WD scenarios with most of the central shoreline exhibiting volumetric changes between -500 m^3 and -1000 m^3.

The net change in dune crest elevation along the CH shoreline, (Δz_{dc}) in Figure 4.15, is similar to that of the volumetric change. The CH's ends (green and magenta areas) show limited variability between scenarios, while the central area exhibits a discernible trend. Similar to the alongshore variation of the volumetric change, WD shows the greatest impact, followed by BD with MC being the least impacted. However, the relative differences between scenarios are smaller compared to the volumetric change. Throughout most of the central CH, z_{dc} in the MC scenario was lowered by at least 0.75 m. The WD scenario sustained large dune lowering with net changes on the order of a meter, while the BD restoration typically varied between -0.75 m and -1.0 m Δz_{dc}. In addition, there appears to be a trend in which the difference between the MC and WD scenarios increases along the eastern part of CH's shoreline. Dune crest lowering increases for the WD scenario and decreases for the MC, which conceivably indicates that marsh creation is more important in this part of the domain.

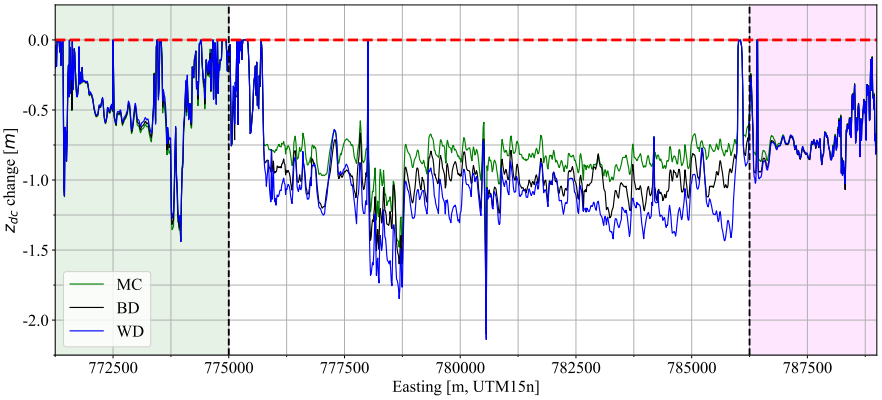

Figure 4.15: Net dune crest elevation change over the 100 year storm event as a function of alongshore distance. The BD, MC, and WD restoration scenarios are shown as black, green, and blue lines, respectively. The green shared area indicates a protected stretch of the CH and the magenta area indicates an area affected by inlet processes.

4.4 Discussion

4.4.1 Vegetation Stem Height in Dynamic Bed Roughness

van der Lugt et al. (2019) showed that incorporating the effects of erosion and deposition on vegetated land cover's surface roughness improves the accuracy of overwash sediment transport modeling. The bed shear stress term in XBeach's implementation of the momentum equations is, in the x direction, given as,

$$\tau_{bx} = c_f \rho u_E \sqrt{(1.16 u_{rms})^2 + u_E^2 + v_E^2} \tag{4.1}$$

where, τ_{bx} is the bed shear stress in the x- direction, c_f is the friction coefficient, ρ is the density of water, u_E is the Eulerian flow velocity in the x-direction, u_{rms} is the root-mean-square wave orbital velocity, and v_E is the Eulerian flow velocity in the y-direction. The friction coefficient is calculated from a depth-dependent, Manning's n based Chézy coefficient,

$$c_f = \frac{g n^2}{h^{1/3}} \tag{4.2}$$

where, g is the gravitational acceleration, n is the Manning's coefficient, and h is the local water depth.

Dynamic roughness accounts for the time variation of n associated with the local bed level changes, i.e., whether the initial land cover is covered with sand or removed through erosion. In the case of surface flows over barrier systems, the most important land cover is typically vegetation, so the dynamic roughness is expressed as a function of vegetation's morphological

parameters:

$$n(t) = \begin{cases} n_{sand} + (n_0 - n_{sand}) \cdot \min\left(\max\left(0, \frac{d_v + \Delta z(t)}{d_v}, 1\right)\right), & -d_v \leq \Delta z(t) < 0 \\ n_{sand} + (n_0 - n_{sand}) \cdot \min\left(\max\left(0, \frac{h_v - \Delta z(t)}{d_v}, 1\right)\right), & \Delta z(t) > 0 \end{cases} \tag{4.3}$$

where, $n(t)$ is the dynamic Manning's n, n_{sand} is the Manning's n for sand, n_0 is the initial Manning's n for the vegetated land cover, d_v and h_v are the vegetation's root depth and stem height, respectively. The values of h_v and d_v thus play an important role for momentum loss in high-energy flows which induce erosion and deposition.

In the case of beach and dune sand washover onto a backbarrier marsh platform, it is expected that landward sediment transport will be sensitive to the vegetation's stem height (h_v). To test this sensitivity, 6 simulations of 100 year storm conditions in the MC restoration scenario were performed for five different values of stem height, i.e., $h_v = 0.25$ m, 0.5 m, 0.75 m, 1.0 m, and 1.25 m. The values selected are all reasonable for backbarrier vegetation stem heights. In addition, a case with dynamic roughness turned off was also simulated, i.e., $dn/dt = 0$.

Pre- and post-storm profile change at T1, T2, and T3 are shown in Figure 4.16. The landward transport of washover sediment is reduced by 50 m to 100 m when dynamic roughness is not utilized compared to the other cases. In the static roughness case, the washover deposits forming during the overwash and inundation regimes do not affect the friction exerted by the backbarrier marsh on the flow despite their relatively thick (approximately 1 m) accumulation on top of the vegetation. The cases with dynamic friction show that decreasing h_v leads to a smooth increase in landward sediment transport. The difference between washover deposition's landward extent between smallest ($h_v = 0.25$ m) and largest ($h_v = 1.25$ m) stem heights varies 30 m and 50 m at transects T1, T2, and T3. This is intuitive because shorter vegetation is buried earlier during the storm; the friction is reduced and thus the shear at the bed increases which allows more erosion for a longer time.

Across the entire domain, h_v played a significant role in determining Δz_{dc} as can be seen in Figure 4.17. In the static roughness case, dune crest lowering generally does not exceed 60 cm, while the other simulations typically exhibit crest lowering in the range of 0.75 to 1.0 m. Similar to the washover deposition's landward extent, the smaller h_v allows for more dune crest lowering. Overall, the simulations indicate that overwash driven sediment transport is sensitive to the dynamic roughness formulation's vegetation input parameters.

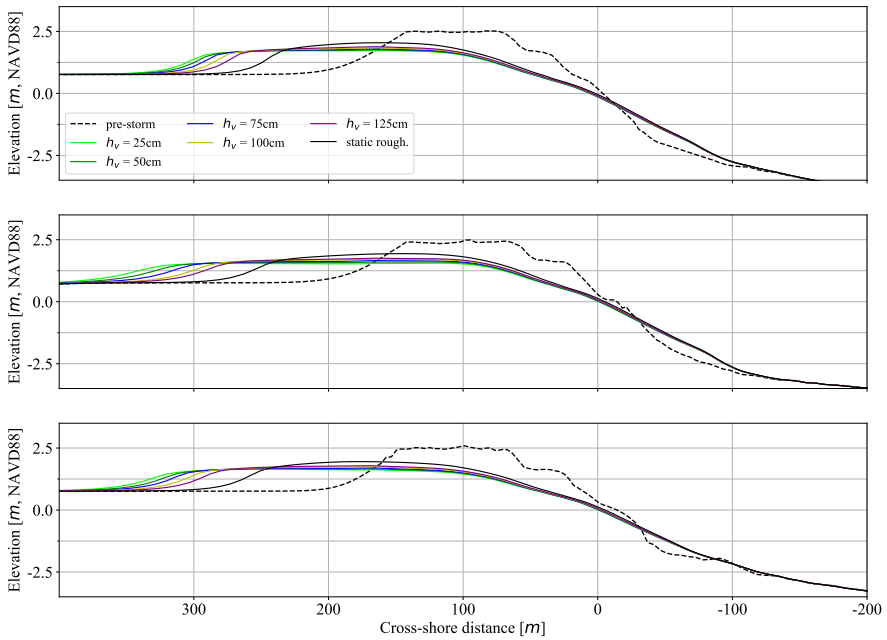

Figure 4.16: Pre- and post-storm profiles at the sample transects T1, T2, and T3 for the 100 year storm event. The initial profile is shown as a dashed line and the post-storm profiles are shown as solid lines. The static friction case is shown as black line, while the results from the sensitivity tests are shown in different colors.

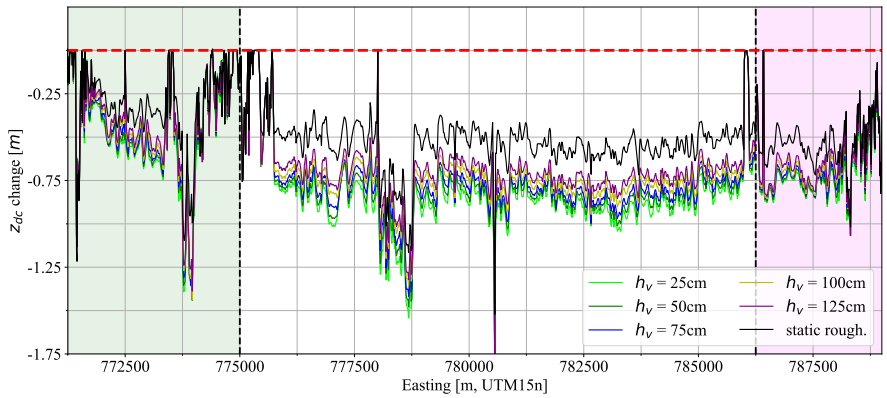

Figure 4.17: Alongshore distribution of dune crest lowering due to the 100 year storm event. The initial profile is shown as a dashed line and the post-storm profiles are shown as solid lines. The static friction case is shown as black line, while the results from the sensitivity tests are shown in different colors.

4.4.2 Simultaneous Backbarrier Marsh Creation with Beach and Dune Restoration

The sediment transport results from the 100-year storm conditions clearly demonstrate the benefit of restoring/creating backbarrier marshes in barrier systems that are likely to experience inundation and/or overwash regimes during a storm. Figures 4.14 and 4.15 show that the presence of a backbarrier marshes systematically reduces storm impacts. With regard to Δz_{dc}, the benefits of reducing dune lowering across the domain are obvious as a higher post-storm dune crest is less vulnerable during subsequent impacts. Barrier island restoration projects typically set a specific barrier elevation at the end of its design lifetime. If, in the project design, it is assumed that overwash and inundation events are probable, it can be expected that the backbarrier wetlands will help mitigate dune crest lowering during those events. The target elevation at the end of its design lifetime can then be accomplished with a lower initial beach and dune lift (i.e., with less dredged sediment). In addition, the design lifetime of the restoration could be extended (e.g., from 20 years to 25 years) adding value to the cost of the project's construction.

With regard to volumetric change, ΔV_{sa} is less negative in scenario MC and Figure 4.7 indicates that washover sediment is deposited at a higher elevation relative to the pre-storm dune. This situation is advantageous to achieve long-term resilience of restored barrier against storm-induced erosion. Since washover deposition is kept at a higher elevation in the tidal frame, i.e., higher relative to MSL, eroded sediment deposits will readily be available for natural and anthropogenic post-storm recovery processes. The subaerial sediment can then be used to re-build the target dune elevation or can serve as a substrate for aeolian recovery (Houser et al., 2015).

Overall, the backbarrier marsh, by reducing ΔV_{sa}, buffers the export of sediment from the subaerial barrier understood as a cell in a sediment budget context. In terms of sediment budget, shoreline erosion occurs due to sediment volume losses from the subaerial barrier either through offshore, alongshore, or overwash transports. Over time, the reduction of sediment export from the subaerial barrier will presumably be manifested as a reduction in the rate of shoreline erosion. Most beach and dune restoration projects also have the goal of offsetting or mitigating shoreline erosion. Thus, the reduction in subaerial sediment loss during overwash and inundation events is facilitated by backbarrier marsh creation and can therefore serve as a feasible alternative in counteracting the shoreline erosion.

Creating a permanent vegetation cover is another aspect of both beach/dune and marsh restoration. This serves many goals, e.g., ecological health, stability of newly placed sediment, and promoting organic accretion in the case of marshes. The marked decrease in landward transport of washover with increasing vegetation height in Figure 4.16 adds an additional benefit to the creation of backbarrier marshes and establishment of vegetation. Further, the effect of stem height in modulating roughness also adds some explanatory evidence for the role vegetation plays in trapping sediment during overwash and inundation regimes. When sediment is retained in the vicinity of beach and dune, this sediment is less likely to be exported from the system entirely in the long-term. Because stem height is dependent on vegetation species, planting tall vegetation species over the backbarriers should be considered.

4.5 Conclusions

A physics-based sediment transport-morphodynamic model was used to simulate the event-scale morphodynamic changes under real and synthetic tropical cyclone conditions at the Caminada Headlands, Louisiana after its recent large-scale beach and dune restoration. Two tropical cyclone conditions were simulated: (1) forcing identical to those of Hurricane Gustav (2008); (2) storm conditions for 100-year return period along Hurricane Gustav's track. In addition to the actual post-restoration scenario, two hypothetical land cover and topography of backbarrier were considered to examine their effect on post-storm impacts. These alternative scenarios aims at assessing the impact of the backbarrier's land cover and elevation on erosion. The first incorporated a fully restored marsh and the second considers a marsh which was fully deteriorated and converted to open-water.

The results indicate that the Caminada Headlands Beach and Dune Restoration could sustain the impact of a Hurricane Gustav-like storm, regardless of backbarrier restoration, with some offshore sediment transport and minimal overwashing. The morphodynamics of the 100-year storm conditions, which produced overwash (approximately 4 hours) and inundation regimes (approximately 4 hours), show considerable differences depending on the restoration scenario. In general, the presence of a restored backbarrier marsh reduced the subaerial volume loss and dune crest lowering compared to those in un-restored and open-water scenarios. These results suggest that incorporating backbarrier marsh creation into beach and dune restoration projects at low-lying barrier which experience frequent overwash may increase the barrier's resilience to storm impacts.

The following summarized the main findings.

1. The simultaneous creation of a backbarrier marsh with a beach and dune restoration produces the optimal solution for mitigating the storm impacts if overwashing and inundation are expected. Backbarrier marsh increases post-storm dune crest elevation and post-storm subaerial volume retention. The increased elevation of the backbarrier marsh platform generated thinner washover deposits because enhanced bed friction due to the vegetative land cover limited landward sediment transport.

2. During the inundation regime, sediment transport is sensitive to vegetation stem height in the backbarrier wetland. Taller vegetation generally exerts drag on the flow for a longer duration as the vegetation is gradually buried into washover deposits. Whereas shorter vegetation is buried quicker allowing a larger shear at the bed and thus landward transport. Assuming that all other ecological considerations are equal, planting taller vegetation species in marshes along the overwash prone barriers is recommended.

3. Hurricane Gustav-like forcing at the post-restoration Caminada Headlands does not produce significant morphological change. This is likely due to a short period of overwash regime forcing and the lack of inundation. Collision regime forcing transported a small amount of sediment offshore. In this regard, it is conjectured that irrespective of the backbarrier land cover and elevation, increasing the crest elevation of a barrier is effective only if the overwash regime is absent or briefly occurs.

CHAPTER 5
CONCLUSIONS

The objective of this dissertation was to investigate the morphodynamics of the Caminada Headlands (CH), a vulnerable low-lying barrier system, driven by tropical cyclone (TC) forcing. To accomplish this, in summary, the CH's morphodynamics were first analyzed at the decadal time scale using a 15 year time series of LIDAR surveys. The analysis of shoreline migration and dune morphology change placed the event-scale barrier morphodynamics within context and prepared the ground for detailed physics-based numerical modeling and analysis of Hurricane Gustav's (2008) impact to the CH. A modeling system, consisting of a large-scale hydrodynamic-wave model and a local-scale sediment transport-morphodynamic model that are one-way coupled, was developed to hindcast the impact of Hurricane Gustav. The hindcast simulation's hydrodynamics were verified with water level observations from multiple stations and nearshore surface waves from rapidly-deployed pressure transducers; while the model's morphodynamics were verified with a pair of pre-/post-storm LIDAR surveys.

The hindcast simulation's sediment transport results revealed that alongshore variability within the CH's backbarrier environment, specifically surface roughness and topography related to wetland disintegration, can explain differences in impacts to the CH's beach and dunes despite similarities in forcing and pre-storm dune topography. Guided by these findings, the verified modeling system was further employed in numerical experiments that forced the CH's recent beach and dune restoration with Hurricane Gustav-like and 100 year return period storm conditions. The Hurricane Gustav-like numerical experiments indicated that a TC of Hurricane Gustav's strength would not significantly impact the post-restoration CH, as its storm surge and waves did not generate significant overwash. The numerical experiment forced with 100 year storm conditions showed extensive washover of the CH's restoration and exhibited a variable response depending on the restoration's backbarrier marsh component, which was varied between full marsh creation, no marsh creation and open water. The evidence and conclusions yielded by the dissertation's research recommends that backbarrier marsh creation within barrier systems vulnerable to overwash will enhance their resiliency to future storm impacts.

The LIDAR analyses in Chapter 2, besides generating conclusions of their own, also provided context for further investigation. To begin, raw LIDAR point clouds for 9 aerial surveys between 1998 and 2013 were acquired, ground-truthed with an independent terrestrial survey, classified and separated into bare-earth data, and interpolated to digital terrain models (DTM) on a

common grid (see Appendix A). The DTMs were analyzed with cross-shore transects spaced every 10 m as well as integrated to provide volumetric change statistics. The CH's decadal coastal morphodynamics exhibited distinct zonation. The central zone's shoreline eroded at a rate of -17.8 m yr^{-1}, while the western and eastern zones' shorelines migrated at rates of -4.4 m yr^{-1} and -6.9 m yr^{-1}, respectively. The zonation is interpreted to reflect the structural defenses in the western zone, the presence of an alongshore sediment transport gradient within the central zone (Georgiou et al., 2005), and aggradational spit/inlet processes in the eastern zone.

Eight named TCs made landfall with 100 km of the CH during this period, including Hurricanes Isidor (2002), Katrina (2004), Gustav (2008), and Isaac (2012). The majority of the CH sustained alongshore averaged shoreline displacements between -30 m and -60 m and dune crest lowering between 20 cm and 50 cm as a result of the TC impacts, followed by recovery periods that typically regained the lost volume and elevation. However, due to alongshore variability in dune morphology, sediment availability and transport gradients, the CH recovered at different rates and, as a result, were overwashed during the post-storm recover periods at different rates depending on zone. The central zone experiencing an average rate of 26.6 overwash occurrences per year in post-TC impact periods, while the western and easter zones exhibited rates of 2.8 and 8.6 occurrence per year, respectfully. The CH's alongshore variability in decadal morphodynamics was therefore also reflected at the shorter time scales of TC impact/recovery cycles.

A conceptual model for the evolution of frequently overwash barriers (FOB model) was applied to the CH (Matias et al., 2008). The model consists of 4 stages: (1) an initial quiescent period where swash erosion/deposition and aeolian transport dominate; (2) a storm impact which produces massive morphological change; (3) a period of frequent overwashing, more washover transport, and potential conversion to a washover plain; (4) a period of wanning overwash events. Applied to the CH, the western zone sustains storm impacts, but quickly returns to stage (1) without suffering a period of frequent overwashing. The eastern zone completes the entire cycle following a storm impact, presumably due to a plentiful supply of sediment eroding from the central zone and accumulating updrift of Caminada Pass. However, due to a negative sediment budget, the central zone does not return to a recovery period, i.e., stage (1), following Hurricane Gustav's impact. This conclusion is supported by the net morphological change of the central zone's alongshore averaged profile, i.e., change in the shape of the beach and dunes from the beginning to the end of the study period, which has shifted from a continuous foredune to a flatter washover plain; while, on the other hand, the western and eastern zones have similar

profile morphologies, but with less elevated foredunes.

Over the study period, despite the multiple TC impacts and shifts in morphology, the CH's subaerial volume is approximately conserved; however, the dunes were generally widened and flattened. It has been hypothesized that the recovery period for subaerial volume at the CH is approximately 10 years (Ritchie and Penland, 1988) and this is generally supported by the LIDAR analyses, except that the period may be revised downward to 5 - 7 years. However, this is not the case for dune elevation, which was not recovering at a sustainable rate. Over the study period, the dune crest change rate was, on average, -2.0 cm yr^{-1}, while the rate of sea-level rise (SLR) was 3.49 mm yr^{-1}. This was an unsustainable situation, leading the CH into a new metastable equilibrium, as opposed to the storm impact/full-recovery cycle which previously characterized its morphodynamics.

Interestingly, within the central zone an inverse correlation ($r^2 = 0.67$) was found between the net shoreline erosion rate and land-to-water (LWR) of the proximal backbarrier wetlands. Shorelines seaward of backbarrier environments with areal averaged LWR values less than 40% exhibited erosion rates of -16 to -20 m yr^{-1}, while other shoreline stretches with proximal backbarrier LWR values above 50% had erosion rates of less than -14 m yr^{-1}. A less determined correlation ($r^2 = 0.48$) was found between LWR and dune crest elevation as well. Given the intimate linkage between the subaerial beach/dunes and the backbarrier during overwash events, and the importance of TC impacts for driving shoreline morphodynamics, it was conjectured that a relationship between these two environments exists which occurs during the process of washover sediment transport. To address this conjecture, a high-resolution sediment transport-morphodynamic model of the CH was developed to hindcast the impact of Hurricane Gustav (2008).

In Chapter 3, the sediment transport and morphodynamic processes and their relationships with backbarrier land cover and topography, which were inferred from the LIDAR surveys of TC impacts, are investigated with a physics-based numerical model. A fully-coupled basin- and regional-scale hydrodynamic-wave model (Delft3D/SWAN) was developed to hindcast the waves and water levels generated by Hurricane Gustav within the Gulf of Mexico (GoM). The model is forced with astronomic tides and meteorological fields produced by blending a tropical cyclone model (Holland et al., 2010) and background North American Regional Re-analysis program winds and atmospheric pressure distributions. Water levels observed at stations 292 and 164 of LA's Coastwide Reference Monitoring System (CRMS) network, the National Oceanographic and Atmospheric Administration's (NOAA) tidal gauge at Grand Isle (GI) and pressure

transducer 8, 9, and 11 from Kennedy et al. (2010)'s pre-storm deployment (AK8, AK9, and AK11, respectively) were utilized to verify the modeling system's hydrodynamics and surface wave fields. The computed water levels have root-mean-square-error (RMSE) values of 0.19 m, 0.30 m, 0.31 m, 0.16 m, 0.21 m, and 0.25 m for observation stations CRMS0292, CRMS0164, GI, AK8, AK9, and AK11, respectively. Surface waves, expressed as significant wave height, were also observed at AK8, AK9, and AK11 and yielded RMSE values of 0.61 m, 0.34 m, and 0.14 m, respectfully.

The large-scale hydrodynamic-wave model drove a local-scale sediment transport-morphological numerical model (XBeach) by forcing the boundary with water levels and directional wave spectra. The internal hydrodynamics of the local-scale model were also compared to observations from AK9, as it was within this model's domain, yielding RMSE values of 0.22 m and 0.41 m for water level and zero-moment wave height, respectively. Verification of the local-scale model's sediment transport and morphodynamics were accomplished with a set of pre- and post-storm LIDAR surveys. The LIDAR points were averaged within the model's computational grid cells and compared with the change between the model's input (pre-storm) and output (post-storm) bed level. Domain-wide, the morphodynamic model exhibited a Brier skill score of 0.30, a bias of 0.18 m, and a RMSE of 0.32 m. Within subregions defined for detailed analysis, i.e., Bay Champagne (BC) and Bayou Thunder (BT), the model had Brier skill scores of 0.82 and 0.53, respectively, with RMSE values of 0.15 m and 0.24 m, respectively; the subregions are relatively free from the influence of structural protection's in the CH's west and inlet processes in the east. The Brier skill scores are reasonable for the entire domain and the BT subregion, and excellent for the BC subregion (van Rijn et al., 2007).

Biases in the model output are uniformly positive across the domain and it was hypothesized that this was due to excess sediment supply in the modeled CH's nearshore compared to reality. The CH is a sediment starved system where the underlying marsh and clay layers outcrop within the beach and dunes due to storm-driven erosion that completely removes the upper veneer of mobile sediment. This situation was modeled by setting a non-erodible layer at the mean high water (MHW) contour to model the contact between the mobile sand layer and the underlying strata. A hindcast of Hurricane Gustav was run with this modification and it reduced the bias in post-storm dune volume per unit width by 28.3% and 9.7% for the central zone and entire domain, respectfully.

The sediment transport-morphodynamic model allowed for observation and analysis of Hurricane Gustav's impact regimes, and their evolution over the event's duration, at high level of

detail where direct observation is prohibitively difficult. A majority of the dune lowering and, too a lesser extent, sediment transport occurs during an initial short-duration overwash regime (2 hours) as beach and dune sediment is eroded and transported onto the backbarrier. This is followed by a more prolonged inundation regime (6 to 7 hours), where landward transport of sediment eroded from a wider section of the subaerial barrier occurs.

The washover deposition at the BT and BC subregions is compared to an additional area, entitled the "solid marsh" (SM) subregion, so-called because it exhibits a relatively continous backbarrier marsh with uniform vegetated land cover. The three subregions are situated on a conceptual scale representing the disintegration of marshes into open water, with SM representing a health continous marsh, BT representing an intermediate state and BC representing the complete conversion of wetlands into open water. Analysis of sediment transport was accomplished at cross-shore transect by computing the centroids of the pre-storm subaerial volume (sediment above MHW) and the post-storm deposition. The washover displacement's horizontal component was inversely correlated with both the proximal backbarrier's average Manning's n and elevation with coefficients of determination (r^2) of 0.70 and 0.49, respectively, and p-values $<<$ 0.001 in both relationships. Further, the vertical displacement of washover sediment was positively correlated with average Manning's n and elevation, i.e. the greater the backbarrier's surface roughness and higher its topographic elevation, the higher the post-storm sediment volume would be deposited in the tidal frame, with r^2-values of 0.70 and 0.79, respectively, and p-values $<<$ 0.001 in both relationships. These parameterizations served well to characterize the conceptual scale of wetland health, as they exhibited approximately continous variation across the SM, BT, and BC subregions representing the high, middle, and low portions of the parameters' ranges.

Chapter 4 attempts to forecast TC impacts to the CH after the large-scale restoration of its beach and dunes using the modeling system verified in Chapter 3. The actual "as-built" beach and dune restoration (completed in 2016) is modified in the model to incorporate a hypothetical marsh creation component. A scenario is also developed that completely removes the backbarrier marsh, representing a situation where the wetland has completely deteriorated into open water. The post-restoration simulations were forced with the hindcast Hurricane Gustav conditions and a 100 year return period TC. The 100 year return period forcing was synthesized based on statistical relationships drawn from the nearby NOAA GI tidal gauge and a Wave Information Studies station, resulting in an peak water level scaled by a factor of 1.57 and a peak significant wave height scaled by 1.39, compared to Hurricane Gustav.

It was found that a Hurricane Gustav-like impact to the post-restoration CH would not cause significant morphological change, regardless of the backbarrier marsh, as the restored dunes were not inundated or extensively overwashed. This, however, assumes that the impact occurred within a relatively shore time period after the restoration. Settlement of the placed sediment due to self-weight consolidation and compaction of the underlying strata significantly reduces the barrier overall elevation through time (Jafari et al., 2019). If the Gustav-like storm conditions impacted the post-restoration CH after sufficient settlement had occurred to allow for extensive overwash and inundation, the protection afforded by the renourished dune system may not have been as robust. The 100 year return period TC, on the other hand, generated considerable overwash (4 hours) and inundation regime (4 hours) forcing. As a result, landward transport of washover occurred across the CH resulting in subaerial volume loss and dune crest lowering which was strongly affected by the backbarrier marsh or lack thereof. Subaerial volumetric losses per unit width, with and without a marsh creation component in place, rarely exceeded 50 m^3 m^{-1}, while in the case of open water backing the dunes, volumetric losses typically ranged between 150 m^3 m^{-1} and 225 m^3 m^{-1}. A similar pattern occurred with dune crest lowering, with changes between 0.50 m of 0.75 m for the marsh creation scenario, 0.75 m and 1.15 m without the marsh creation, and 1.00 m and 1.25 m for the scenario with open water backing the dunes. When the displacements of eroded pre-storm volume are analyzed into vertical and horizontal components, the created marsh component allowed for increased landward displacement of sediment, but the washover is deposited at a higher elevation compared to the other post-restoration scenarios.

Considering the main finding from Chapters 2, 3, and 4, it can be concluded that backbarrier wetlands play an important roll in buffering low-lying barriers from morphological change during overwash and inundation regime events. At the decadal time scale, it was observed that the conversion of solid marsh to open water (as represented by the LWR) is significantly correlated to shoreline erosion and dune crest elevation, suggesting that restoration/creation of backbarrier marshes could help attenuate shoreline erosion and dune lowering. At the event time scale, based on a hindcast simulation of Hurricane Gustav's impact, land cover-based surface roughness and topography, as a parameterization of backbarrier wetland health, were found to significantly influence washover sediment transport. The greater the average surface roughness and backbarrier elevation, which may serve as proxies for wetland health, the smaller the horizontal displacement of washover sediment and the less elevation the sediment losses once redeposited. Finally, the presence of a backbarrier marsh creation component, in conjunction with a beach and dune restoration of the CH, was seen to mitigate the erosion of subaerial dune volume and dune crest

lowering during a 100 year return period storm event. On the basis of these results, the simultaneous creation of backbarrier wetlands with beach and dune restorations, or as standalone projects, appears to be an effective method for enhancing the resiliency of barrier systems which are frequently overwashed.

If restoration budgets are constrained and project priority must be determined, then the distribution of pre-restoration coastal morphology and backbarrier wetland health should be utilized when evaluating cost-benefit ratios. For instance, if the majority of a project site's backbarrier wetlands are severely deteriorated, then marsh creation should be prioritized as an inundation regime impact to renourished dunes, without an intact backbarrier marsh platform, would likely generate significant elevation and subaerial volume loss, reducing the benefit of the renourishment. With an intact backbarrier marsh created first, then vulnerable beaches and dunes could be renourished with a greater probability that future inundation regime impacts would result in less severe losses, increasing the renourishment's benefit. On the other hand, if the backbarrier wetlands are generally not deteriorated, or at risk of disintegration, then renourishment of the beach and dunes should be prioritized to protect the barrier from inundation regime impacts due to lower probability storm events. In the scenario where both the beach/dunes and backbarrier marsh are seriously impaired, and the barrier is at risk of disintegration, then the prudent action would be to add sandy sediment to the system through a beach and dune renourish and forestall the complete disappearance of the barrier.

Future work related to this dissertation should follow two related trajectories. The first pertains to field work. Topographic and vegetation monitoring of the CH could provide the context for understanding the evolution of its restoration due to storm events in the future. If this monitoring was coupled with rapid-response efforts, following a TC impact, then progress in the modeling of TC driven sediment transport could be made based on the data collection. Further field investigations into the distribution of the CH's mobile surficial sand layer are necessary if the accurate modeling of this situation is to be accomplished. On the other hand, the modeling system verified in Chapter 3, and utilized in Chapter 4, could facilitate further numerical experimentation. Conducting more simulations which vary the storm conditions, possibly representing less energetic events or different storm tracks, and restoration scenarios would increase the scope and robustness of recommendations as to barrier restoration design. Additionally, efforts should be made to perform long-term modeling of the CH using the verified modeling system, coupled with wind-driven aeolian sediment transport, subsidence, and sediment compaction/consolidation process models, as enhancing coastal resiliency necessarily requires

long-term estimates of morphological change. The physics-based modeling of a barrier system's long-term evolution, while challenging both computationally and in terms of uncertainty, would be a great technological advancement.

APPENDIX A

SUPPLEMENTAL MATERIAL FOR CHAPTER 2

A.1 Work flow

In coastal LA, the conditions of low-relief and low-elevation topography, subsidence-driven vertical land movement (VLM) and accelerated coastal evolution present unique challenges to morphological analyses. To address these challenges, the lidar surveys were processed from raw data a whole to generate quality-controlled, comparable digital terrain models (DTMs) of the subaerial beach, backshore, and foredune. Figure A.1 presents a flow chart that illustrates the step-by-step methods for processing the raw lidar point clouds.

A brief walk-through of Figure A.1 is provided here with more detailed descriptions available in the following sections. The initial step was the acquisition of airborne lidar survey data sets which exhausted publicly available data resources (to the best of the authors' knowledge). An extensive terrestrial real-time kinematic global positioning system (RTK-GPS) survey was filtered to extract geodetically stable ground-control points (GCPs) that were contained within the combined lidar data's coverage (see Figure A.2 for aerial photographic depiction of GCPs). Lidar points were compared with the GCPs to calculate ground-truthing statistics (see Table A.1). The lidar surveys were shifted individually based on the median difference between the lidar data and the GCPs (see Figure A.3 for an illustration of the correction's results).

Corrected lidar data which were classified as *ground* points were extracted into a bare-earth lidar data set. The surveys which were were not initially classified were processed with an surface point detection algorithm. The lidar points classified as *ground* as opposed to *non-ground* were extracted and added to the bare-earth data set. The bare-earth lidar were analyzed for elevation range and point density at resolutions 0.5, 1, 2, 5, and 10 m. The lidar data were gridded at 0.5 $\times$ 0.5 m resolution using a smoothing spline approximation method. The DTMs were masked to remove cells below mean high water (MHW) and not contiguous with the main barrier landform. The extracted subaerial barrier DTMs were analyzed with cross-shore transects to determine the dune crest, dune toe, and shoreline positions. Dune volume was calculated by integrating the DTMs above a threshold defined as than mean dune toe elevation. Finally, the morphological parameters and dune volumes, that are functions of alongshore position and time, were assembled in a database that allowed for the investigation of spatial and temporal trends in the study site's

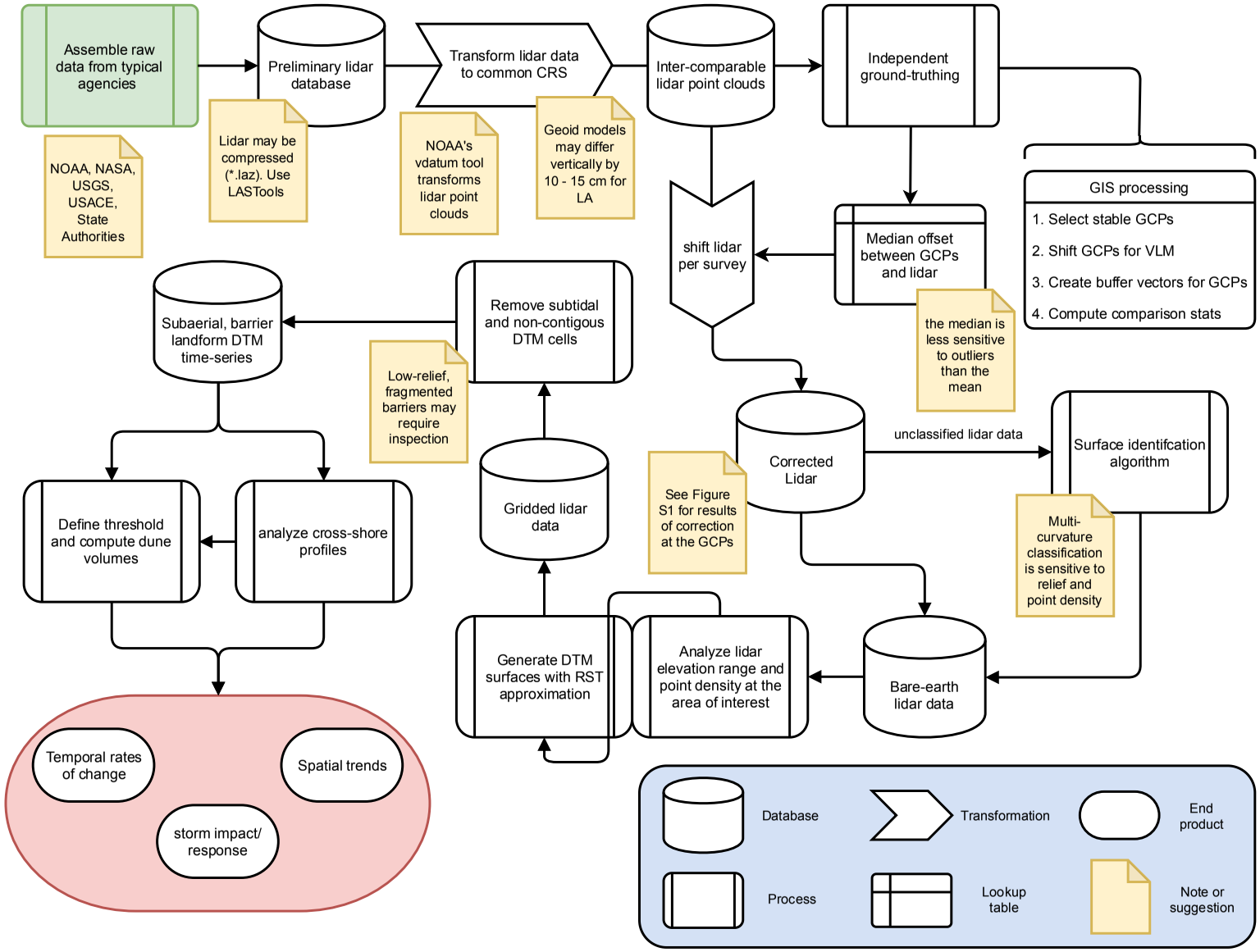

Figure A.1: Flowchart for pre-processing and analyzing lidar data.

coastal geomorphology.

A.2 Lidar data pre-processing

The first survey was flown October 9th, 1998 and the final on March 8th, 2013. Three surveys were collected directly following a storm impact: TS Isidore (2002); Hurricane Gustav (2008); and Hurricane Isaac (2012). The effects of multiple other TCs were also captured (see Table 2.1 for storm details). The lidar data were collected by different agencies and acquired with disparate survey equipment. The surveys were conducted by four agencies: the United States Geological Survey (USGS), the National Oceanographic and Atmospheric Administration (NOAA), the National Aeronautic and Space Agency (NASA), and the United States Army Corps of Engineers (USACE) through their Joint Airborne Lidar Bathymetry Technical Center of Expertise (JALBTCX). The data sets' signal-to-noise ratio, point classification scheme, and geodetic coordinate reference system also varied significantly between themselves. The data were archived along with the metadata (vintage, nominal accuracy, coordinate reference system, etc.) in uncompressed *.las format (see Figure 2.2 for select metadata). The survey metadata is provided in Table 2.2.

The data were pre-processed generally following the methodology in Mitasova et al. (2009) to achieve comparable DTMs and verify quality control. The National Oceanographic and Atmospheric Administration's (NOAA) VDatum 3.8 tool (`https://vdatum.noaa.gov`) was used for transformation and conversion of the uncompressed lidar data to a common coordinate reference system (CRS). Using NOAA's VDatum tool, the lidar were transformed from their original CRS to the Geodetic Reference System of 1980 (GRS80), referenced to the North American Datum 1983 (NAD83) and the North American Vertical Datum 1988 (NAVD88) using geoid model 2012b (GEOID12B) and projected to the Universal Transverse Mercator zone 15N (UTM15N). The maximum uncertainties associated with CRS transformations in eastern Louisiana amount to 17.1 cm. The transformations made herein are not as large as they do not included sea-level referenced datums and were on the order of 10 cm. Transformations between geoid models (e.g. GEOID06 to GEOID12B) were significant and yielded elevation changes on the order of 5 cm at some points.

The 1998, 2001, 2002, and 2008b lidar were not disseminated as classified points (i.e. identified as ground, water, low vegetation, etc.) following the LAS open data format specification (The American Society for Photogrammetry & Remote Sensing, 2013). However, the 2006, 2008a, 2010, 2012, and 2013 surveys were available as classified lidar. Multi-curvature classifi-

cation (MCC), a ground surface identification algorithm implemented in GRASS GIS (Blumentrath, 2015), was used to identify the ground points of the unclassified lidar (Evans and Hudak, 2007; Tinkham et al., 2011). The MCC parameters require tuning as the algorithm is sensitive to point density, beam angle, and topographic relief. Classification results from a sensitivity analysis were visually compared with aerial orthophoto imagery acquired close in time to the surveys. The selected MCC parameters can be found in Table A.7, and the reader is referred to Mitasova et al. (2005) and Evans and Hudak (2007) for details on the MCC. Only ground points were used for bare-earth DTM generation.

Preliminary inspection of the lidar data revealed that some surveys apparently contained significant biases. In certain situations, the bias was comparable in magnitude to the relevant morphodynamics, e.g. storm-induced dune crest elevation change. For example, as determined by the ground-truthing, the bias of the 2008a and 2008b lidar surveys are -16.3 cm and 46.7 cm, respectively (see Table A.1). These lidar surveys recorded Hurricane Gustav's impact which, after removing the biases to yield *best estimates*, produced an average dune crest elevation change of -29.3 cm within the central zone (see Table 2.4). In this case, not only are the biases comparable in magnitude to the morphodynamics, but retaining them in the calculated elevation change would lead to the conclusion that the central zone's dune crest increased in elevation. Therefore, the lidar surveys were independently ground-truthed.

To ground-truth the lidar, the raw point clouds were compared to a stable geodetic reference surface by means of a real-time kinematic global positioning system (RTK-GPS) survey. The geodetic reference surface was Chevron Rd. in Port Fourchon adjacent the Chevron Pipe Line installation. Figure A.2 shows the GCPs in relation to Chevron Rd.. The RTK-GPS survey was completed on November 11^{th}, 2010 during the CH Beach and Dune Restoration Project's design. Forty-two RTK-GPS points were selected as GCPs. These points were selected as they overlapped with every lidar surveys' coverage and occupied the "center line of asphalt", referring to Chevron Rd., as denoted by the surveyor. Chevron Rd. is located near the shoreline within Port Fourchon (see Figure 2.1 for the location of the GCPs relative to the study area).

The CH is known to be affected by regional subsidence. Subsidence would act to lower the elevation of Chevron Rd. through time which would positively bias comparisons of the GCPs to lidar surveys conducted prior to 2010. A National Geodetic Service's Continuously Operating Reference Station (CORS), located at the Grand Isle (GI) NOAA station (see Figure 2.1 for its location), has recorded a VLM rate of -5.6 mm yr^{-1}. Since the Chevron Pipe Line and the CORS site are in close proximity and overlie similar stratigraphy, it is reasonable to assume

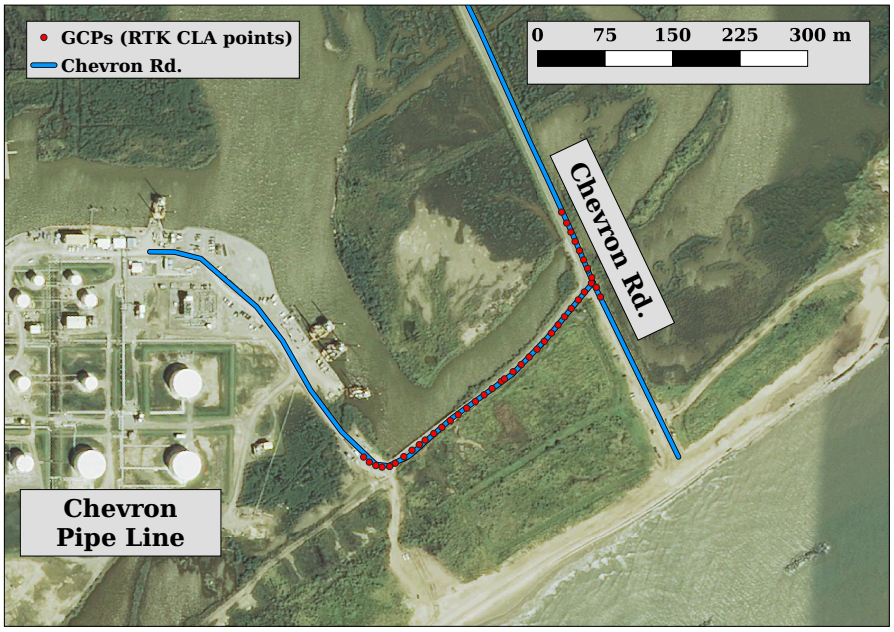

Figure A.2: Location of GCPs in relation to Chevron Rd., Port Fourchon, LA.

they are affected by similar subsidence rates. To correct for subsidence, the GCPs were linearly interpolated to the lidar acquisition dates with the observed VLM rate of -5.6 mm yr^{-1}. Lidar returns within a 0.5 m horizontal radius of a GCP were then averaged to represent the lidar derived elevation, z_{lidar}, for each lidar survey.

The difference between z_{lidar} and the subsidence-corrected RTK-GPS elevation was computed for each lidar survey. The median of the differences was used to represent the systematic error (offset) of a particular lidar survey. The entire uncorrected lidar point clouds were uniformly shifted by their corresponding offset. Statistics on the ground-truthing can be found in Table A.1. The corrected and uncorrected z_{lidar} values along Chevron Rd. are shown with the GCP elevations in Figure A.3. The smaller vertical discrepancies in the bottom panel of Figure A.3 suggest that the correction performed reasonably well.

A.3 DTM generation

The corrected lidar point clouds were analyzed to determine optimum DTM resolution and generation method. Per cell elevation range and points-per-cell were calculated at 0.5, 1, 2, 5, and 10 m resolutions. For resolutions of 2 m or less, all surveys except 2012 had a mean per cell elevation range less than the nominal accuracy of the survey. A resolution of 0.5 m was selected for DTM generation to accurately resolve the shoreline and other small-scale features. At this resolution, mean points-per-cell is near 1 for all surveys except 2006 and interpolation is required to ensure data coverage for all DTM cells. Regularized spline with tension and smoothing (RST),

Table A.1: Statistics of lidar survey validation. The GCPs column shows the number of GCPs that contained lidar data within a 0.5 m radius of the GCP. Mean, median, standard deviation (Std.), and root-mean-square-error (RMSE) are calculated between $\overline{z}_{lidar}$ and the GCP's elevation.

Survey	GCPs (n)	Mean (cm)	Median (cm)	Std. (cm)	RMSE (cm)
1998	14	-1.8	-2.3	8.2	8.1
2001	37	7.7	8.2	5.7	9.6
2002	19	2.8	3.8	7.2	7.6
2006	42	-27.5	-27.8	3.6	27.8
2008a	29	-16.3	-15.6	11.7	20.0
2008b	37	46.7	47.0	5.5	47.0
2010	42	-4.5	-4.5	1.6	4.7
2012	42	32.4	32.4	1.2	32.4
2013	40	-2.8	-3.2	3.0	4.1

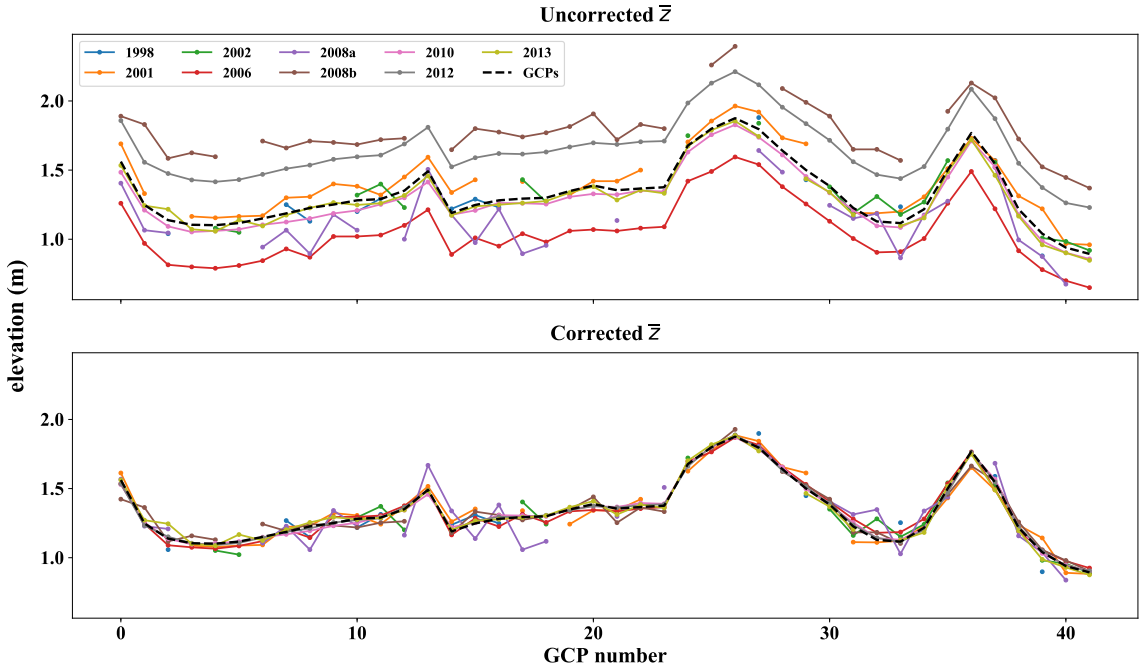

Figure A.3: Comparison of GCP elevations with mean lidar elevations at each GCP along Chevron Rd. The lidar surveys are represented by solid lines, where the values of $\overline{z}_{lidar}$ are indicated with markers, and the black dashed line is the RTK-GPS derived elevation of Chevron Rd. (top) Uncorrected lidar. (bottom) Lidar elevations after shifting by the correction. All elevations are referenced to NAVD88.

an approximation function which minimizes the data's deviation from an approximated surface, was used to interpolate the DTMs (Mitasova et al., 2005).

Cross-validation optimization was performed for each lidar survey on a limited portion of the study area to tune the RST function (Neteler and Mitasova, 2008). Cross-validation iterates over individual lidar data points, approximating a surface without the point and then computing the residual between the removed point and surface. The tension parameter, which controls the weight of individual points, was varied over the values 500, 1000, 1200, and 2000. The tension which minimized the root-mean-square error (RMSE) of the cross-validation results was used in the RST approximation. However, the RST was found not to be sensitive to tension for the study site's topography. The elevation range, point density, and cross-validation RMSE for the lidar surveys can be found in Table A.8.

Finally, the removal of spurious and low-quality lidar was necessary to produce comparable DTMs. Turbid waters in the surfzone and back barrier wetlands within the CH render the ground classification of lidar in these locations unreliable. The lidar beam is partly reflected by the water column and thus incorrectly estimates the terrain's elevation. Therefore, DTM cells below MHW and not contiguous with the main coastal barrier landform were masked out and the supratidal beach, backshore, and foredune were extracted for morphometric analysis. MHW elevations for the lidar acquisition dates were taken from the GI station. The final product of the pre-processing is a time series of DTMs containing the CH's subaerial coastal morphology from 1998 to 2013.

A.4 Morphometric analysis

The DTMs were analyzed for five morphological parameters: shoreline position (x_{sl}), dune crest position and elevation (x_{dc} and z_{dc}, respectively) and dune toe position and elevation (x_{dt} and z_{dt}, respectively). The horizontal parameters were measured relative to a baseline that was generated by smoothing and simplifying the 1998 MHW contour. The vertical features (z_{dc} and z_{dt}) are referenced to NAVD88. The parameters were extracted from cross-shore transects of the DTMs spaced every 10 m in the alongshore direction. The transect lengths, which ranged from 200 to 450 m, were chosen to avoid intersecting obstructions behind the barrier while still completely sampling the dune profile. These coastal features (morphological parameters) were utilized to identify temporal trends and spatial patterns with a focus on post-storm response and recovery.

The shoreline position was defined as the MHW elevation for the lidar's date (Hapke et al.,

2011). The dune crest was identified as the cross-shore profile's maximum elevation. The dune toe, referred to as *dune low* in storm impact studies (Sallenger, 2000), was defined as the point of maximum slope change seaward of the dune crest. This definition follows Stockdon et al. (2007), except that identification is limited to elevations within the interval $[x_{sl},\ x_{dc}]$. The identification was accomplished by fitting a 5^{th}-order spline to the cross-shore profile between x_{sl} and x_{dc} and taking the spline's second derivative. Next, the position of maximum slope change (i.e. the spline's second derivative in space) within the cross-shore profile yields x_{dt} and z_{dt}. This was found to be a sufficient and robust method for the study area, as compared to more complex techniques (Wernette et al., 2016), because the morphology consisted of a single foredune with minimal relief. In Figure 2.3 sections of the 1998 and 2013 DTMs are shown with example feature extraction results and cross-shore transect. If a dune was not present, then dune low was not defined. The reader is also referred to Figure 3 in Stockdon et al. (2007) for a diagram portraying the cross-shore profile and extracted features.

Dune volume was defined as sediment volume above a common threshold. The mean dune tow elevation ($\overline{z_{dt}}$) across the entire lidar survey collection was chosen to minimize the effects of seasonality and storm impacts on the individual surveys. To obtain a constant threshold through time, it was necessary to define the threshold relative to MSL on a per survey basis. In nature z_{dt} is related to MSL, therefore defining a mean threshold relative to NAVD88 would bias the volumetric calculations with respect to time due to MSL rise. In other words, a common threshold referenced to NAVD88 would sit higher in the dune profiles of more recent surveys relative to the older surveys and result in the estimation of less sediment volume in newer surveys relative to older surveys. Therefore, z_{dt} elevations were transformed from NAVD88 to MSL for each survey before taking the mean, where MSL at the survey's acquisition date was estimated from the GI NOAA station. Mean z_{dt} referenced to MSL was transformed back to NAVD88 for each survey to define dune sediment.

DTM elevation above $\overline{z_{dt}}$ was integrated to estimate dune volume (see Eq. 2.1 for expression). Dune volume per unit width was calculated by dividing V_d by the alongshore length. Change in morphological parameters and dune volume were calculated by taking the difference between lidar surveys, expressed as $\Delta\chi = \chi_{t_2} - \chi_{t_1}$, where χ represents a morphological parameter. Rates of change were computed with two methods: (1) the slope of a least-squares linear regression of the parameter's complete time series; (2) the net change (i.e. t_2 =2013 and t_1 =1998) divided by the total time elapsed.

A.5 Assessment of lidar accuracy

Quality control of lidar data is critical for morphological analyses of low-elevation dune systems. This is evidenced by the pre- and post-Hurricane Gustav lidar. These surveys each have reported vertical accuracies of ±15 cm. An observed 55 cm decrease in z_{dc} (the 10% exceedence value for the central zone's post-Gustav change) therefore has an accuracy of ±30 cm. This change represents a 42% ± 23% reduction in the central zone's average z_{dc} (1.33 m). A reduction of 10% of the dune crests by 50% or more would likely warrant further investigation or prompt emergency repairs. However, as shown by the independent ground-truthing, uncorrected systematic biases may interfere with sound management decision-making. The post-Hurricane Gustav lidar displayed a +47 cm bias (see Table A.1). If left uncorrected, and assuming that this bias is representative of the entire survey, the systematic error would reduce the 10% exceedence value of post-storm z_{dc} change to -8 cm or a 6% ± 23% reduction of the average pre-storm x_{dc}. Coastal management may not be justified expending resources to repair this level of dune crest lowering. Thorough circumspection is therefore required when applying three dimensional morphological analyses to lidar data within a low-elevation dune system.

One can possibly question the accuracy of the lidar processing on two bases. (1) The limited spatial extent of the ground-truthing relative to the study area; and (2) the temporal interpolation of the GCP elevations for ground-truthing the older lidar (see Section A.2).

Issue (1) questions whether elevation corrections determined considering the GCPs' limited footprint is applicable to the entire survey. Forty-two of the 48,664 points from the 2010 RTK-GPS survey qualified as GCPs for the entire lidar time-series. The remaining RTK-GPS points occurred on the beach, dunes, and wetlands which are not geodetically stable. The topography at these positions changes considerably in time and, therefore, cannot validate older lidar surveys. However, selecting all 2010 RTK-GPS survey points above MHW yields 2,885 points that can ground-truth the full spatial extent of the 2010 lidar survey. These points occupied cross-shore transects along the entire CH coastline. This additional ground-truthing was performed identically to the others (see Section A.2).

The full 2010 lidar survey showed a bias of -3.2 cm and a RMSE of 12.0 cm when referenced to the 2,885 RTK-GPS points. The ground-truthing of the entire 2010 lidar survey yields errors similar to the spatially-limited ground-truthing reported in Table A.1, i.e. bias = -4.5 cm and RMSE = 4.7 cm. The increased RMSE is plausibly due to vegetation and structures captured by the lidar, but avoided in the RTK-GPS survey. These obstacles introduce larger discrepancies

Table A.7: Optimized MCC parameter values.

Survey	Resolution (m)	Tension	Spline step
1998	0.5	0.200	20
2001	0.5	0.175	15
2002	1.0	0.150	20
2008b	0.5	0.255	15

between the lidar and RTK-GPS, but would not affect mean error determined by ground-truthing the unobstructed Chevron Rd. It is therefore reasonable to apply corrections derived from the limited ground-truthing to the entire study area.

Issue (2) addresses whether the GCPs are valid as reference elevations for the older lidar surveys given regional subsidence. The GCP elevations for the 1998, 2001, and 2002 ground-truthing were vertically shifted by -7.9, -6.3, and -5.6 cm, respectively, based on the observed vertical land movement rate. The RMSE of these lidar surveys, using the shifted GCP elevations as reference values, is smaller than the surveys' reported vertical accuracies (see Table 2.2 and Table A.1). This lends credibility to the methodology despite the difference in observation dates. The 2006, 2008a, 2008b, and 2012 lidar surveys exhibit RMSEs outside their reported vertical accuracies, but do not have an observable trend suggesting an uncorrected bias due to subsidence. Further, the ground-truthing of these surveys yielded relatively narrow absolute error distributions (see standard deviation in Table A.1). This suggests that the relatively larger RMSE values of the 2006, 2008a, 2008b, and 2012 lidar are due to the initial lidar acquisition process, rather than a discrepancy with the interpolated GCP elevations. After correcting the lidar data by their offset from the GCPs (median error), the accuracy of the corrected data, computed as $1.96 \cdot RMSE$, is brought within the reported accuracy for all the surveys except 2008a.

Table A.8: Statistics and cross-validation results for lidar surveys.

Survey	Resolution (m)	Points per cell	Range (m)	Tension	RMSE (m)
1998	0.5	1.047	0.006	500	0.088
	1.0	1.192	0.023	1000	0.094
	2.0	1.784	0.083	1200	0.095
	5.0	6.382	0.289	2000	0.096

	10.0	21.292	0.481	—	—
2001	0.5	1.000	0	500	0.064
	1.0	1.000	0	1000	0.066
	2.0	1.393	0.026	1200	0.067
	5.0	4.672	0.152	2000	0.067
	10.0	16.573	0.313	—	—
2002	0.5	1.007	0.001	500	0.097
	1.0	1.026	0.004	1000	0.096
	2.0	1.103	0.014	1200	0.095
	5.0	1.728	0.090	2000	0.093
	10.0	3.975	0.254	—	—
2006	0.5	1.114	0.002	500	0.052
	1.0	1.198	0.006	1000	0.054
	2.0	1.512	0.033	1200	0.055
	5.0	6.641	0.284	2000	0.054
	10.0	25.333	0.553	—	—
2008a	0.5	4.195	0.001	500	0.108
	1.0	4.275	0.004	1000	0.113
	2.0	4.987	0.030	1200	0.113
	5.0	15.56	0.272	2000	0.111
	10.0	59.861	0.576	—	—
2008b	0.5	1.012	0.002	500	0.075
	1.0	1.052	0.011	1000	0.077
	2.0	1.386	0.064	1200	0.078
	5.0	5.670	0.368	2000	0.079
	10.0	21.547	0.649	—	—
2010	0.5	1.031	0.001	500	0.018
	1.0	1.382	0.011	1000	0.017
	2.0	3.831	0.075	1200	0.017
	5.0	21.600	0.246	2000	0.017

	10.0	82.687	0.418	—	—
2012	0.5	1.067	0.002	500	0.022
	1.0	1.614	0.026	1000	0.022
	2.0	5.363	0.125	1200	0.022
	5.0	30.962	0.295	2000	0.023
	10.0	115.448	0.444	—	—
2013	0.5	1.001	0.000	500	0.023
	1.0	1.030	0.001	1000	0.021
	2.0	1.353	0.013	1200	0.021
	5.0	5.850	0.130	2000	0.021
	10.0	21.505	0.283	—	—

A.6 LWR window-size sensitivity

The side length of the window operator used to compute the LWR can affect the results. Studies in the literature provide little guidance for objectively selecting the window size, besides the notion that it should be sufficient to capture the length scales of interest and yet large enough to reduce noise. However, LWR computed with different window sizes are expected to exhibit a similar alongshore signal. Figure A.4 shows mean LWRs calculated with a range of window sizes. A similar spatial pattern exists for all the window sizes and, as expected, the smaller windows produce higher frequency oscillations. It appears that the 251 m window is shifted slightly to the west, but it exhibits the same pattern. The similarity between LWRs lends credibility to the relationships found with the CH's backbarrier LWR.

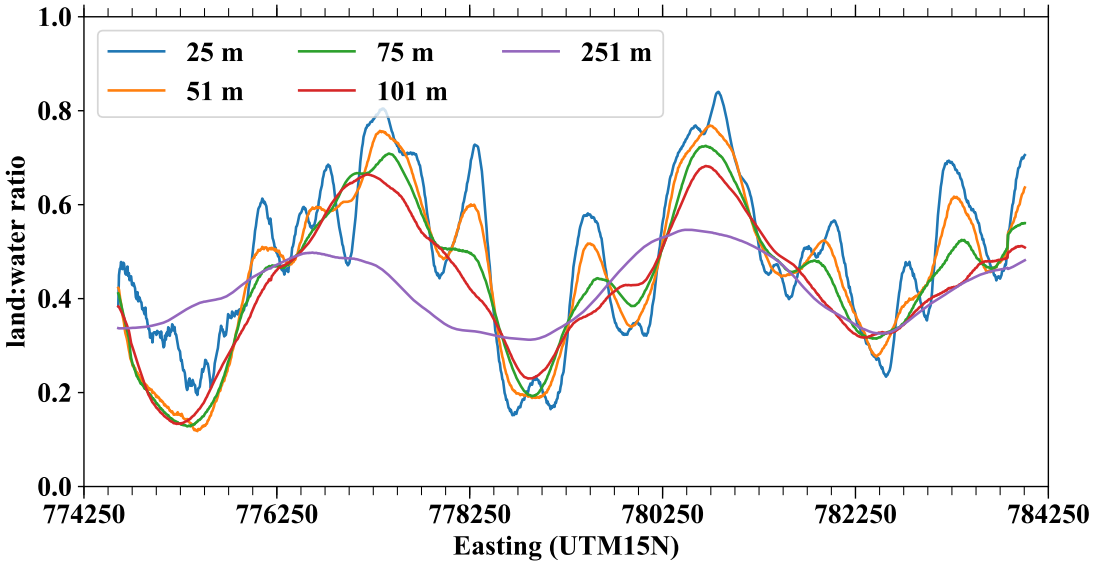

Figure A.4: LWRs computed with different sliding window operator sizes.

APPENDIX B

PERMISSION LETTER FOR CHAPTER 2

Fwd: RE: Enquiry: Permission to publish article in Ph.D. disseration

To: cjoh296@lsu.edu
From: Simon Allen <simon.allen@unige.ch>
Date: Wed, 24 Jun 2020 08:52:32 +0200 (*06/24/2020 01:52:32 AM*)

Dear Cody

It is fine to publish your own papers as part of your thesis. See message below from the jounral manager. Note the last point taken from the elsevier policies.

Best,
Simon Allen

-------- Forwarded Message --------
Subject: RE: Enquiry: Permission to publish article in Ph.D. disseration
Date: Wed, 24 Jun 2020 02:44:06 +0000
From: Wang, Emilie (ELS-BEI) <emilie.wang@elsevier.com>
To: Simon Allen <simon.allen@unige.ch>

Dear Simon,

Thank you for the message. Yes, it is OK for the author to include his own published articles in the thesis, as long as the reference is properly listed. I have also found something from the sharing site at Elsevier (https://www.elsevier.com/about/policies/sharing) as shown below. Please check the last point in the screenshot for your information.

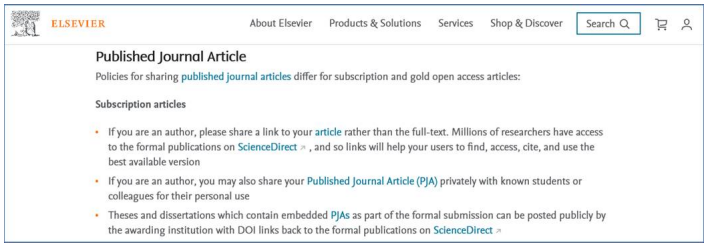

Let me know if you have other questions. Many thanks!

Regards,
Emilie

-- Sender --
First Name: Cody
Last Name: Johnson
Email: cjoh296@lsu.edu

-- Message --
Hello,

I'm requesting permission to include an article previously published in Geomorphology within my Ph.D. dissertation. The article is:

Johnson, C. L., Chen, Q., & Ozdemir, C. E. (2019). Lidar time-series analysis of a rapidly transgressing low-lying mainland barrier (Caminada Headlands, Louisiana, USA). Geomorphology.

Please let me know what actions I need to do to receive permission.

thanks
Cody Johnson

REFERENCES

(2019). Caminada Headland beach and Dune Restoration – Increment I (BA-0045).

Andrews, B. D., P. A. Gares, and J. D. Colby (2002). Techniques for GSIS modeling of coastal dunes. *Geomorphology 48*(1-3), 289–308.

Ardaman & Associates, I. (2018). Design report caminada headlands back barrier marsh creation increment II. Technical report, Coastal Protection and Restoration Authority, Baton Rouge, LA.

Blum, M. D. and H. H. Roberts (2009). Drowning of the Mississippi Delta due to insufficient sediment supply and global sea-level rise. *Nature Geoscience2 2*(7), 488–491.

Blumentrath, S. (2015). Addon v.lidar.mcc. Geographic resources analysis support system (GRASS) software, version 7.4.

Boyd, R. and S. Penland (1981). WASHOVER OF DELTAIC BARRIERS ON THE LOUISIANA COAST. *Transactions - Gulf Coast Association of Geological Societies 31*, 243–248.

Brenner, O. T., L. J. Moore, and A. B. Murray (2015). The complex influences of back-barrier deposition, substrate slope and underlying stratigraphy in barrier island response to sea-level rise: Insights from the Virginia Barrier Islands, Mid-Atlantic Bight, U.S.A. *Geomorphology 246*, 334–350.

Byrnes, M. R., J. L. Berlinghoff, S. F. Griffee, S. Underwood, and D. M. Lee (2017). Louisiana Barrier Island Comprehensive Monitoring Program (BICM): Phase 2 - Shoreline Compilation and Change Assessment. Technical report, Coastal Protection and Restoration Authority, Baton Rouge, LA.

Byrnes, M. R., C. Hedderman, M. Hasen, H. H. Roberts, S. M. Khalil, and S. G. UNDERWOOD (2015). Differential Sediment Consolidation Associated With Barrier Beach Restoration: Caminada Headland, South Louisiana. *Proceedings of Coastal Sediments '15*.

Charnock, H. (1955, oct). Wind stress on a water surface. *Quarterly Journal of the Royal Meteorological Society 81*(350), 639–640.

Coastal Engineering Consultants, I. (2015). Caminada Headlands Beach and Dune Restoration (BA-45) Completion Report. Technical report, Coastal Protection and Restoration Authority, Baton Rouge, LA.

Congedo, L. (2016). Semi-Automatic Classification Plugin Documentation.

Cooper, J., A. Green, and C. Loureiro (2018, sep). Geological constraints on mesoscale coastal barrier behaviour. *Global and Planetary Change 168*, 15–34.

Cooper, J. A. G. (2013, oct). Mesoscale geomorphic change on low energy barrier islands in Chesapeake Bay, U.S.A. *Geomorphology 199*, 82–94.

Couvillion, B. R., J. A. Barras, G. D. Steyer, W. Sleavin, M. Fischer, H. Beck, N. Trahan, B. Griffin, and D. Heckman (2011). Land area change in coastal Louisiana 1932 to 2010.

Couvillion, B. R., H. Beck, D. Schoolmaster, and M. Fischer (2017). Land area change in coastal Louisiana (1932 to 2016). Technical report, United States Geogical Survey, Reston, VA.

de Vet, P. L. M. (2014). *Modeling Sediment Transport and Morphology during Overwash and Breaching Events*. Ph. D. thesis, Delft University of Technology.

de Vet, P. L. M., R. T. McCall, J. P. Den Bieman, M. J. Stive, and M. V. Ormondt (2015). Modelling Dune Erosion , Overwash and Breaching At Fire Island (Ny) During Hurricane Sandy. In *Coastal Sediments '15*, pp. 1–10.

Dean, R. G. (2002). *Beach Nourishment: Theory and Practice*. Advanced series on ocean engineering. World Scientific.

Dietrich, J. C., J. J. Westerink, A. B. Kennedy, J. M. Smith, R. E. Jensen, M. Zijlema, L. H. Holthuijsen, C. Dawson, R. A. Luettich, M. D. Powell, V. J. Cardone, A. T. Cox, G. W. Stone, H. Pourtaheri, M. E. Hope, S. Tanaka, L. G. Westerink, H. J. Westerink, and Z. Cobell (2011). Hurricane Gustav (2008) Waves and Storm Surge: Hindcast, Synoptic Analysis, and Validation in Southern Louisiana. *Monthly Weather Review 139*(8), 2488–2522.

Dingler, J. R. and T. E. Reiss (1995). Beach Erosion on Trinity Island, Louisiana Caused by Hurricane Andrew. *Journal of Coastal Research 1992*(21), 254–264.

Donnelly, C. (2007). Morphologic Change by Overwash : Establishing and Evaluating Predictors. *Journal of Coastal Research* (50), 520–526.

Doran, K. S., H. F. Stockdon, B. K. L. Sopkin, N. G. Plant, A. H. Sallenger, K. K. Guy, and S. A. Kathrine (2009). Hurricane Gustav : Observations and Analysis of Coastal Change. *Director*, 54.

Doughty, S. D., W. J. Cleary, and B. A. McGinnis (2004). The Recent Evolution of Storm-Influenced Retrograding Barriers in Southeastern North Brazil The Recent Evolution of Storm-Influenced Retrograding Barriers in Southeastern. *8th International Coastal Symposium 1*(39), 122–126.

Durán, R., J. Guillén, A. Ruiz, J. A. Jiménez, and E. Sagristà (2016, dec). Morphological changes, beach inundation and overwash caused by an extreme storm on a low-lying embayed beach bounded by a dune system (NW Mediterranean). *Geomorphology 274*, 129–142.

Eisemann, E. R., D. J. Wallace, M. C. Buijsman, and T. Pierce (2018). Response of a vulnerable barrier island to multi-year storm impacts: LiDAR-data-inferred morphodynamic changes on Ship Island, Mississippi, USA. *Geomorphology*.

Energy Information Administration (2020). Louisiana - State Energy Profile Analysis - U.S. Energy Information Administration (EIA).

Eustis, C. L. (2010). Geotechnical Data Collection Report Caminada headland beach and Dune Restoraion Project (BA-45) LaFourche and Jeffereson Parishes, Louisiana. Technical report, GeoEngineers, Inc., Baton Rouge, Louisiana.

Evans, J. S. and A. T. Hudak (2007). A multiscale curvature algorithm for classifying discrete return LiDAR in forested environments. *IEEE Transactions on Geoscience and Remote Sensing 45*(4), 1029–1038.

Everard, M., L. Jones, and B. Watts (2010). Have we neglected the societal importance of sand dunes? An ecosystem services perspective. *Aquatic Conservation: Marine and Freshwater Ecosystems 20*(4), 476–487.

Fearnley, S. M., M. D. Miner, M. Kulp, C. Bohling, and S. Penland (2009). Hurricane impact and recovery shoreline change analysis of the Chandeleur Islands, Louisiana, USA: 1855 to 2005. *Geo-Marine Letters 29*(6), 455–466.

FitzGerald, D. M., I. Buynevich, and B. Argow (2006). Model of Tidal Inlet and Barrier Island Dynamics in a Regime of Accelerated Sea Level Rise. *Journal of Coastal Research II*(39), 789–795.

FitzGerald, D. M., M. S. Fenster, B. a. Argow, and I. V. Buynevich (2008). Coastal Impacts Due to Sea-Level Rise. *Annual Review of Earth and Planetary Sciences 36*(1), 601–647.

Fredericks, X., C. Kranenburg, D. Nagle, and K. Doran (2017). EAARL Coastal Topography—Eastern Louisiana Barrier Islands, 09 March 2008: U.S. Geological Survey data release. Technical report, United States Geological Survey, St. Petersburg.

French, J., A. Payo, B. Murray, J. Orford, M. Eliot, and P. Cowell (2016). Appropriate complexity for the prediction of coastal and estuarine geomorphic behaviour at decadal to centennial scales. *Geomorphology 256*, 3–16.

Gagliano, B. S. M., H. J. Kwon, J. L. V. Beek, and B. Rouge (1970). Deterioration and Restoration of Coastal Wetlands. *Coastal Engineering Proceedings1 12*, 1767–1782.

Gallagher, E. L., S. Elgar, and R. T. Guza (1998, feb). Observations of sand bar evolution on a natural beach. *Journal of Geophysical Research: Oceans 103*(C2), 3203–3215.

Georgiou, I. Y., D. M. FitzGerald, and G. W. Stone (2005). The Impact of Physical Processes along the Louisiana Coast. *Journal of Coastal Research Sp. Issue*(Figure 1), 72–89.

GRASS Development Team (2018). Geographic Resources Analysis Support System (GRASS GIS) Software.

Guisado-Pintado, E. and D. W. Jackson (2018, jul). Multi-scale variability of storm Ophelia 2017: The importance of synchronised environmental variables in coastal impact. *Science of The Total Environment 630*, 287–301.

Gutierrez, B. T., S. J. Williams, and E. R. Thieler (2007). Potential for shoreline changes due to sea-level rise along the U.S. mid-Atlantic region. Technical report, USGS.

Hanley, M. E., S. P. Hoggart, D. J. Simmonds, A. Bichot, M. A. Colangelo, F. Bozzeda, H. Heurtefeux, B. Ondiviela, R. Ostrowski, M. Recio, R. Trude, E. Zawadzka-Kahlau, and R. C. Thompson (2014). Shifting sands? Coastal protection by sand banks, beaches and dunes. *Coastal Engineering 87*, 136–146.

Hapke, C. J., E. A. Himmelstoss, M. G. Kratzmann, J. H. List, and E. R. Thieler (2011). National assessment of shoreline change: Historical shoreline change along the New England and Mid-Atlantic coasts. Technical report, U.S. Geological Survey.

Hapke, C. J., M. G. Kratzmann, and E. A. Himmelstoss (2013). Geomorphic and human influence on large-scale coastal change. *Geomorphology 199*, 160–170.

Harper, J. (1977). Sediment Dispersal Trends of the Caminada-Moreau Beach-Ridge System. *Transactions - Gulf Coast Association of Geological Societies 27*, 283–289.

Harter, C. and J. Figlus (2017). Numerical modeling of the morphodynamic response of a low-lying barrier island beach and foredune system inundated during Hurricane Ike using XBeach and CSHORE. *Coastal Engineering 120*(April 2016), 64–74.

Harter, C., J. Figlus, and T. Dellapenna (2015, jul). THE ROLE OF HURRICANES ON THE MORPHOLOGICAL EVOLUTION OF A SEDIMENT-STARVED BARRIER ISLAND ALONG THE UPPER TEXAS COAST: FOLLETS ISLAND. *Proceedings of Coastal Sediments '15*.

Hinkel, J., R. J. Nicholls, R. S. Tol, Z. B. Wang, J. M. Hamilton, G. Boot, A. T. Vafeidis, L. McFadden, A. Ganopolski, and R. J. Klein (2013). A global analysis of erosion of sandy beaches and sea-level rise: An application of DIVA. *Global and Planetary Change 111*, 150–158.

Holland, G. J., J. I. Belanger, and A. Fritz (2010). A Revised Model for Radial Profiles of Hurricane Winds. *Monthly Weather Review 138*(12), 4393–4401.

Hoonhout, B. (2015). XBeach Documentation.

Houser, C. (2012, nov). Feedback between ridge and swale bathymetry and barrier island storm response and transgression. *Geomorphology 173-174*, 1–16.

Houser, C. (2013). Alongshore variation in the morphology of coastal dunes: Implications for storm response. *Geomorphology 199*, 48–61.

Houser, C. and S. Hamilton (2009, apr). Sensitivity of post-hurricane beach and dune recovery to event frequency. *Earth Surface Processes and Landforms 34*(5), 613–628.

Houser, C., C. Hapke, and S. Hamilton (2008). Controls on coastal dune morphology, shoreline erosion and barrier island response to extreme storms. *Geomorphology 100*, 223–240.

Houser, C. and S. Mathew (2011). Alongshore variation in foredune height in response to transport potential and sediment supply: South Padre Island, Texas. *Geomorphology 125*(1), 62–72.

Houser, C., P. Wernette, E. Rentschlar, H. Jones, B. Hammond, and S. Trimble (2015). Post-storm beach and dune recovery: Implications for barrier island resilience. *Geomorphology 234*, 54–63.

Hu, K., Q. Chen, and H. Wang (2015). A numerical study of vegetation impact on reducing storm surge by wetlands in a semi-enclosed estuary. *Coastal Engineering 95*, 66–76.

IPCC (2014). *Climate Change 2014: Synthesis Report. Contribution of Working Groups I, II and III to the Fifth Assessment Report of the Intergovernmental Panel on Climate Change*. IPCC2014b: IPCC.

Jafari, N. H., B. D. Harris, and T. D. Stark (2018). Geotechnical investigations at the caminada headlands beach and dune in coastal Louisiana. *Coastal Engineering 142*(March), 82–94.

Jafari, N. H., B. D. Harris, and T. D. Stark (2019, dec). Settlement of the Caminada Headlands Beach and Dune Nourishment in Coastal Louisiana. *Journal of Geotechnical and Geoenvironmental Engineering 145*(12), 05019013.

Johnson, C. L., Q. Chen, and C. E. Ozdemir (2019, dec). Lidar time-series analysis of a rapidly transgressing low-lying mainland barrier (Caminada Headlands, Louisiana, USA). *Geomorphology*.

Johnson, C. L., Q. J. Chen, C. E. Ozdemir, K. Xu, R. T. McCall, and K. Nederhoff (2020). Morphodynamic Modeling of a Low-lying Barrier Subject to Hurricane Forcing: The Role of Backbarrier Wetlands. *Coastal Engineering (under review.*

Keim, B. D., R. A. Muller, and G. W. Stone (2007). Spatiotemporal patterns and return periods of tropical storm and hurricane strikes from Texas to Maine. *Journal of Climate 20*(14), 3498–3509.

Kennedy, A. B., U. Gravois, B. Zachry, R. Luettich, T. Whipple, R. Weaver, J. Reynolds-Fleming, Q. J. Chen, and R. Avissar (2010). Rapidly installed temporary gauging for hurricane waves and surge, and application to Hurricane Gustav. *Continental Shelf Research 30*(16), 1743–1752.

Kindinger, J. L., N. a. Buster, J. G. Flocks, J. C. Bernier, and M. a. Kulp (2013). Louisiana Barrier Island Comprehensive Monitoring (BICM) Program Summary Report: Data and Analyses 2006 through 2010. Technical report, U.S. Geological Survey.

Kindinger, J. L., J. Flocks, M. A. Kulp, S. Penland, and L. D. Britsch (2001). Sand Resources, Regional Geology, and Coastal Processes for the Restoration of the Barataria Barrier Shoreline. Technical report, US Geological Survey, New Orleans, LA.

Krabill, W. B., C. W. Wright, R. N. Swift, E. B. Frederick, S. S. Mankade, J. K. Yungel, C. F. Martin, J. G. Sonntag, M. Duffy, W. Hulslander, and J. C. Brock (2000). Airborne Laser Mapping of Assateague National Seachore Beach. *Photogrammetric Engineering & Remote Sensing 66*(1), 65–71.

Krone, R. B. (1985). *Simulation of marsh growth under rising sea level*. Univ. Calif. at Davis, Dep. Civ. Eng., Davis, CA, United States; Tenn. Val. Auth. , , USA , United States: Am. Soc. Civ. Eng. : New York, NY, United States.

Kuhn, N. L., I. A. Mendelssohn, and D. J. Reed (1999, sep). Altered hydrology effects on Louisiana salt marsh function. *Wetlands 19*(3), 617–626.

Kulk, M., D. M. Fitzgerald, and S. Penland (2005). Sand-Rich Lithosomes of the Holocene Mississippi River Delta Plain. *SEPM Society for Sedimentary Geology* (83), 277–293.

Kulp, M., S. Penland, S. J. Williams, C. Jenkins, J. Flocks, and J. Kindinger (2005). Geologic Framework , Evolution , and Sediment Resources for Restoration of the Louisiana Coastal Zone. *Journal of Coastal Research* (44), 56–71.

Kulp, M. A., A. A. Howell, S. Penland, J. L. Kindinger, and S. J. Williams (2002). Latest Quaternary stratigraphic framework of the Mississippi river delta region. *Gulf Coast Association of Geological Societies Transactions2 52*, 573 – 582.

Kurum, M. O., M. Overton, and H. Mitasova (2012). Land Cover and Sediment Layers as Controls of Inlet Breaching. *Coastal Engineering Proceedings 1*(33), 1–9.

Leatherman, S. P. (1987). Annotated Chronological Bibliography of Barrier Island Migration. *Journal of Coastal Research 3*(1), 1–14.

Lentz, E. E. and C. J. Hapke (2011). Geologic framework influences on the geomorphology of an anthropogenically modified barrier island: Assessment of dune/beach changes at Fire Island, New York. *Geomorphology 126*(1-2), 82–96.

Lesser, G. R., J. A. Roelvink, J. A. van Kester, and G. S. Stelling (2004, oct). Development and validation of a three-dimensional morphological model. *Coastal Engineering 51*(8-9), 883–915.

Levinson, D. H., K. R. Knapp, M. C. Kruk, J. H. Howard, and J. P. Kossin (2010). The International Best Track Archive for Climate Stewardship (IBTrACS) project: Overview of methods and Indian ocean statistics. *Indian Ocean Tropical Cyclones and Climate Change*, 215–221.

Lindemer, C. A., N. G. Plant, J. A. Puleo, D. M. Thompson, and T. V. Wamsley (2010). Numerical simulation of a low-lying barrier island's morphological response to Hurricane Katrina. *Coastal Engineering 57*(11-12), 985–995.

Liu, K., Q. Chen, K. Hu, K. Xu, and R. R. Twilley (2018). Modeling hurricane-induced wetland-bay and bay-shelf sediment fluxes. *Coastal Engineering 135*(December 2017), 77–90.

Lopez, J. A. (2009). The Multiple Lines of Defense Strategy to Sustain Coastal Louisiana. *Journal of Coastal Research 10054*(54), 186–197.

Lorenzo-Trueba, J. and G. Mariotti (2017, aug). Chasing boundaries and cascade effects in a coupled barrier-marsh-lagoon system. *Geomorphology 290*, 153–163.

Louisiana Coastal Protection and Restoration Authority (2017). Louisiana's Comprehensive Master Plan for a Sustainable Coast. Technical report, Coastal Protection and Restoration Authority, Baton Rouge, LA.

Luijendijk, A., G. Hagenaars, R. Ranasinghe, F. Baart, G. Donchyts, and S. Aarninkhof (2018). The State of the World's Beaches. *Scientific Reports*, 1–11.

Masselink, G. and S. Van Heteren (2014). Response of wave-dominated and mixed-energy barriers to storms. *Marine Geology 352*, 321–347.

Matias, A., Ó. Ferreira, A. Vila-Concejo, T. Garcia, and J. A. Dias (2008). Classification of washover dynamics in barrier islands. *Geomorphology 97*(3-4), 655–674.

Matias, A., A. Vila-Concejo, Ó. Ferreira, B. Morris, and J. A. Dias (2009). Sediment Dynamics of Barriers with Frequent Overwash. *Journal of Coastal Research 253*, 768–780.

Mattocks, C. and C. Forbes (2008, jan). A real-time, event-triggered storm surge forecasting system for the state of North Carolina. *Ocean Modelling 25*(3-4), 95–119.

McCall, R. T., J. S. M. Van Thiel de Vries, N. G. Plant, A. R. Van Dongeren, J. A. Roelvink, D. M. Thompson, and A. J. H. M. Reniers (2010). Two-dimensional time dependent hurricane overwash and erosion modeling at Santa Rosa Island. *Coastal Engineering 57*(7), 668–683.

McFeeters, S. K. (1996). The use of the Normalized Difference Water Index (NDWI) in the delineation of open water features. *International Journal of Remote Sensing 17*(7), 1425–1432.

Mederios, S. C., S. C. Hagen, and J. F. Weishampel (2012). Comparison of floodplain surface roughness parameters derived from land cover data and field measurements. *Journal of Hydrology 452–453*, 1582–1590.

Mederios, S. C., S. C. Hagen, and J. F. Weishampel (2015). A Random Forest Model Based on Lidar and Field Measurements for Parameterizing Surface Roughness in Coastal Modeling. *IEEE Journal of Selected Topics in Applied Earth Observations and Remote Sensing 4*(8), 1582–1590.

Miot da Silva, G. and P. Hesp (2010, aug). Coastline orientation, aeolian sediment transport and foredune and dunefield dynamics of Moçambique Beach, Southern Brazil. *Geomorphology 120*(3-4), 258–278.

Miselis, J. L., B. D. Andrews, R. S. Nicholson, Z. Defne, N. K. Ganju, and A. Navoy (2016). Evolution of Mid-Atlantic Coastal and Back-Barrier Estuary Environments in Response to a Hurricane: Implications for Barrier-Estuary Connectivity. *Estuaries and Coasts 39*(4), 916–934.

Miselis, J. L. and J. Lorenzo-Trueba (2017). Natural and Human-Induced Variability in Barrier-Island Response to Sea Level Rise. *Geophysical Research Letters 44*(23), 11,922–11,931.

Miselis, J. L. and J. E. McNinch (2006). Calculating shoreline erosion potential using nearshore stratigraphy and sediment volume: Outer Banks, North Carolina. *Journal of Geophysical Research: Earth Surface 111*(2), 1–15.

Mitasova, H., L. Mitas, and R. S. Harmon (2005). Simultaneous Spline Interpolation and Topographic Analysis for LIDAR Elevation Data: Methods for Open Source GIS. *IEEE Geoscience and Remote Sensing Letters 2*(4), 375–379.

Mitasova, H., M. F. Overton, J. J. Recalde, D. J. Bernstein, and C. W. Freeman (2009). Raster-Based Analysis of Coastal Terrain Dynamics from Multitemporal Lidar Data. *Journal of Coastal Research 252*, 507–514.

Moore, L. J., J. H. List, S. J. Williams, and D. Stolper (2010, jul). Complexities in barrier island response to sea level rise: Insights from numerical model experiments, North Carolina Outer Banks. *Journal of Geophysical Research 115*.

Moore, L. J., K. Patsch, J. H. List, and S. J. Williams (2014). The potential for sea-level-rise-induced barrier island loss: Insights from the Chandeleur Islands, Louisiana, USA. *Marine Geology 355*, 244–259.

Morang, A., J. Rosati, and D. King (2013). Regional Sediment Processes, Sediment Supply, and their Impact on the Louisiana Coast. *Journal of Coastal Research Sp.Issue*(63), 141–165.

Morris, J. T., P. V. Sundareshwar, C. T. Nietch, B. Kjerfve, and D. R. Cahoon (2002, oct). Responses of Coastal Wetlands to Rising Sea Level. *Ecology 83*(10), 2869.

Morton, R. A. (2002). Factors Controlling Storm Impacts on Coastal Barriers and Beaches - A Preliminary Basis for Near Real-Time Forecasting. *Journal of Coastal Research 18*(3), 486–501.

Morton, R. A. (2010, jul). First-Order Controls of Extreme-Storm Impacts on the Mississippi–Alabama Barrier-Island Chain. *Journal of Coastal Research 264*(264), 635–648.

Morton, R. A., J. C. Gibeaut, and J. G. Paine (1995, aug). Meso-scale transfer of sand during and after storms: implications for prediction of shoreline movement. *Marine Geology 126*(1-4), 161–179.

Morton, R. A., J. G. Paine, and J. C. Gibeaut (1994). Stages and Durations of Post-Storm Beach Recovery, Southeastern Texas Coast, U.S.A. *Journal of Coastal Research 10*(4), 884–908.

Morton, R. A. and A. H. Sallenger Jr. (2003). Morphological Impacts of Extreme Storms on Sandy Beaches and Barriers. *Journal of Coastal Research 19*(3), 560–573.

Nederhoff, C., Q. Lodder, M. Boers, J. den Bieman, and J. Miller (2015, jul). MODELING THE EFFECTS OF HARD STRUCTURES ON DUNE EROSION AND OVERWASH. In *Coastal Sediments*. World Scientific Pub Co Pte Lt.

Neteler, M. and H. Mitasova (2008). *Open Source GIS: A GRASS GIS Approach* (3rd ed.). New York, NY: Springer.

Nienhuis, J. H., A. D. Ashton, D. A. Edmonds, A. J. F. Hoitink, A. J. Kettner, J. C. Rowland, and T. E. Tornqvist (2020, jan). Global-scale human impact on delta morphology has led to net land area gain. *Nature 577*(7791), 514–518.

Odezulu, C. I., J. Lorenzo-Trueba, D. J. Wallace, and J. B. Anderson (2018). Follets Island: A Case of Unprecedented Change and Transition from Rollover to Subaqueous Shoals. In *Barrier Dynamics and Response to Changing Climate*, pp. 147–174. Cham: Springer International Publishing.

Oppenheimer, M., B. Glavovic, J. Hinkel, R. van de Wal, A. K. Magnan, A. Abd-Elgawad, R. Cai, M. Cifuentes-Jara, R. M. DeConto, T. Ghosh, J. Hay, F. Isla, B. Marzeion, B. Meyssignac, and Z. Sebesvari (2019). Sea Level Rise and Implications for Low Lying Islands, Coasts and Communities. *IPCC Special Report on the Ocean and Cryosphere in a Changing Climate 355*(6321), 126–129.

Orson, R., W. Panageotou, and S. P. Leatherman (1985). Response of Tidal Salt Marshes of the U.S. Atlantic and Gulf Coasts to Rising Sea Levels. *Journal of Coastal Research 1*(1), 29–37.

Otvos, E. G. (2011, jul). Hurricane signatures and landforms—toward improved interpretations and global storm climate chronology. *Sedimentary Geology 239*(1-2), 10–22.

Otvos, E. G. (2012, feb). Coastal barriers — Nomenclature, processes, and classification issues. *Geomorphology 139-140*, 39–52.

Otvos, E. G. (2020, apr). Coastal barriers - fresh look at origins, nomenclature and classification issues.

Passeri, D. L., M. V. Bilskie, N. G. Plant, J. W. Long, and S. C. Hagen (2018). Dynamic modeling of barrier island response to hurricane storm surge under future sea level rise. *Climatic Change*.

Passeri, D. L., J. W. Long, N. G. Plant, M. V. Bilskie, and S. C. Hagen (2018). The influence of bed friction variability due to land cover on storm-driven barrier island morphodynamics. *Coastal Engineering 132*(August 2017), 82–94.

Penland, S. and R. Boyd (1981). Shoreline Changes on the Louisiana Barrier Coast. *Oceans*, 209 – 219.

Penland, S., R. Boyd, and J. R. Suter (1988). Trangressive Depositional Systems of the Mississppi Delta Plain: A model for Barrier shoreline and Shelf Sand Development. *Journal of Sedimentary Petrology 58*(6), 932–949.

Penland, S., K. Debusschere, K. A. Westphal, J. R. Suter, and R. A. Mcbride (1989). THE 1985 HURRICANE IMPACTS ON THE ISLES DERNIERES , LOUISIANA : A TEMPORAL AND SPATIAL ANALYSIS OF THE COASTAL GEOMORPHIC CHANGES. *Transactions - Gulf Coast Association of Geological Societies 39*.

Powell, M. D., P. J. Vickery, and T. A. Reinhold (2003, mar). Reduced drag coefficient for high wind speeds in tropical cyclones. *Nature 422*(6929), 279–283.

Priestas, A. M. and S. Fagherazzi (2010). Morphological barrier island changes and recovery of dunes after Hurricane Dennis, St. George Island, Florida. *Geomorphology 114*(4), 614–626.

Psuty, N. P., K. Ames, A. Habeck, and W. Schmelz (2018). Responding to coastal change: Creation of a regional approach to monitoring and management, northeastern region, U.S.A. *Ocean and Coastal Management 156*, 170–182.

QGIS Development Team (2018). QGIS Geographic Information System.

Rader, A. M., A. J. Pickart, I. J. Walker, P. A. Hesp, and B. O. Bauer (2018). Foredune morphodynamics and sediment budgets at seasonal to decadal scales: Humboldt Bay National Wildlife Refuge, California, USA. *Geomorphology 318*, 69–87.

Restore the Mississippi River Delta (2020). What's at Risk: Economy — Restore the Mississippi River Delta.

Ritchie, W. and S. Penland (1988). Rapid dune changes associated with overwash processes on the deltaic coast of South Louisiana. *Marine Geology 81*(1-4), 97–122.

Roberts, H. H. (1997). Dynamic Changes of the Holocene Mississippi River Delta Plain: The Delta Cycle. *Journal of Coastal Research 13*(3), 605–627.

Roelvink, D., R. McCall, S. Mehvar, K. Nederhoff, and A. Dastgheib (2017). Improving predictions of swash dynamics in XBeach: The role of groupiness and incident-band runup. *Coastal Engineering* (February), 1–21.

Roelvink, D., A. Reniers, A. van Dongeren, J. van Thiel de Vries, R. McCall, and J. Lescinski (2009). Modelling storm impacts on beaches, dunes and barrier islands. *Coastal Engineering 56*(11-12), 1133–1152.

Roelvink, D., G. Stelling, B. Hoonhout, J. Risandi, W. Jacobs, and D. Merli (2012). Development and Field Validation of a 2Dh Curvilinear Storm Impact Model. *Coastal Engineering*, 1–14.

Rosati, J. D. and G. W. Stone (2007). Critical Width of Barrier Islands and Implications for Engineering Design. *Coastal Sediments '07 40926*(May 2007), 1988–2001.

Rosati, J. D. and G. W. Stone (2009). Geomorphologic Evolution of Barrier Islands along the Northern U.S. Gulf of Mexico and Implications for Engineering Design in Barrier Restoration. *Journal of Coastal Research 251*, 8–22.

Sallenger, A. H. (2000). Storm Impact Scale for Barrier Islands. *Journal of Coastal Research 16*(3), 890–895.

Sallenger, A. H., W. B. Krabill, R. N. Swift, J. C. Brock, J. H. List, M. Hansen, R. A. Holman, S. Manizade, J. Sontag, A. Meredith, K. Morgan, J. K. Yunkel, E. B. Frederick, and H. F. Stockdon (2003). Evaluation of airborne topographic lidar for quantifying beach changes. *Journal of Coastal Research 19*(1), 125–133.

Sallenger, A. H., H. F. Stockdon, L. Fauver, M. Hansen, D. Thompson, C. W. Wright, and J. Lillycrop (2006). Hurricanes 2004 : An Overview of Their Characteristics and Coastal Change. *Estuaries and Coasts 29*(6A), 880–888.

Sasser, C. E., J. M. Visser, E. Mouton, J. Linscombe, and S. B. Hartley (2008). Vegetation Types in Coastal Louisiana in 2007. Technical report, U.S> Geological Survey.

Schambach, L., A. R. Grilli, S. T. Grilli, M. R. Hashemi, and J. W. King (2018). Assessing the impact of extreme storms on barrier beaches along the Atlantic coastline: Application to the southern Rhode Island coast. *Coastal Engineering 133*(September 2017), 26–42.

Sherman, D. J., B. U. Hales, M. K. Potts, J. T. Ellis, H. Liu, and C. Houser (2013). Impacts of Hurricane Ike on the beaches of the Bolivar Peninsula, TX, USA. *Geomorphology 199*, 62–81.

Sherwood, C. R., J. W. Long, P. J. Dickhudt, P. S. Dalyander, D. M. Thompson, and N. G. Plant (2014). Inundation of a barrier island (Chandeleur Islands, Louisiana, USA) during a hurricane: Observed water-level gradients and modeled seaward sand transport. *Journal of Geophysical Research: Earth Surface 119*(7), 1498–1515.

Shirley, J. S. (2020). Louisiana Coastal Wetlands: A Resource At Risk - USGS Fact Sheet.

Siverd, C. G., S. C. Hagen, M. V. Bilskie, D. H. Braud, S. Gao, R. H. Peele, and R. R. Twilley (2019). Assessment of the temporal evolution of storm surge across coastal Louisiana. *Coastal Engineering 150*, 59–78.

Siverd, C. G., S. C. Hagen, M. V. Bilskie, D. H. Braud, R. H. Peele, M. R. Foster-Martinez, and R. R. Twilley (2019b). Coastal Louisiana landscape and storm surge evolution: 1850–2110. *Climatic Change 157*(3), 445–468.

Siverd, C. G., S. C. Hagen, M. V. Bilskie, D. W. H. Braud, R. H. Peele, and R. R. Twilley (2018). Hydrodynamic Storm Surge Model Simplification via Application of Land to Water Isopleths in Coastal Louisiana. *Coastal Engineering 137*, 28–42.

Smallegan, S. M., J. L. Irish, and A. R. van Dongeren (2017). Developed barrier island adaptation strategies to hurricane forcing under rising sea levels. *Climatic Change*, 1–12.

Smallegan, S. M., J. L. Irish, A. R. Van Dongeren, and J. P. Den Bieman (2016). Morphological response of a sandy barrier island with a buried seawall during Hurricane Sandy. *Coastal Engineering 110*, 102–110.

Stive, M. J. (2004). How Important is Global Warming for Coastal Erosion? *Climatic Change 64*(1985), 27–39.

Stockdon, H. F., K. S. Doran, and A. H. Sallenger (2009). Extraction of Lidar-Based Dune-Crest Elevations for Use in Examining the Vulnerability of Beaches to Inundation During Hurricanes pp . 59-65 Published by : Coastal Education & Research Foundation , Inc . Stable URL : http://www.jstor.org/stable/25737452 E. *Journal of Coastal Research 25*(53), 59–65.

Stockdon, H. F., R. A. Holman, P. A. Howd, and A. H. Sallenger (2006). Empirical parameterization of setup, swash, and runup. *Coastal Engineering 53*(7), 573–588.

Stockdon, H. F., A. H. Sallenger, R. A. Holman, and P. A. Howd (2007). A simple model for the spatially-variable coastal response to hurricanes. *Marine Geology 238*(14), 1–20.

Stone, G. W., J. M. G. Iii, J. R. Dingler, D. A. Pepper, G. W. Stone, J. M. G. Iii, J. R. Dingier, and D. A. Pepper (1997). Overview and Significance of Hurricanes on the Louisiana Coast, U.S.A. *Journal of Coastal Research 13*(3), 656–669.

Stone, G. W., B. Liu, D. A. Pepper, and P. Wang (2004). The importance of extratropical and tropical cyclones on the short-term evolution of barrier islands along the northern Gulf of Mexico, USA. *Marine Geology 210*(1-4), 63–78.

Stone, G. W. and J. D. Orford (2004). Storms and their significance in coastal morpho-sedimentary dynamics. *Marine Geology 210*(1-4), 1–5.

Thatcher, C. A., J. C. Brock, J. J. Danielson, S. K. Poppenga, D. B. Gesch, M. E. Palaseanu-Lovejoy, J. A. Barras, G. A. Evans, and A. E. Gibbs (2016). Creating a Coastal National Elevation Database (CoNED) for Science and Conservation Applications. *Journal of Coastal Research SI Coconut Creek Journal of Coastal Research, Special Issue Coconut Creek 76*(76), 64–74.

The American Society for Photogrammetry & Remote Sensing (2013). LAS Specification Version 1.4-R13. Technical Report November 2011, The American Society for Photogrammetry & Remote Sensing.

The LSU Department of Geography and Anthropology (1999). Color Infrared Orthopho, LA, 1998.

Thieler, E. R. and R. S. Young (1991). Quantitative evaluation of coastal geomorphological changes in South Carolina after Hurricane Hugo; Impact of Hurricane Hugo; September 10-20, 1989. *Journal of Coastal Research Special is*(8), 187–200.

Tinkham, W. T., H. Huang, A. M. Smith, R. Shrestha, M. J. Falkowski, A. T. Hudak, T. E. Link, N. F. Glenn, and D. G. Marks (2011). A Comparison of two open source LiDAR surface classification algorithms. *Remote Sensing 3*(3), 638–649.

Toimil, A., I. J. Losada, P. Camus, and P. Díaz-Simal (2017). Managing coastal erosion under climate change at the regional scale. *Coastal Engineering 128*(August), 106–122.

Twilley, R. R., S. J. Bentley, Q. Chen, D. A. Edmonds, S. C. Hagen, N. S. N. Lam, C. S. Willson, K. Xu, D. W. Braud, R. Hampton Peele, and A. McCall (2016). Co-evolution of wetland landscapes, flooding, and human settlement in the Mississippi River Delta Plain. *Sustainability Science 11*(4), 711–731.

U.S. Army Corps of Engineers (2018). Mississippi River Ship Channel, Gulf to Baton Rouge, LA: Integrated General Reevaluation Report and Supplemental Environmental Impact Statement. Technical Report April, Mississippi Valley Division.

van der Lugt, M. A., E. Quataert, A. van Dongeren, M. van Ormondt, and C. R. Sherwood (2019). Morphodynamic modeling of the response of two barrier islands to Atlantic hurricane forcing. *Estuarine, Coastal and Shelf Science 229*(May), 106404.

van Dongeren, A. and I. Svendsen (1997). Absorbing-Generating Boundary Condition for Shallow Water Models. *Journal of Waterway, Port, Coastal, and Ocean Engineering 123*(6), 303–313.

van Rijn, L. C., D.-J. R. Walstra, and M. van Ormondt (2007). Unified View of Sediment Transport by Currents and Waves. II Suspended Transport. *Journal of Hydraulic Engineering 133*(7), 776–793.

Van Thiel de Vries, J. S. (2009). *Beach and dune erosion during storm surges.* Phd dissertation, Delft University of Technology.

Vatvani, D., N. C. Zweers, M. Van Ormondt, A. J. Smale, H. De Vries, and V. K. Makin (2012). Storm surge and wave simulations in the Gulf of Mexico using a consistent drag relation for atmospheric and storm surge models. *Natural Hazards and Earth System Science 12*(7), 2399–2410.

Walters, D., L. J. Moore, O. D. Vinent, S. Fagherazzi, and G. Mariotti (2014). Interactions between barrier islands and backbarrier marshes affect island system response to sea level rise: Insights for a coupled model. *Journal of Geophysical Research: Earth Surface 119*, 2315–2334.

Wang, P. and M. H. Horwitz (2007). Erosional and depositional characteristics of regional overwash deposits caused by multiple hurricanes. *Sedimentology 54*(3), 545–546.

Wernette, P., C. Houser, and M. P. Bishop (2016). An automated approach for extracting Barrier Island morphology from digital elevation models. *Geomorphology 262*, 1–7.

Weston, N. B. (2014). Declining Sediments and Rising Seas: An Unfortunate Convergence for Tidal Wetlands. *Estuaries and Coasts 37*(1), 1–23.

Williams, H. F. L. (2015). Contrasting styles of Hurricane Irene washover sedimentation on three east coast barrier islands: Cape Lookout, North Carolina; Assateague Island, Virginia; and Fire Island, New York. *Geomorphology 231*, 182–192.

Williams, S. J., S. Penland, and J. Sallenger Asbury H. (1992). Atlas of shoreline changes from 1853 to 1989 : Louisiana barrier island erosion study. Imap, U.S. Geological Survey.

Woodroffe, C. D. (2002). *Coasts : form, process, and evolution.* Cambridge ; New York : Cambridge University Press, 2002.

Woodroffe, C. D. (2007). *The Natural Resilience of Coastal Systems: Primary Concepts.* Elsevier.

Woolard, J. W. and J. D. Colby (2002). Spatial characterization, resolution, and volumetric change of coastal dunes using airborne LIDAR: Cape Hatteras, North Carolina. *Geomorphology 48*(1-3), 269–287.

Xu, K., S. J. Bentley, J. W. Day, and A. M. Freeman (2019, sep). A review of sediment diversion in the Mississippi River Deltaic Plain. *Estuarine, Coastal and Shelf Science 225*, 106241.

VITA

Cody Johnson grew up in Florida and developed an appreciation for the coastal environment. He attended Florida State University and received a B.S. in geology and earned an M.S. in Coastal and Ecological Engineering from Louisiana State University in 2016. In his spare time, he tries to keep up with technological advancements and enjoys the game of soccer.

His career continues to focus on the conservation and engineering of the coastal landscape as a research engineer with the Coastal and Hydraulics Laboratory (CHL) of the U.S. Army Corps of Engineer's (USACE) Engineer Research and Development Center (ERDC).